Semi-empirical and ab initio calculations of the optical properties of semiconductor superlattices

Silvana Botti

UNIVERSITÀ DEGLI STUDI DI PAVIA
FACOLTÀ DI SCIENZE MATEMATICHE FISICHE E NATURALI

Dipartimento di Fisica "A. Volta"

SEMI-EMPIRICAL AND AB-INITIO CALCULATIONS OF OPTICAL PROPERTIES IN SEMICONDUCTOR SUPERLATTICES

Silvana Botti

Tesi presentata per il conseguimento del
titolo di Dottore di Ricerca in Fisica
XIV CICLO

Coordinatore del dottorato di ricerca in fisica
presso l'Università di Pavia:
Prof. S. P. Ratti

Tutore nelle attività di ricerca:
Prof. L.C. Andreani

Io vedo le teorie scientifiche come costruzioni umane
– reti progettate da noi per catturare il mondo.
(K. Popper)

A mio padre

Table of contents

Chapter 1

Introduction and overview

A semiconductor heterostructure is an artificial material, basically obtained by epitaxial growth and/or chemical etching of two or more different semiconductors. The size reduction achieved in one, two or three dimensions in heterostructures at the nanoscale level leads to electronic ground and excited states widely different from those of the bulk crystals, and has opened the way to a new generation of optoelectronic and photonic devices.

If we consider the evolution of an electronic state from a bulk crystal to a nanostructure, essentially three phenomena occur. First, the band-offsets at the interfaces act as effective potential barriers, which confine the carriers, both the electrons and the holes, in one, two or three dimensions. Second, for an artificial periodic system, e.g. a superlattice, the supercell is made up by joining a number N_c of primitive cells of the underlying bulk lattices. Hence, in the reciprocal space N_c $\mathbf{k}$-points in the Brillouin zone of the bulk are folded onto the same $\mathbf{k}$-point in the smaller Brillouin zone of the nanostructure, and the artificially superimposed potential induces a coupling between previously independent bulk states. Third, the artificial combination of different materials usually leads to a reduction of the originally higher symmetry of the constituent bulk materials.

Quantum confinement and confinement-induced mixing affect the energy and the dimensionality of electronic levels, the lowering in the crystal symmetry is responsible for the removal of level degeneracies. In practice, to take advantage of all these modifications in the electronic states, we have to consider how they are reflected in

modifications of the quantities of interest. In particular, the optical properties are of the utmost importance, as they lie at the basis of many new technological applications. Among the already well-established applications we can cite the multiple quantum well (MQW) lasers [1, 2], the quantum cascade lasers [3], the Schottky barriers [1, 2], the modulation-doped heterostructures [1, 2], like the high electron mobility transistors (HEMT). Dielectric superlattices are developed for their nonlinear properties, which induce effects such as the optical bistability or the nonlinear frequency conversion [4]. Those effects are also found in semiconductor heterostructures based on GaAs, which has by itself important nonlinear optical properties [5]. The optical bistability has for instance been observed in a photoexcited GaAs/AlAs superlattice [6]. In search of new optical sources, in GaAs/oxidized-AlAs superlattices the optical anisotropy has been exploited to achieve phase matching for second-harmonic generation, the enhanced dielectric contrast has produced a breakthrough in the construction of Bragg reflectors for MQW lasers and microcavities and birefringent waveguides have been proposed [7].

Let us analyze more in details the physical effects involved in the above mentioned applications. Interband absorption spectra of bulk tetrahedral semiconductors (like Silicon, GaAs, AlAs, ...) are dominated by two prominent features, denoted E_1 and E_2 [8, 9]. The E_1 peak originates from band-to-band transitions along the $\Gamma - L$ direction, where valence and conduction bands are nearly parallel: this results in a M_1-type critical point, i.e. a saddle point in the joint density of states, which also gives a strong excitonic character to the transition. The E_2 peak, instead, has contributions from different parts of the Brillouin zone, but mainly from a region centered around the special point $(\frac{3}{4}, \frac{1}{4}, \frac{1}{4})$ (in units of $2\pi/a$, where a is the lattice constant). Starting from a basic level of analysis, in a nanostructure the confinement of the carriers, as the simplistic exercise of the particle in a box can teach, leads to a blue shift and a sharpening of the absorption peaks. In addition, removal of level degeneracies can induce the subdivision of the transitions in groups, leading to splittings of the absorption peaks. In the past, most experimental investigations have focused on the energy region of the fundamental gap, which is easily accessible by photoluminescence and photoluminescence excitation spectroscopies and yields a variety of interesting physical phenomena related to bound excitonic

states. Relatively few studies of confinement effects on high-energy transitions have been presented. Blue shifts and splittings of the E_1 and E_2 transitions were measured in GaAs/AlAs superlattices [10, 11]. More recently, a quantum confinement induced shift of E_1 and E_2 was measured in Ge nanoparticles embedded in a glassy matrix [12, 13]. Concerning theory, confined electronic levels close to band edges, excitonic effects and the resulting optical properties can be calculated rather simply and accurately by the envelope-function method [14]. The theoretical problem of determining optical spectra of semiconductor heterostructures in the whole visible region is much more complex and beyond the reach of effective-mass methods, as it requires a description of the effects of confinement and coupling on electronic states in the whole Brillouin zone.

Yet, there is still a remarkable effect of the reduction of symmetry to be considered, which obliges us to move to a deeper level of analysis of the problem. The original point group of most of the bulk semiconductors which constitute the studied heterostructures is the cubic group of the diamond or zinc-blend structure, which yields an isotropic optical response of the medium. The lowering in the crystal symmetry gives rise to an optical anisotropy in the real part of the dielectric constant (birefringence) and in the imaginary part (absorption anisotropy or dichroism). Even at zero-frequency, birefringence can be large, like in nanostructured silicon surfaces [15], or of moderate amplitude, as in GaAs/AlAs superlattices [16], where it also shows a non-trivial dependence on the superlattice period. The basic picture in terms of transitions between one-electron states, mainly used up to now, ignores contributions from many-body effects which may play a crucial role, and which tend to be especially important when the scale of the system is reduced and the inhomogeneity of the medium is more pronounced. Self-energy and electron-hole interaction (i.e. excitonic) effects can have a significant contribution to the absorption spectra of even simple bulk semiconductors. The former corrects the ground state exchange-correlation potential, the latter describes the variations of the exchange-correlation potential upon excitation. Of course, there are also contributions stemming from variations of the Hartree potential, including the so-called local field effects, which express the fact that these variations reflect the charge inhomogeneity of the responding material. Therefore, local field effects can be of moderate importance,

compared to the exchange-correlation contributions, in the absorption spectra of simple bulk semiconductors, but show up increasingly when one considers more inhomogeneous systems.

Most of the today technologically interesting systems are strongly inhomogeneous, and their potential applications might even be based on their inhomogeneity - superlattices are one of the best examples. As a first conclusion, we can now designate the nearly lattice-matched GaAs/AlAs superlattices as the ideal prototype systems for the understanding of artificial structures. Many reference data are available, since their optical properties have been thoroughly investigated both experimentally [10, 17, 18] and theoretically [19, 20, 21, 22, 23, 24, 25]. In this thesis we will study the electronic states all over the Brillouin zone and the optical properties, with a special care for the optical anisotropy, of two specific kinds of systems: $(\mathrm{GaAs})_p/(\mathrm{AlAs})_p$ superlattices and free-standing GaAs layers, which are simulated by $(\mathrm{GaAs})_p/(\mathrm{vacuum})_p$ superlattices. Both these systems consist in the periodic alternation of layers of two different materials (or also an empty lattice) with an original zinc-blend structure. Each layer is composed by the same number p of (001) planes: $2p$ planes compose the supercell. An example of GaAs/AlAs tetragonal supercell is shown in Fig. 1.1 on page 11. Besides the obvious choice of GaAs/AlAs systems, the motivation for studying GaAs/vacuum superlattices is to analyze how confinement effects act in a system where the electronic states are truly confined in GaAs layers, even at high energies. In GaAs/AlAs superlattices, in fact, the band structures of the two constituents far away from the fundamental band edges are rather similar and strong banding effects occur in short-period structures, i.e. the electronic states become delocalized along the superlattice. A comparison between the two systems should therefore elucidate the respective roles of quantum confinement and superlattice band formation in determining the optical properties. However, free-standing GaAs films are not only an ideal model system, as they can be produced by chemical etching [26], and, moreover, GaAs/vacuum superlattices can be a model for superlattices made of GaAs and a wide-gap oxide, like Al_2O_3 or oxidized AlAs (AlOx).

GaAs/AlAs superlattices have been the subject of various theoretical studies. Most of the approaches well established for bulk band structure calculations reveal

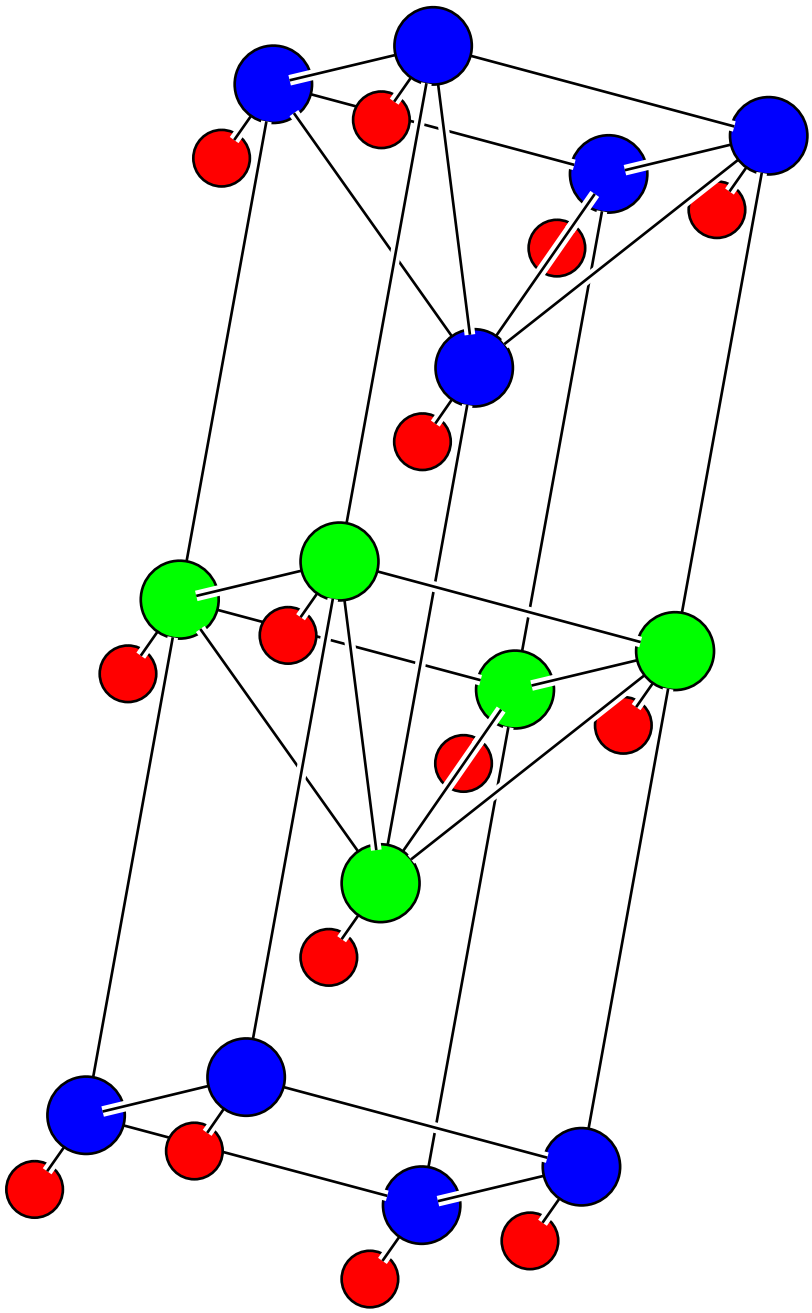

Figure 1.1: Tetragonal supercell for a $(GaAs)_2/(AlAs)_2$ (001) superlattice. Red small circles indicate As atoms, blue circles and green circles indicate respectively Ga and Al atoms.

some weaknesses, when applied to a low-dimensional system. A completely satisfactory method should describe accurately, all over the Brillouin zone, both intervalley coupling and confinement effects, in systems of any scale, constituted by few-atom to million-atom supercells. In literature, only the electronic structure of very-short-period $(GaAs)_p/(AlAs)_p$ superlattices has been calculated from first principles by Density Functional Theory (DFT) and norm-conserving pseudopotentials (see Section 3.5). DFT calculations benefit of a high degree of precision, which cannot be reached by empirical calculations. Nevertheless, the computation time grows rapidly with the number p of monolayers, making the method impractical for large scale systems. Thus, many empirical methods have been developed in the last decades to study large-scale superlattices (see Section 2.1). While reaching a simplification of the problem, they often fail to describe correctly all the physical effects involved. Concerning the optical properties, only a few calculations of absorption spectra for very-small period superlattices exist. Moreover, very few information is known about the dielectric properties and the anisotropy at zero frequency of GaAs/AlAs superlattices. First, the refractive index has been neither measured nor calculated, and it is commonly estimated from the dielectric constants of bulk GaAs and AlAs in the framework of the effective medium approach [27]. This classical theory may fail for small period superlattices, where the delocalization of the electronic states over the superlattice implies that the use of the bulk dielectric constants is not justified anymore. In fact, theoretical calculations have shown for ultrathin (001) $(GaAs)_p/(AlAs)_p$ SL's that an effective medium model cannot explain the behavior from p=1 to p=3 [11]. Second, the change in the refractive index with light polarization – the static birefringence – has been measured for large period (001) $(GaAs)_p/(AlAs)_p$ SL's and a remarkable drop has been observed (see Fig 4.9 on page 90) as the period decreases. This behavior has been suggested to depend on local fields [16]. *Ab initio* methods for ultrathin SL's [11], and a semi-empirical approach for larger ones [28], have been applied neglecting local field effects and did not account for the observed value of the birefringence, nor for its decrease with decreasing p, even qualitatively.

After having defined the systems we are going to study, and after clarifying the reasons for their interest and the variety of physical phenomena that they show, we

want to discuss the objectives of this thesis work. We aim at attaining:

(i) A detailed analysis of the electronic band structure of superlattices; in particular a comprehension of how different physical effects, i.e. confinement, superlattice potential-induced couplings, lowering of crystal symmetry, influence the evolution from the bulk electronic states to the superlattice states.

(ii) An insight in the advantages and disadvantages and an instructive comparison of two powerful models for electronic calculations in solids, namely the pseudopotential Linear Combination of Bulk Bands (LCBB) method [29] and the Density Functional Theory (DFT), used in the Local Density Approximation (LDA), with norm-conserving pseudopotentials and a plane wave basis set. The first of them is based on a semi-empirical parameterization of the pseudopotential, which involves a fitting on experimental data, the second relies completely on first principles. Concerning the LCBB method, we have developed a code based on this method to study superlattice states and optical properties.

(iii) A detailed determination of the dielectric properties of superlattices, both in the isotropic approximation and considering the anisotropy of the dielectric tensor for light polarizations along growth or in-plane directions. We will focus on the behavior under confinement of the peaks in the absorption curves and on the anisotropy of the optical response, in particular calculating the dielectric tensor components and the zero-frequency birefringence. These properties will be analyzed as a function of the superlattice period p. Once again, the discussion will follow the two parallel roads of a semi-empirical and a first-principle Time-Dependent DFT (TDDFT) approach to the problem. The two methods will be applied, on one hand, within the same approximation, to judge the consistency of the corresponding results. On the other hand, we will try to differentiate the calculations in order to cast light on all the possible physical effects presented above. As a first step, we will discuss to what extent confinement and folding-induced modifications on the electronic states are sufficient in reproducing experimental data. This kind of analysis will be carried out in a semi-empirical approach, within the semplified picture of Fermi's golden rule for one-particle states and independent particle transitions. Afterwards, we will

compare the obtained results with totally analogous independent-transition *ab initio* calculations. Then, we will introduce local field effects in the *ab initio* TDDFT calculations, to understand whether they give a relevant contribution to the optical anisotropy, as it can be expected intuitively. We will finally conjecture, in view of the obtained results, how many-body effects can further contribute to the results. We will test two different approximations (RPA and TDLDA) for the inclusion of the exchange-correlation contributions. To include quasi-particle and excitonic effects, within a many-body Green's function formulation is out of reach for the existing computational tools, except in case of very-thin superlattices.

(iv) An innovative investigation of the optical spectra of bulk GaAs and AlAs systems. The application of an improved TDDFT model recently elaborated by Reining *et al.* [30] and up to now only applied to Si bulk crystals, allows to include the many-body effects in the optical spectra in a computational very efficient way. We will establish if it succeeds in reproducing, besides Si spectra, bulk GaAs and AlAs spectra as well. The continuum exciton effect is known to be considerably strong in this kind of systems. An application to superlattices is at the moment premature; nevertheless the quality of the results will be discussed also in view of a future application to heterostructures.

The thesis is organized as follows. In Chapter 2 we introduce the pseudopotential semi-empirical techniques, and in particular the LCBB method: we apply them to calculate bulk (i.e. GaAs and AlAs) and superlattice (i.e. GaAs/AlAs and GaAs/vacuum) band structures. The Density Functional Theory formalism for ground state calculations is described and applied in Chapter 3. The results obtained in the two different approaches are compared at the end of the Chapter 3. In Chapter 4 and 5 we present, respectively, the semi-empirical and *ab initio* calculations of the dielectric properties, with a particular interest in the optical anisotropy. Chapter 6 contains the summary and the discussion of the present findings, also in view of extensions of this work. Finally, in Appendix A we discuss some basic approximations and in Appendix B we present a description of the semi-empirical and norm-conserving *ab initio* pseudopotentials.

Chapter 2

Semi-empirical calculations of superlattice band structures

The first step to face the tasks that we have just presented in the introduction to our work, is the search for a reliable approach to the calculation of the electronic states of quantum nanostructures. Although the problem is more general, we are interested in focusing on the study of (GaAs)/(AlAs) and (GaAs)/(vacuum) superlattices, grown in the [001] direction. In the present and the following chapters, we will analyze two different choices among the big variety of methods developed within the independent-particle scheme. At the end of the next chapter we will be able to compare the band structures obtained by means of the two different methods. Here we start dealing with semi-empirical calculations. We will present a rapid overview of the empirical/semi-empirical methods usually adopted in literature, underlining their advantages and disadvantages. Then, we will motivate the choice of one of this methods, namely the Linear Combination of Bulk Bands (LCBB) method [29, 31]. In particular, we will explain the details of the formalism and how we have applied it to build a computational code. The application of the method requires the availability of good semi-empirical pseudopotentials. The procedure to construct semi-empirical atomic pseudopotentials is discussed in Appendix B. Finally, the calculated superlattice band structures will be compared to the experiment and to the constituent bulk band structures. It is especially interesting to discuss how the bulk states evolve into the superlattice ones.

2.1 The choice of an empirical model

A method is called *empirical* when the electronic Hamiltonian (see Appendix A), which characterizes the physical system, depends on a set of parameters, to be fitted on experimental data. In this sense, we will see that it is more correct to define the method we apply *semi-empirical*, because the fitting procedure considers also numerical data coming from first-principle calculations. If one aims at approaching complex large scale systems, first principle parameter-free techniques often reach their limits: these kind of calculations are not feasible, because of practical computational limitations in time and in memory. In these cases, the choice of one among the many existing empirical or semi-empirical techniques represents a low computational cost solution to investigate, with satisfying reliability, some particular aspects of the problem. It must be clear from the beginning that, to keep reasonably low the number or fitting parameters, it is necessary to give up reaching a too high precision in band structure calculations, especially far from the band gap and the high symmetry points. To compete with the *ab initio* quasi-particle calculations an empirical method should involve a small computational effort and allow to study very large scale systems.

In order to develop and improve the empirical techniques, a considerable effort has been devoted in the last 15 years to go beyond the "standard model", i.e. the $\mathbf{k}\cdot\mathbf{p}$ envelope-function approach [32, 33, 14]. The envelope function method represents the highest degree of simplification of the problem: it substitutes the true microscopic potential and the real band structure with simpler constant potentials and parabolic bands. In a way which reminds the $\mathbf{k}\cdot\mathbf{p}$ model for a bulk crystal, the representation for the Bloch superlattice states $\psi_{i,\mathbf{q}}$ is made of bulk eigenfunctions in $\mathbf{k}_0$, $\left\{u_{n,\mathbf{k}_0}(\mathbf{r})\, e^{i\mathbf{k}_0\cdot\mathbf{r}}\right\}_n$, (usually $\mathbf{k}_0 = \Gamma = \mathbf{0}$):

$$\psi_{i,\mathbf{q}}(\mathbf{r}) = \sum_{n,\mathbf{G}_{SL}} c^{(i,\mathbf{q})}_{n,\mathbf{G}_{SL}} \Big[\, u_{n,\mathbf{\Gamma}}(\mathbf{r})\, e^{i\mathbf{G}_{SL}\cdot\mathbf{r}} \Big]\, e^{i\mathbf{q}\cdot\mathbf{r}}\,, \tag{2.1}$$

where $\mathbf{G}_{SL}$ are superlattice reciprocal lattice vectors and n is the bulk band index. This type of representation suggests an intuitive criterion to select the band indices n to include in the finite sum in Eq. (2.1): only the bulk states not too far in energy from the searched state $\psi_{i,\mathbf{q}}$ are physically important. While eminently successful in describing states in wide quantum wells, this approach encounters strong limitations

in modeling small systems with more complex geometries, like short/medium period superlattices, wires and dots. The band structure far from $\mathbf{k}_0$ cannot be reproduced in a satisfactory way, as it already happened in a $\mathbf{k} \cdot \mathbf{p}$ calculation for a bulk solid, unless an extremely high number of basis function are considered. The mixing effects between states labelled by $\mathbf{k}$-points connected by a nanostructure reciprocal vector, and thus coupled by the mesoscopic periodicity of the superlattice potential, are not accounted for and must be introduced artificially. As a result, the application of this method is advised only if one is interested in the dispersion of a single band edge of the heterostructure, which originates from states of the bulk material coming from a region close to the selected point $\mathbf{k_0}$. On the other hand, excitonic effects and external fields can be easily modeled to be included, as an approximation, in calculations. The more sophisticated and accurate $\mathbf{k} \cdot \mathbf{p}$ generalizations, which can include multiband coupling throughout all the Brillouin zone, have been discussed in many recent works (see for example Ref. [34, 35, 36, 37]). A semi-quantitative description of superlattices has been obtained by Dandrea and Zunger [21] within a virtual-crystal approximation. This model represents a further step in the direction of relating the superlattice levels to those of their constituents.

The search for improvements is intended to avoid the drastic solution of a "direct diagonalization", which gives accurate results, but is, from a computational point of view, as expensive as the *ab initio* approaches. The direct diagonalization approach comes from an antithetic starting point: it consists in expanding the nanostructure wave functions on a large basis, usually made of plane waves or localized atomic states. The empirical tight-binding model [38, 39, 40, 41] expresses the ionic potential $V(\mathbf{r})$ of the nanostructure as a superposition of atomic empirical potentials. The nanostructure wave functions are expanded on a set of localized atomic orbitals. The variational flexibility of the basis is quite limited and the calculations usually do not include more than the second or third nearest-neighbor interactions. The computational time is fairly high for an empirical method: the dimension of the basis scales as the number N of atoms of the cell, in its turn the diagonalization time scales as N^3, making the method impractical already for a system made of a few thousands of atoms. A more flexible basis is offered by a plane wave set, to be used in connection with atomic empirical pseudopotentials (EPM) [42, 20]. Nevertheless,

the choice of a delocalized basis set does not change the limit size of 10^3 atoms. The advantage of these two methods, in comparison to the standard envelope function model, is the ability to study a system characterized by whatever complex geometry, without losing symmetry information.

The *Linear Combination of Bulk Bands* (LCBB) method, proposed some years ago by Wang, Franceschetti and Zunger [29] allows a gathering of the advantages of many different methods. This approach has proved to be able to face the problem of the electronic structure all over the Brillouin zone, for a nanostructure made of up to million atoms supercells, characterized by any geometry. In fact, it needs a small computational expense and includes naturally all the folding and confinement effects. As the name of the method suggests, it consists in expanding the electronic wavefunctions of the nanostructure as a linear combination of the eigenfunctions of the bulk constituent materials. Unlike tight-binding or standard plane wave expansions, a basis of bulk states allows to pre-select intuitively the physically important states which may mix in the formation of the nanostructure state, hence the dimension of the basis can be reduced as much as to make possible to approach large scale systems. By contrast with the $\mathbf{k}\cdot\mathbf{p}$ envelope function method, off-Γ states $u_{n,\mathbf{k}\neq 0}e^{i\mathbf{k}\cdot\mathbf{r}}$ are directly considered, permitting a correct treatment of multiband confinement-induced couplings within the Brillouin zone, without the need for a large basis of $\mathbf{k}=0$ bulk states. Moreover, a technique whose starting points are the bulk states is the most suitable tool to understand how the bulk states evolve into the superlattice ones, allowing to study further which effects contribute to the differences between the optical spectra of the superlattices and their constituent bulk materials. All these motivations have lead us to choose the semi-empirical LCBB method.

2.2 The Linear Combination of Bulk Bands method

The LCBB method, as presented in Refs. [29, 31] can be easily applied to every kind of nanostructure. Although more general, from now on we restrict the presentation of the formalism to $(\mathrm{A})_p/(\mathrm{B})_p$ superlattices, made of alternating layers of two different materials characterized by an original zinc-blend structure, grown in the direction [001]. In practice, two specific kinds of periodic systems have been studied:

$(\mathrm{GaAs})_p/(\mathrm{AlAs})_p$ and $(\mathrm{GaAs})_p/(\mathrm{vacuum})_p$ superlattices, with a superlattice period p ranging from 4 to 20. We choose to constrain the width $d/2 = p/2a$ of the A layers to be equal to the width of B layers. In GaAs/vacuum superlattices a is simply the experimental GaAs lattice constant, whereas in GaAs/AlAs superlattices a is the average of the experimental lattice constants of the the almost lattice-matched GaAs and AlAs crystals. In fact, the lattice mismatch is so small (about 0.15% [43]) that it can be neglected for our purposes, thus allowing to use the strain-free formalism [31].

According to the LCBB approach, the superlattice electronic wave functions are expressed as linear combinations over band indices n and wave vectors $\mathbf{k} = \mathbf{q}+\mathbf{G}_{SL}$ [1] of full-zone Bloch eigenstates of the constituent bulk materials:

$$\psi_{i,\mathbf{q}}(\mathbf{r}) = \sum_{\sigma=A,B} \sum_{n,\mathbf{G}_{SL}}^{N_b,N_{\mathbf{G}_{SL}}} c^{(i,\mathbf{q})}_{n,\mathbf{G}_{SL},\sigma}\, u^{\sigma}_{n,\mathbf{q}+\mathbf{G}_{SL}}(\mathbf{r})\, e^{i(\mathbf{q}+\mathbf{G}_{SL})\cdot\mathbf{r}}\,. \tag{2.2}$$

In the expression (2.2) the first sum runs over the two constituent bulk materials, A=GaAs and B=AlAs,vacuum, the second sum runs over the band indices n and the supercell reciprocal lattice vectors $\mathbf{G}_{SL}$, belonging to the first Brillouin zone of the underlying bulk lattice. Because of the supercell periodicity, the superimposed superlattice potential mixes up only bulk states labelled by $\mathbf{k} = \mathbf{q} + \mathbf{G}_{SL}$ vectors which differ by a superlattice reciprocal lattice vector $\mathbf{G}_{SL}$: the number of coupled states is hence always equal to $2p$, because exactly $2p$ vectors $\mathbf{G}_{SL}$ are contained in the fcc Brillouin zone. The maximum dimension of the basis set is then given by $2p$ multiplied by the number N_b of selected bulk bands indices. The classification of the bulk states by means of the band index n and the dispersion of the bands as a function of $\mathbf{k}$ allow an intuitive selection of the bands to be retained in the basis: the physically relevant states belong to energy bands close in energy to the superlattice states we are interested in calculating. For example, if one is aiming at studying the optical absorption in an energy range close to the gap, the bulk states to be included in the basis are those close to the optical gap. We know that, for each independent point $\mathbf{k} = \mathbf{q} + \mathbf{G_{SL}}$, the bulk eigenfunctions of type σ form an infinite orthonormal set. In the ideal case of an infinite representation for the superlattice

[1] From now on we will indicate with $\mathbf{q}$ a reciprocal space vector inside the tetragonal Brillouin zone of the superlattice, with $\mathbf{k}$ a vector inside the bulk Brillouin zone, with $\mathbf{G}_{SL}$ a superlattice reciprocal lattice vector which is contained inside the first Brillouin zone of the underlying bulk lattice, and with $\mathbf{G}$ a bulk reciprocal lattice vector.

wavefunctions, it would be equivalent to use the bulk set of type A or B, whereas it would be an error to merge them in a unique set, which would obviously yield an overcomplete basis. Nevertheless, using a small set of bulk eigenfunctions, it is more convenient to create a mixed set of A and B eigenstates, provided that the resulting basis is orthonormalized before being used.

Local semi-empirical continuous atomic pseudopotentials have been picked out from literature [44] to build the pseudopotential term in the one-particle Hamiltonian. These pseudopotentials have been used to perform all the semi-empirical band structure calculations, first for the bulk constituent materials and then for the heterostructures. A detailed description of the pseudopotential method is presented in Appendix B. Since the adopted pseudopotentials are designed for a kinetic-energy cutoff of 5 Ry, [44] bulk eigenfunctions are expanded on a plane wave basis set truncated at about 60 plane-waves at each $\mathbf{k}$-point:

$$\phi^{\sigma}_{n,\mathbf{k}}(\mathbf{r}) = \frac{1}{\sqrt{\Omega}} \sum_{\mathbf{G}} B^{\sigma}_{n,\mathbf{k}}(\mathbf{G})\, e^{i(\mathbf{k}+\mathbf{G})\cdot\mathbf{r}}\,, \tag{2.3}$$

where Ω is the bulk fcc cell volume. This means that, as a consequence, also the superlattice states are a linear combination of the same small set of plane waves. However, the method is much more powerful than a simple direct diagonalization on the plane wave basis, because the first diagonalization step concerning the bulk constituents furnishes a set of conveniently weighted plane waves to face the more complex superlattice problem. Instead, a standard plane wave expansion would require a much larger plane wave basis, whose dimension would continue growing proportionally to the number of atoms in the supercell. At this stage we have decided to neglect the spin-orbit interaction, even if it is possible to include it, as explained in Ref. [44]. In Figs. 2.2 and 2.3 we show the band structures of GaAs and AlAs calculated with these pseudopotentials. More details are discussed in the following section.

Moving finally to the superlattice one-particle Hamiltonian, we observe that the pseudopotential term is built as a superposition of screened, spherical atomic local pseudopotentials v_α:

$$H = -\frac{\hbar^2\nabla^2}{2m} + \sum_{\alpha} \sum_{\mathbf{R}\in DL} v_\alpha\left(\mathbf{r}-\mathbf{R}-\mathbf{d}_\alpha\right) W_\alpha\left(\mathbf{R}\right)\,, \tag{2.4}$$

where $\mathbf{R}$ is a fcc direct lattice (DL) vector and $\mathbf{d}_\alpha$ the displacement of the atom of type α in the bulk primitive cell. The index α can assume four different values for a GaAs/AlAs superlattice, because an As atom in the GaAs environment is considered different from an As atom in the AlAs environment. In case of GaAs/vacuum superlattices only three constituents are admitted: Ga, As (in GaAs environment) and empty lattice sites. To preserve a correct description of interfaces in GaAs/AlAs superlattices, an As atom bound to two Al and two Ga atoms has been attributed a symmetrized pseudopotential, which is the average of the As pseudopotential functions in GaAs and AlAs environments.

The weight function $W_\alpha(\mathbf{R})$ selects the atom basis which lies on each lattice site, defining the geometrical details and the symmetry of the structure: in the vacuum layers its value is zero. In the following calculations we assume ideal sharp interfaces, which are described by a step-like weight function $W_\alpha(\mathbf{R})$. However, the interfacial roughness, which is always present in real samples, can be easily simulated by a segregated profile of $W_\alpha(\mathbf{R})$, as discussed in Ref. [29]. The Hamiltonian matrix elements on the bulk basis set are given by

$$\begin{aligned}\langle \sigma', n', \mathbf{G}'_{SL}+\mathbf{q}|\, H\, |\sigma, n, \mathbf{G}_{SL}+\mathbf{q}\rangle = \sum_{\mathbf{G},\mathbf{G}'} \left[B^{\sigma'}_{n',\mathbf{G}'_{SL}+\mathbf{q}}(\mathbf{G}')\right]^* \\ \left[\frac{\hbar^2}{2m}\,|\mathbf{q}+\mathbf{G}_{SL}+\mathbf{G}|^2\,\delta_{\mathbf{G}_{SL},\mathbf{G}'_{SL}}\,\delta_{\mathbf{G},\mathbf{G}'} + \sum_\alpha v_\alpha(|\mathbf{G}_{SL}+\mathbf{G}-\mathbf{G}'_{SL}-\mathbf{G}'|)\right. \\ \left. e^{i\,d_\alpha\cdot(\mathbf{G}_{SL}+\mathbf{G}-\mathbf{G}'_{SL}-\mathbf{G}')}\,W_\alpha(\mathbf{G}_{SL}-\mathbf{G}'_{SL})\right]\left[B^{\sigma}_{n,\mathbf{G}_{SL}+\mathbf{q}}(\mathbf{G})\right].\end{aligned} \tag{2.5}$$

They depend on the Fourier transform of the pseudopotentials (i.e. a continuum form factor) $v_\alpha(\mathbf{r})$:

$$\int_\Omega d\mathbf{r}\, e^{i(\mathbf{G}_{SL}+\mathbf{G})\cdot\mathbf{r}}\, v_\alpha(\mathbf{r}) = \Omega\, v_\alpha(|\mathbf{G}_{SL}+\mathbf{G}|)\,, \tag{2.6}$$

and the Fourier transform of the weight function $W_\alpha(\mathbf{R})$:

$$W_\alpha(\mathbf{G}_{SL}) = \frac{1}{N_p}\sum_{\mathbf{R}\in DL} W_\alpha(\mathbf{R})\, e^{i\mathbf{G}_{SL}\cdot\mathbf{R}}\,, \tag{2.7}$$

where N_p equals the number of bulk lattice points in the crystal volume.

It is evident that the few discrete pseudopotential form factors (i.e. the Fourier transform coefficients of the pseudopotential $v_\alpha(\mathbf{r})$, evaluated at the smallest $\mathbf{G}$ vec-

tor shells of the reciprocal lattice), which are sufficient to calculate the bulk band structure, are no longer enough to obtain the matrix elements for the superlattice Hamiltonian. The Fourier transform (2.6) is needed at all the superlattice reciprocal lattice vectors $\mathbf{G}_{SL}$. When the superlattice period p grows, the superlattice reciprocal lattice becomes denser and denser and, in the limit of an infinitely large supercell, we need to know the Fourier transform of the pseudopotential $v_\alpha(x)$ for all the real values $x = |\mathbf{G} + \mathbf{G}_{SL}|$, as a continuum function. We use the continuous-space functions $v_\alpha(x)$ proposed by Mäder and Zunger [44]. Details on the construction of the semi-empirical pseudopotentials and a table of the parameters can be found in Appendix B. In Ref. [44], the empirical parameters of the pseudopotential function are adjusted in order to fit both the measured electronic properties of bulk GaAs and AlAs and some DFT-Local Density Approximation (LDA) results for superlattices. This last requirement is the reason why we have called these pseudopotential "semi-empirical", instead of simply "empirical". It has been verified that the wave functions of bulk and p=1-superlattice systems calculated with these pseudopotentials are close to those obtained in rigorous first principles LDA calculations [44]. These pseudopotentials are adjusted to reproduce the experimental GaAs/AlAs valence band offset (0.50 eV). As bulk and superlattice energy levels are provided in the same absolute energy scale, their eigenvalues can be compared directly. The Fourier transform of the weight function W_α can be calculated analytically in the case of abrupt interfaces. Its expression reveals a proportionality to the inverse of the superlattice period p [45]:

$$W_\alpha(\mathbf{G}_{SL}) = \frac{1}{4p}\sum_{l=1}^{p} 2\, e^{i(l-1)\frac{\pi j}{p}} \qquad \alpha = \text{Ga, As (in GaAs)}\,, \tag{2.8}$$

$$W_\alpha(\mathbf{G}_{SL}) = \frac{1}{4p}\sum_{l=p+1}^{2p} 2\, e^{i(l-1)\frac{\pi j}{p}} \qquad \alpha = \text{Al,As (in AlAs)}\,, \tag{2.9}$$

$$W_\alpha(\mathbf{G}_{SL}) = 0 \qquad \alpha = \text{empty lattice site}\,; \tag{2.10}$$

where

$$\mathbf{G}_{SL} = \Gamma + \frac{2\pi}{pa}(0,0,j) \qquad j \in (-p, p]\,. \tag{2.11}$$

As a result, the coupling between bulk wavefunctions coming from **k**-points in the fcc Brillouin zone connected by a superlattice vector $\mathbf{G}_{SL}$ becomes less relevant as the superlattice period p grows. Moreover, a different behavior for even or odd p is

detected.

2.3 From bulk to superlattice states

The first step to study the superlattice band structures by the LCBB method is the calculation of the bulk energy levels and eigenfunctions all over the Brillouin zone. The dispersions of the energy levels along the high symmetry directions in the fcc Brillouin zone, for GaAs and AlAs crystals, are shown respectively in Figs. 2.2 and 2.3. The energy zero is fixed at the top of the valence band of GaAs, for both GaAs and AlAs band structures. This choice is meant to emphasize the advantages offered by the semi-empirical pseudopotentials parametrized in Ref. [44]: the electronic energies extracted by the diagonalization of the Hamiltonian (2.5) lie on an absolute energy scale, thus the energy levels of GaAs and AlAs can be directly compared and the difference between the highest occupied levels of the two materials at Γ gives the 0.5 eV valence band offset without further adjustments. The fit of s-like conduction-band edges at the high symmetry points Γ, X, L is excellent, especially in the case of GaAs. Yet, we will notice that the error remains relevant, even 0.7 eV with respect to the experiment for the p-like GaAs Γ_{15c} (see Tables 3.2 and 3.3). The numeric values of the energy levels at the high symmetry points will be further discussed in the comparative tables mentioned above, after the presentation of the analogous *ab initio* band structure calculations in Section 3.5. It is worth remembering that the semi-empirical pseudopotential implemented here is local, whereas the norm-conserving pseudopotential accounts for non-local contributions. Hence it is expected that the quality of first principle band structure is higher.

Starting from a bulk basis set to expand the superlattice wavefunctions obliges to think about the way in which the bulk states couple to evolve to the superlattice states. The cubic symmetry of the bulk lattices is reduced when the superlattice is built and the growth direction z is no longer equivalent to the orthogonal in-plane directions x and y. The ideal structure for a lattice-matched system with abrupt interfaces is a simple tetragonal Bravais lattice, with a supercell defined by the basis vectors $(1,1,0)\,a/2$, $(-1,1,0)\,a/2$, $(0,0,1)\,pa$, where a is the bulk lattice constant. The reciprocal lattice is also simple tetragonal, with basis vectors $(1,1,0)\,(2\pi)/a$,

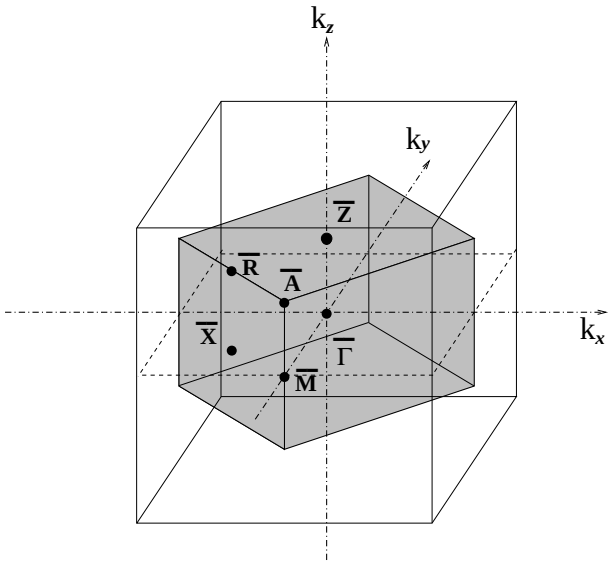

Figure 2.1: Brillouin zone for simple tetragonal $(\mathrm{GaAs})_p/(\mathrm{AlAs})_p$ and $(\mathrm{GaAs})_p/(\mathrm{vacuum})_p$ (001) superlattices, included in bulk conventional cubic cell. The figure shows high symmetry points positions.

$(-1,1,0)\,(2\pi)/a$ and $(0,0,1)\,(2\pi)/(pa)$. The first Brillouin zone is shown in Fig. 2.1. Superlattice high symmetry points are distinguished from their bulk counterparts by putting a bar over the symbol. An additional symmetry point $\bar{L}$ is defined as follows: $\bar{L} = \bar{X}$ if p is even, $\bar{L} = \bar{R}$ if p is odd. The most important zinc-blend **k**-points are folded onto superlattice points as follows:

$$\begin{aligned} \Gamma, \left\{\frac{j}{p}X^z\right\}_{j=-p+1,p} &\longrightarrow \bar{\Gamma}\,, \\ X^y, \left\{\frac{j}{p}X^z\right\}_{j=-p+1,p} &\longrightarrow \bar{M}\,, \\ L_{111}, \left\{\frac{j}{p}X^z\right\}_{j=-p+1,p} &\longrightarrow \bar{L}\,. \end{aligned} \tag{2.12}$$

In the case of a common anion structure like $(\mathrm{GaAs})_p/(\mathrm{AlAs})_p$ the point group is D_{2d}, otherwise it is C_{2v}: the latter is the case of $(\mathrm{GaAs})_p/(\mathrm{vacuum})_p$ superlattices [46]. In Fig. 2.1 we show the tetragonal Brillouin zone and the high-symmetry-points. First of all, we consider the case of GaAs/AlAs superlattices, where two different bulk materials constitute the alternating layers. We can observe that GaAs and AlAs band structures are very similar, thus we do expect to still be able to recognize

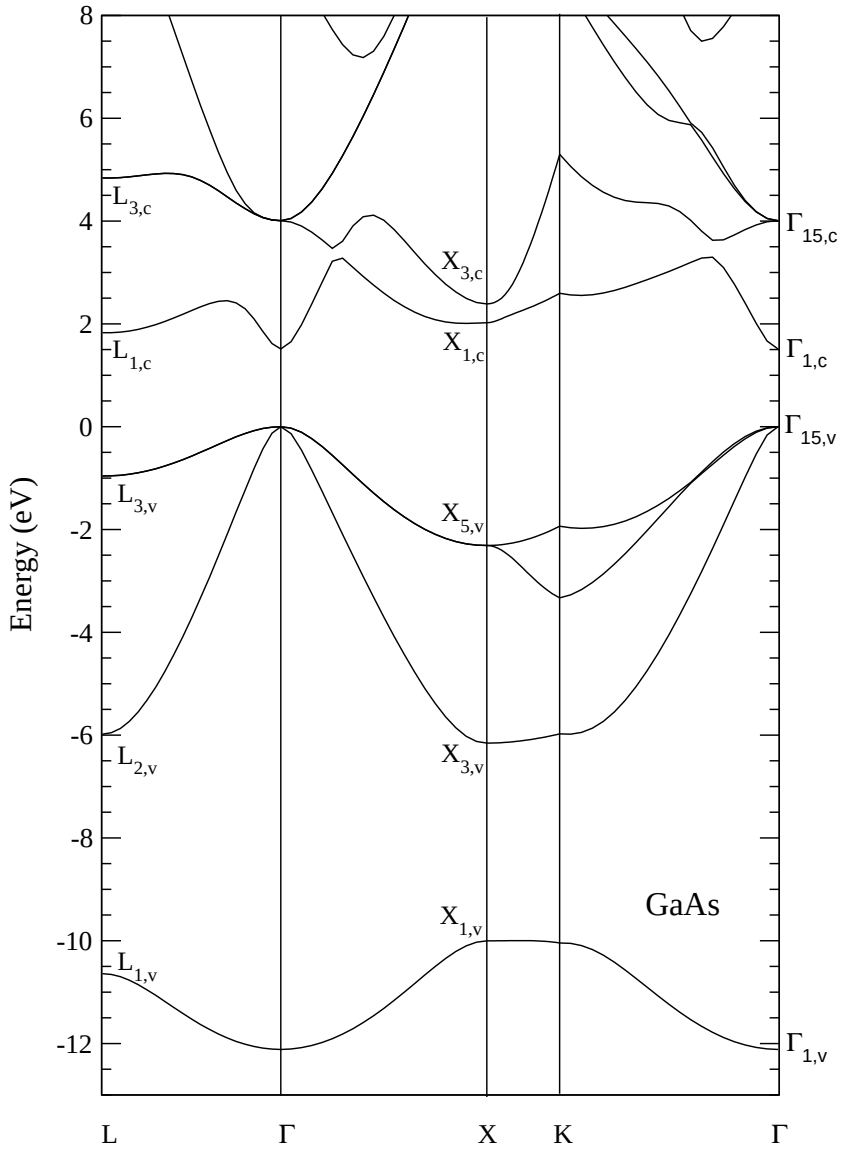

Figure 2.2: Bulk band structure of a GaAs crystal along the high symmetry directions, obtained by the semi-empirical pseudopotentials of Ref. [44]. The energy zero is taken at the valence band maximum of bulk GaAs.

in the superlattice band dispersion the characteristic features present in the bulk dispersions. However, comparing directly the GaAs/AlAs band dispersion, shown e.g. in Fig. 2.6, with the bulk band structures in Figs. 2.2 and 2.3 is misleading and cannot reveal these expected similarities. Before being instructively compared, the two band structure must be referred to the same Brillouin zone. The tetragonal supercell contains $2p$ bulk fcc Wigner-Seitz cells, as a consequence, in the reciprocal space the tetragonal Brillouin zone is contained in the bulk octahedron Brillouin zone (see Fig. 2.1). The bulk states outside the superlattice tetragonal Brillouin zone can be folded into it, by adding tetragonal reciprocal lattice vectors. The result is a $2p$ times denser band dispersion along the tetragonal symmetry directions. The $(\mathrm{GaAs})_{2p}$ band structure showed, for p=10, in Fig. 2.4 is completely equivalent to the more usual picture in Fig. 2.2. We remember that in the bulk fcc crystal the directions [001] and [100] are equivalent, hence the bulk band dispersion is the same along the $\bar{\Gamma}$-$\bar{M}$ and $\bar{\Gamma}$- $\bar{Z}$ lines. Now, if we compare the $(\mathrm{GaAs})_{20}$ band structure in the tetragonal Brillouin zone with the $(\mathrm{GaAs})_{10}/(\mathrm{AlAs})_{10}$ superlattice band structure in Fig. 2.6, we are struck by their similarity. However, they are not equal, because beside the consequences of folding, also coupling effects occur when a superlattice is built. Starting from a simple perturbation picture, when the superlattice potential is switched on, it couples the previously independent bulk bands, relative to the same superlattice point $\mathbf{q}$, but coming from non-equivalent points $\mathbf{q}+\mathbf{G}_{SL}$ in the bigger fcc Brillouin zone. The effect is an overall modification of the energy levels. In particular, since the superlattice potential has a lower symmetry, it can remove level degeneracies. It is time to observe that there are some slight, but relevant, differences in the bulk band structures of GaAs and AlAs: they differ with regard to the first conduction band. The conduction minimum of GaAs is in Γ, the minimum of AlAs is in X instead. Thanks to the absolute energy scale, we can compare directly the distance in energy of the two edges, which measures only 0.2 eV. Moreover, we know that the bulk $\mathbf{k}$-points Γ and X can be connected by a superlattice reciprocal lattice vector $\mathbf{G}_{SL}$. Starting again from the perturbation theory picture, we can easily see that the bulk GaAs eigenfunctions in Γ can be strongly coupled to the AlAs eigenfunctions in X. This effect is known in literature as Γ-X *coupling* and has remarkable consequences on the properties of the minimum

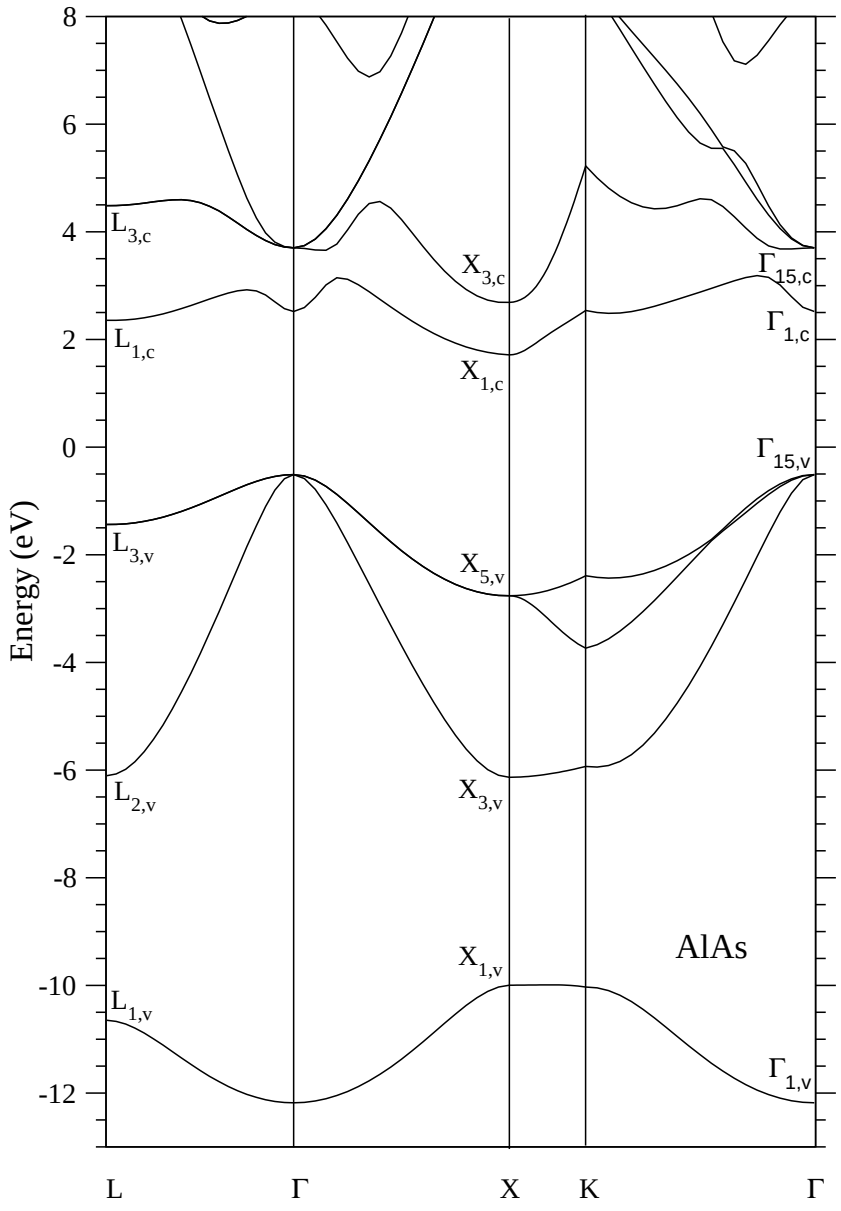

Figure 2.3: Bulk band structure of AlAs along the high symmetry directions, obtained by the semi-empirical pseudopotentials of Ref. [44]. The energy zero is always taken at the valence band maximum of bulk GaAs, hence the valence band offset between GaAs and AlAs is 0.5 eV.

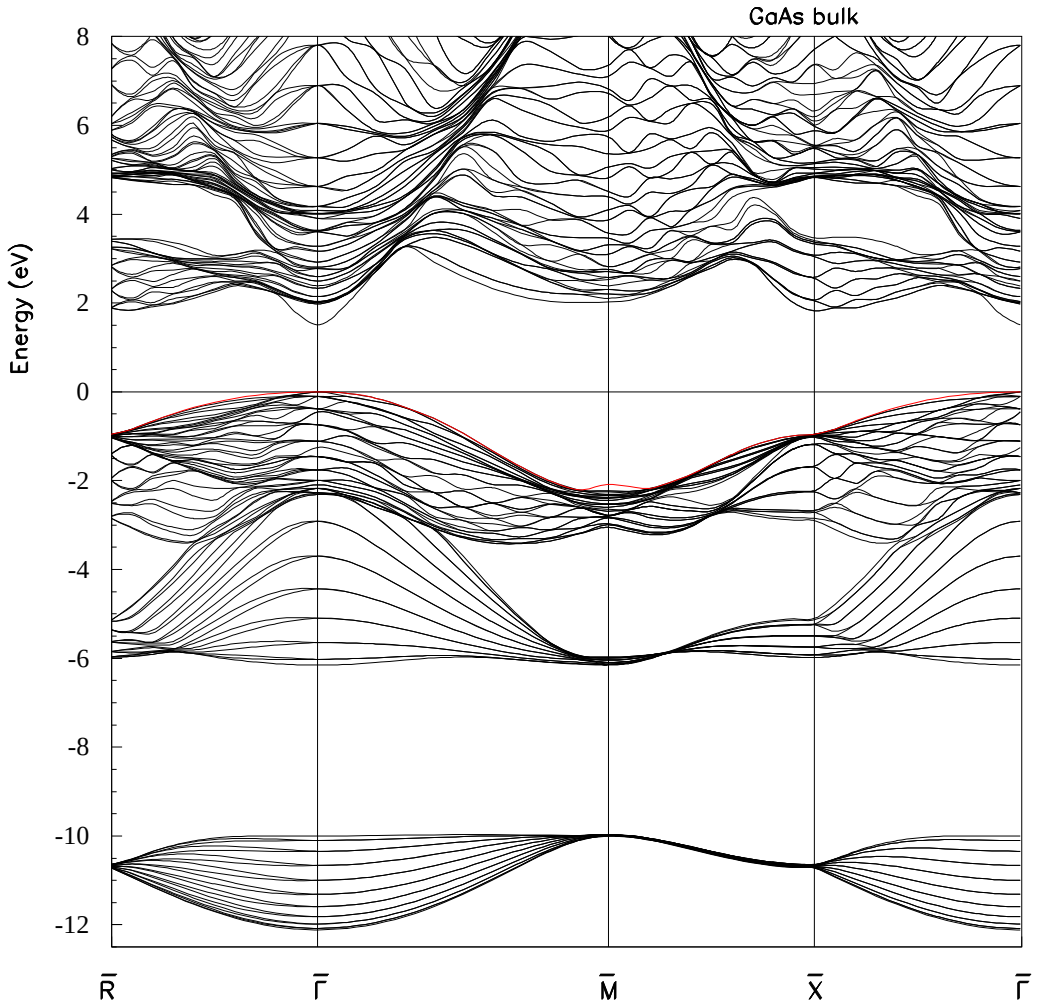

Figure 2.4: Bulk band structure of a $(GaAs)_{20}$, i.e. p=10, obtained by folding the GaAs bands in Fig. 2.2 along the high symmetry directions of the tetragonal Brillouin zone. The energy zero is taken at the valence band maximum of bulk GaAs. The dotted top valence band is the Fermi level.

conduction state in $\bar{\Gamma}$ at different superlattice sizes [45, 47, 48]. The coupling between $\bar{\Gamma}(\Gamma_{1c})$ and $\bar{\Gamma}(X_{1c,3c})$ states, i.e. the lowest superlattice conduction states at $\bar{\Gamma}$, which come respectively from Γ and X band-edge states of the constituent bulk materials (see the state labels in Figs. 2.2 and 2.3), leads to a reciprocal repulsion between these two levels. Since all zinc-blend X states lie higher in energy than the GaAs Γ conduction minimum, this symmetry coupling pushes down the $\bar{\Gamma}(\Gamma_{1c})$ state, contrasting the upward shift due to confinement. This competition between potential symmetry and kinetic energy effects results in a non-monotonic $\bar{\Gamma}\left(\Gamma_{1c}\right)/\bar{\Gamma}\left(X_{1c}\right)$ splitting for small p. For large periods, symmetry induced repulsions rapidly attenuate, as the weight function W_α becomes smaller, and confinement effects dominate, even though they also decrease as the well width grows. All this determines the transition form a pseudo-direct (i.e. $\bar{\Gamma}\left(X_{1c}\right)$ is the conduction minimum) to a direct (i.e. $\bar{\Gamma}\left(\Gamma_{1c}\right)$ is the conduction minimum) gap at a superlattice period $p = 11 \pm 1$ [49].

We have also determined (see the table in Fig. 2.5) the electron effective masses m^* from the definition:

$$E(\mathbf{k}) - E_0 = \frac{\hbar^2 \left|\mathbf{k} - \mathbf{k}_0\right|^2}{2m^*}, \tag{2.13}$$

where E_0 is the energy of the band extreme at $\mathbf{k}_0$ and $\mathbf{k}$ must not be too far from $\mathbf{k}_0$, in order to validate the parabolic approximation. The quality of the obtained effective masses is particularly important, in view of describing correctly another important effect, besides the mixing effects: the carrier confinement. We give in Fig. 2.5 a schematic image of the confinement of an electron in a multilayered structure. We consider an electron in a conduction band (but the same considerations are valid for a hole in a valence band) in a GaAs/AlAs superlattice, lying in a state which comes from a bulk band edge state: it can be represented by a particle of mass m^* which feels a rectangular potential, given by the level alignment of the bulk energy bands along the growth direction z (see the schematic picture in Fig. 2.5). This corresponds to nothing more than the simple quantum mechanic exercise of a particle in a periodic repetition of boxes. The AlAs layers act as barriers for the carriers (both electrons in conduction band and holes in valence band), confined in the wells made of GaAs. The result is a shift of both the valence and the conduction energy levels, which makes the gap wider. The effective mass values are related to

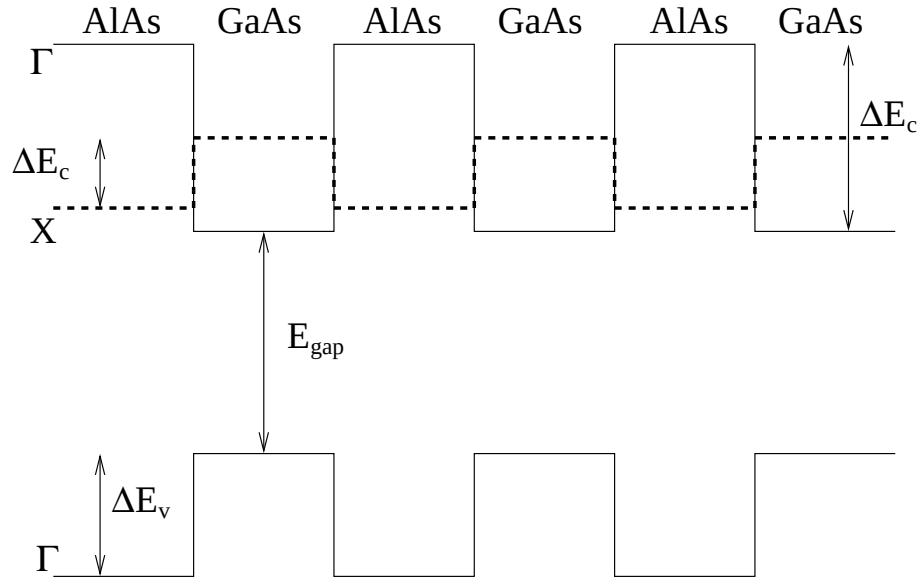

		GaAs	AlAs
E_{gap}	(eV)	1.51	3.03
$m^*_{\Gamma_c}/m_0$		0.10	0.18
$m^*_{\Gamma_{v1}}/m_0$		0.44	0.46
$m^*_{\Gamma_{v2}}/m_0$		0.10	0.17
m^*_X/m_0		2.0	1.0
$\Delta E_v(\Gamma)$	(eV)	0.51	
$\Delta_{\Gamma X}$	(eV)	0.20	
$\Delta E_c(\Gamma)$	(eV)	1.01	
$\Delta E_c(X)$	(eV)	0.31	

Figure 2.5: Conduction and valence band edge profiles in the GaAs/AlAs superlattice. Both Γ and X minima are shown.

the curvature of the bands: the semi-empirical pseudopotentials give satisfactory effective masses if compared to experiments, as discussed in Ref. [44].

Concerning GaAs/vacuum superlattices, the same considerations are valid, except for the fact that there are no AlAs states and thus only GaAs states can mix with each other. For the vacuum barriers are ideally infinite in height, confinement effects are significantly stronger and, accordingly, the band gaps are wider than in GaAs/AlAs systems. If we now compare the GaAs band structure in the tetragonal Brillouin zone with the GaAs/vacuum superlattice band structure in Fig. 2.7, they still show similar dispersions. However, as the GaAs/vacuum superlattice has only half the number of electrons if compared to the bulk GaAs, also the superlattice band structure has only half the number of bulk bands.

2.4 Calculated superlattice electronic levels

Finally, we show the results of the application of the method LCBB to the single-particle band structures of (001) $(\mathrm{GaAs})_p/(\mathrm{AlAs})_p$ and $(\mathrm{GaAs})_p/(\mathrm{vacuum})_p$ superlattices. In practice, the period $d = pa$ has been varied from $4a$ to $20a$. We do not consider smaller supercells because the superlattice electronic states differ more and more from bulk states while the layer width decreases, making the expansion on the bulk states less reliable.

In the case of a GaAs/vacuum superlattice we decide to include the 4 valence bands and the 4 lowest conduction bands in the basis set. In the case of a GaAs/AlAs superlattice the roughest selection is to take both GaAs and AlAs bulk states at each mixed $\mathbf{k}$ and n, orthonormalizing at the end the basis set obtained. As GaAs and AlAs band structures are very similar except for the lowest conduction band (see again Figs. 2.2 and 2.3 and details of calculation below), we have verified that it is enough to include only GaAs states for n from 1 to 8 together with the 5^{th} band of AlAs (i.e. the lowest conduction band). The resulting set must be orthonormalized. It can easily be seen that the final dimension of the basis is always small (40×9 for the largest supercell). When a sufficiently large number of bulk states is used as a basis set for the LCBB method, the results must converge to those obtained with a direct diagonalization of the Hamiltonian for the corresponding number of plane

waves. A comparison of LCBB results with the conventional supercell approach was presented in Ref. [29]. Here we have performed a convergence test, which consists in calculating the energy levels with four different bulk basis sets of increasing size. Selected results are shown in Tab. 2.1 for $(GaAs)_{10}/(AlAs)_{10}$ and $(GaAs)_6/(AlAs)_6$ superlattices. As far as valence states are concerned, dependence of the energy levels on the basis set is below 10^{-3} eV; for the lowest conduction levels the dependence on the basis set is generally below 0.05 eV, and falls below 10^{-2} eV when the 5^{th} band of AlAs is included in the basis. The results of Tab.2.1 justify the use of basis 3), namely $n = 1$ to 8 for GaAs and $n = 5$ for AlAs.

Table 2.1: Comparison of energy levels (in eV) at the symmetry points for $(GaAs)_n/(AlAs)_n$ superlattices with period $n = 6$ and $n = 10$. We show highest valence levels and lowest conduction levels: the energy zero is taken at the valence band maximum. Four different choices are considered for the basis set: 1) five GaAs bands for n from 1 to 5, no AlAs bands; 2) eight GaAs bands for n from 1 to 8, no AlAs bands; 3) eight GaAs bands for n from 1 to 8, the 5th band of AlAs; 4) eight GaAs bands for n from 1 to 8, four AlAs bands for n from 5 to 8.

basis	valence band maximum					conduction band minimum				
	$\bar{\Gamma}$	$\bar{Z}$	$\bar{R}$	$\bar{M}$	$\bar{X}$	$\bar{\Gamma}$	$\bar{Z}$	$\bar{R}$	$\bar{M}$	$\bar{X}$
n=10										
1)	0.0000	-0.0004	-0.8992	-2.1127	-0.8992	1.8318	1.8303	2.0069	1.9048	2.0063
2)	0.0000	-0.0004	-0.8990	-2.1129	-0.8990	1.8173	1.8190	2.0057	1.9014	2.0049
3)	0.0000	-0.0004	-0.8990	-2.1131	-0.8990	1.7949	1.8008	1.9911	1.8588	1.9881
4)	0.0000	-0.0003	-0.8985	-2.1130	-0.8985	1.7884	1.7957	1.9904	1.8590	1.9874
n=6										
1)	0.0000	-0.0118	-0.8488	-2.0968	-0.8489	1.9766	1.9940	2.1730	1.9961	2.1561
2)	0.0000	-0.0115	-0.8481	-2.0970	-0.8482	1.9526	1.9567	2.1694	1.9940	2.1535
3)	0.0000	-0.0115	-0.8481	-2.0973	-0.8482	1.9062	1.9109	2.1451	1.9618	2.1053
4)	0.0000	-0.0113	-0.8468	-2.0967	-0.8468	1.9042	1.9098	2.1440	1.9626	2.1043

In Figs. 2.6 and 2.7 we show the superlattice energy bands for p=10: the electron energy levels are plotted along the highest symmetry lines in the tetragonal Brillouin zone. All trends in the superlattice states obtained by LCBB method were shown to be reproduced [29], with a surprising accuracy (10-20 meV) and a small

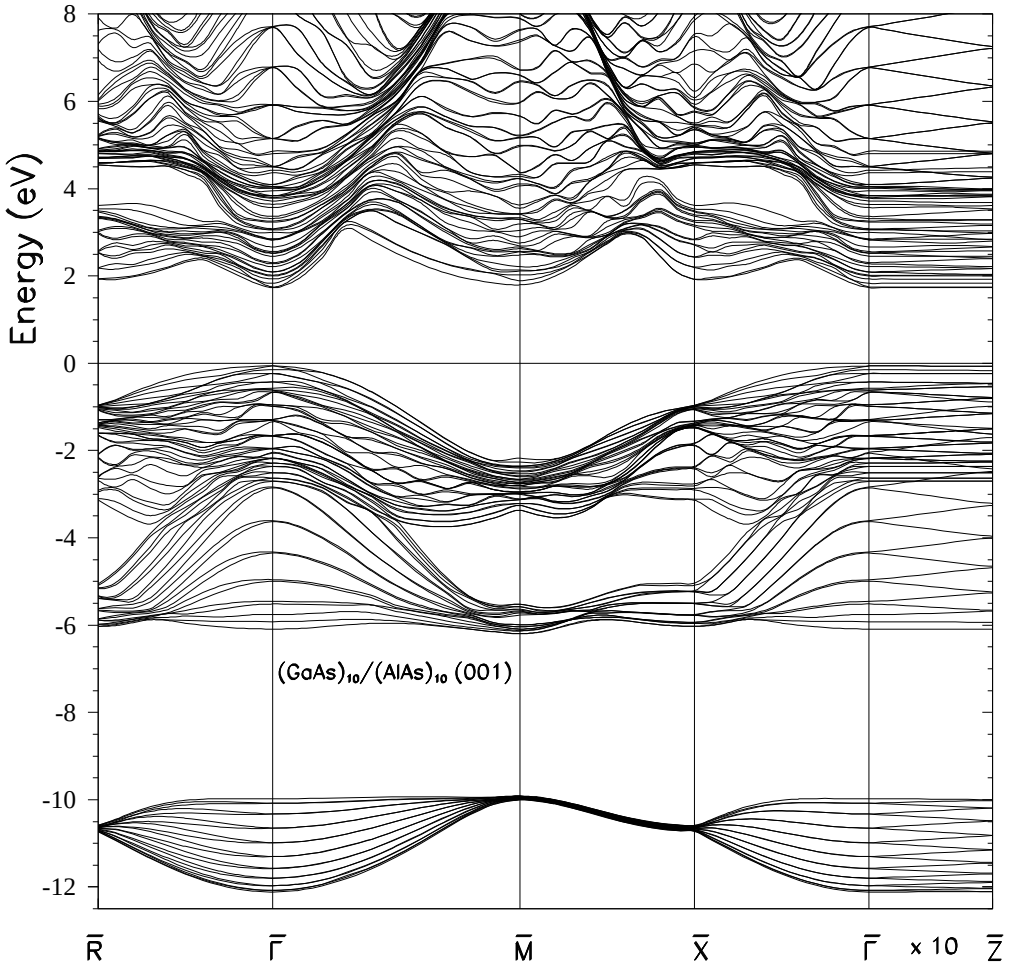

Figure 2.6: Band structure of a $(GaAs)_{10}/(AlAs)_{10}$ (001) superlattice along the high symmetry directions. The length of the $\bar{\Gamma} - \bar{Z}$ line is multiplied by ten for clarity. The energy zero is taken at the bulk GaAs valence band maximum.

computational effort, down to thin superlattices and up to large periods. Since $2p$ **k**-points in the fcc Brillouin zone are always folded onto the same point **q** in the smaller tetragonal Brillouin zone, the number of occupied superlattice bands is $2p$ times the number of bulk bands for GaAs/AlAs, p times the number of bulk bands for GaAs/vacuum superlattices. The dispersion along the direction $\bar{\Gamma}$-$\bar{M}$ is similar to the dispersion along the direction Γ-X in the bulk, while the other two directions $\bar{\Gamma}$-$\bar{R}$ and $\bar{\Gamma}$-$\bar{X}$ have no counterpart in the band structures of Figs. 2.2 and 2.3. In GaAs/AlAs, the dispersion along the growth direction $\bar{\Gamma}$-$\bar{Z}$ is much smaller than in the other directions, as expected for superlattice minibands; in GaAs/vacuum the bands along $\bar{\Gamma}$-$\bar{Z}$ are flat as tunneling through the vacuum has a negligible effect.

We have discussed how the main differences in the superlattice band structures compared to the bulk (compare again to Fig. 2.4) can be interpreted in terms of zone folding and quantum confinement effects; it is also interesting to compare the band structures of the two superlattices. The superlattice gaps are larger than the bulk gaps: in particular the GaAs/vacuum gaps are larger than the GaAs/AlAs ones, as a result of a stronger confinement; moreover the superlattice band gap widths increase as the superlattice period decreases. The lowering in the crystal symmetry is responsible for the removal of level degeneracies: as an example in the GaAs/AlAs D_{2d} superlattice the threefold degenerate valence states at Γ (spin-orbit is neglected) are split in a twofold-degenerate and a non-degenerate state, while in the GaAs/vacuum C_{2v} superlattices the degeneracy is completely removed.

In GaAs/vacuum bands we clearly see the appearance of states lying in the forbidden energy gaps. The lowest one lies in the gap from -10 to -6 eV, while two other ones lie in the optical gap from 0 to about 2 eV. A fourth state can be recognized at -5 eV around the point $\bar{M}$, while in other regions of the Brillouin zone it resonates with the energy bands. Indeed, four surface states or resonances are expected from the presence of two dangling bonds at the two interfaces of each GaAs layers. We can identify the surface states by studying the behavior of the probability $|\psi|^2$ to find an electron along the growth direction z, averaged over the in-plane x, y coordinates. Taking as an example the conduction miniband states at Γ, where the potential profile is characterized by 0.5 eV deep wells in GaAs layers, we observe (see Fig. 2.8) that an electron in a surface state ($j = 39$ in the exemplified case)

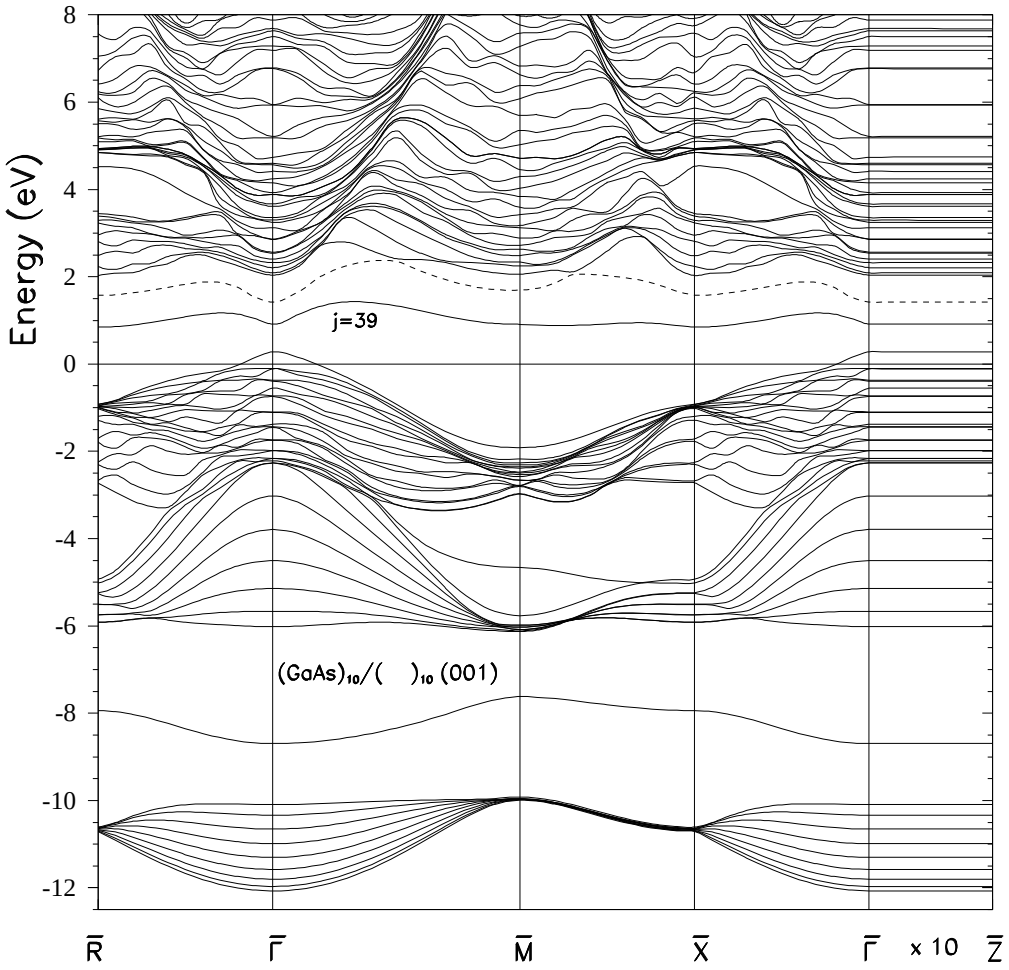

Figure 2.7: Band structure of a $(GaAs)_{10}$/ $(vacuum)_{10}$ (001) superlattice along the high symmetry directions. The energy zero is taken at the bulk GaAs valence band maximum. The uppermost occupied band is number 40 (dotted).

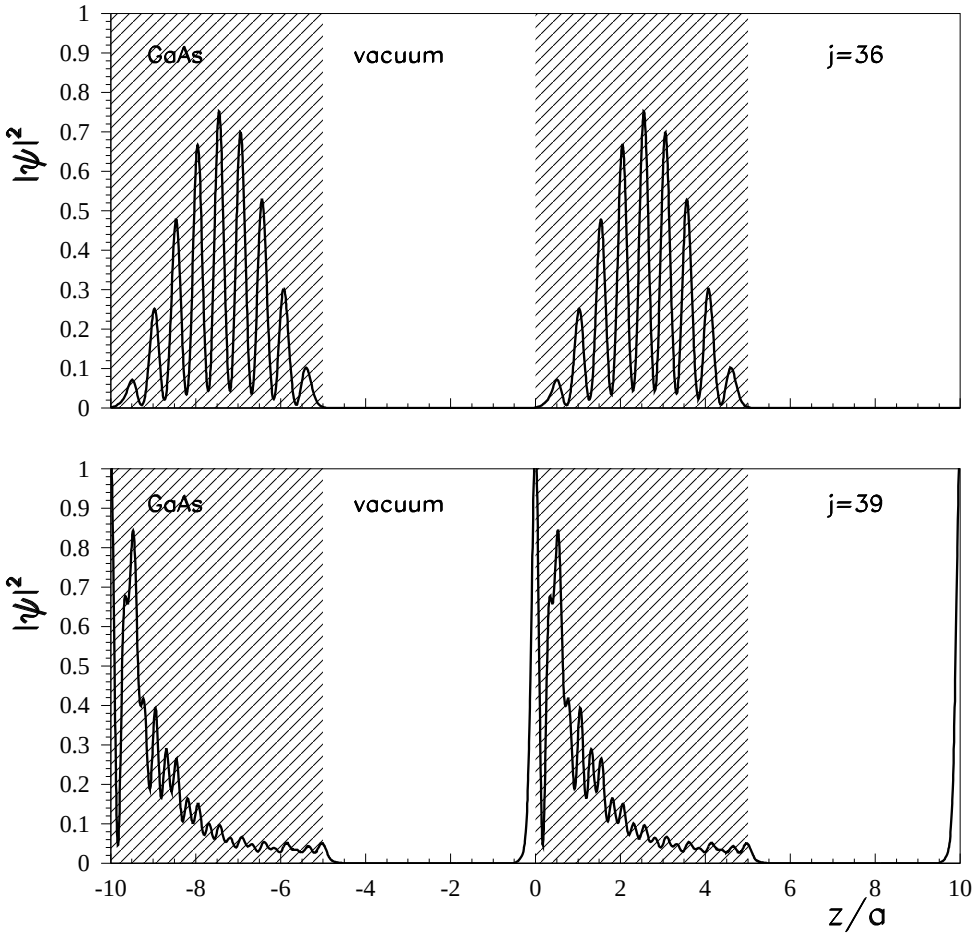

Figure 2.8: Planar averaged probability along the growth direction z to find an electron at Γ in the 36th and the 39th band of a $(\mathrm{GaAs})_{10}/(\mathrm{vacuum})_{10}$ (001) superlattice.

has a high probability to be localized on the surface and a decaying probability to enter the GaAs layer; on the other hand an electron in a bulk state ($j = 36$ in the figure) has an oscillating probability to be found in the GaAs layers. Both states are obviously evanescent in vacuum. From the position of the uppermost occupied band ($j = 40$) it follows that GaAs/vacuum superlattices have a metallic behavior: this is an artifact of the model, as our aim is to simulate insulating multilayers made of GaAs and a wide-gap oxide or H-saturated free standing films. When calculating optical spectra, we will get rid of the problem by excluding surface states as initial or final states in interband transitions. This simulates the formation of interface

states or defects in a GaAs/oxide superlattice, which would saturate the dangling bonds. The surface resonance cannot be easily eliminated, but it produces small effects on the spectra, since it lies deep in the valence band.

In this chapter we have discussed the LCBB approach to study the superlattice band structures. This approach, which expands the electronic states of the superlattice on the basis of bulk states, calculated by semi-empirical pseudopotentials, is found to be adequate and practical for superlattices characterized by medium to intermediate periods. It has revealed to be particularly suitable for calculating how the band structures of the bulk materials are modified when an artificial confining potential is applied. We have written a computational code to calculate the electronic states in superlattices. We have applied the code to study the evolution of a bulk state into a superlattice state, gaining a clear insight on the role played by the confinement, the bulk states-coupling and the reduction of the symmetry, all involved in the formation of a superlattice. The superlattice gaps result larger: in particular the GaAs/vacuum gaps are larger than the GaAs/AlAs ones. Moreover, the superlattice gaps become larger when the confinement increases, as a consequence of the size reduction. The lowering in the crystal symmetry and the mixing of bulk states induce a modification of the energy levels and remove level degeneracies.

Chapter 3

Ab-initio calculations of superlattice band structures

In this chapter we present our second choice for band structure calculations of bulk and nanostructure semiconductor systems. We move from the semi-empirical approach to a well-known first principle theory: the Density Functional Theory (DFT). If compared to the LCBB method presented in the previous chapter, the first striking difference in the *ab initio* DFT approach is the total absence of experimental inputs. Within a pseudopotential approach, starting from the mere knowledge of the atomic numbers, atomic pseudopotentials can be fitted to calculations for the isolated atoms. Next, an hypothesis on the geometric structure of the system is all we need to build up the Hamiltonian operator. The most stable structure can be found among all the different hypothesized structures, by searching for the minimum of the calculated total energy. It is evident that the development of *ab initio* techniques has given a much stronger predictive character to the theory of electronic properties in the matter. Details on the procedure we have followed to construct norm-conserving *ab initio* pseudopotentials can be found in Appendix B. In the following sections, at first, we will present the fundamentals of the Density Functional Theory. They are intended to be a practical guide to accompany the immediately successive exposition of our results, namely the electronic ground state properties and the band structures of bulk (i.e. GaAs and AlAs) and superlattice (i.e. GaAs/AlAs) systems. We have analyzed the structural properties and the electronic band structures of

GaAs and AlAs crystals. Results in agreement with both the experiment and analogous calculations existing in literature are a reassuring proof about the quality of the norm-conserving pseudopotentials we have built. In addition, a good bulk band dispersion is promising concerning the quality of further calculations of the optical response. However, we are essentially interested in $(\mathrm{GaAs})_p/(\mathrm{AlAs})_p$ superlattices. For superlattices with a very short period, the expansion over bulk states becomes unreliable (unless using a very large basis) and LCBB calculations have not been pushed to periods p smaller than 4. Some results for the band structure of small to medium size ($1 \leq p \leq 8$) systems will be presented in the last section. Analogous *ab initio* calculations are available in literature only for the smallest periods p. Thus, we will focus on the comparison of the DFT band structure for the superlattice period p=8 to the corresponding semi-empirical band structure.
We will adopt atomic units, as it is usually done in literature: $\hbar = e^2 = m_e = 1$. The spin and space coordinates are abbreviated by $\mathbf{x} \equiv (\mathbf{r}, \sigma)$.

3.1 Density Functional Theory

The Density Functional Theory (DFT), in the Kohn-Sham formalism, provides a powerful computational scheme, which allows to determine exactly the ground-state properties even of complex systems of interacting particles, simply solving a single-particle-like equation. Let us consider a system made of N fermions (let us say electrons), interacting with each other via the Coulomb potential $v(\mathbf{r}_i, \mathbf{r}_j) = 1/|\mathbf{r}_i - \mathbf{r}_j|$. The system experiences an external potential $w(\mathbf{r})$, which is supposed at the moment to be time-independent. In the specific case of electrons in an infinite periodic solid, this external potential is due to the Coulomb interaction between electrons and ion cores, fixed on the lattice sites. The Hamiltonian operator

$$\begin{aligned} H &= T + W + V \\ &= \sum_{i=1}^{N} \left(-\frac{1}{2}\nabla^2_{\mathbf{r}_i} + w(\mathbf{r}_i) \right) + \frac{1}{2}\sum_{i \neq j}^{N} v(\mathbf{r}_i, \mathbf{r}_j) \end{aligned} \tag{3.1}$$

is the main ingredient in the time-dependent Schrödinger equation, which determines the time evolution of the system:

$$H(\mathbf{x}_1, \mathbf{x}_2, \ldots, \mathbf{x}_N)\, \Psi(\mathbf{x}_1, \mathbf{x}_2, \ldots, \mathbf{x}_N, t) = i\frac{\partial \Psi(\mathbf{x}_1, \mathbf{x}_2, \ldots, \mathbf{x}_N, t)}{\partial t}\,. \tag{3.2}$$

The stationary states are the eigenstates of the time-independent Schrödinger equation:

$$H\left(\mathbf{x}_1, \mathbf{x}_2, \ldots, \mathbf{x}_N\right) \psi\left(\mathbf{x}_1, \mathbf{x}_2, \ldots, \mathbf{x}_N\right) = E\psi\left(\mathbf{x}_1, \mathbf{x}_2, \ldots, \mathbf{x}_N\right) . \tag{3.3}$$

An analytical solution of the Eq. (3.3) is not feasible, except for some extremely simple model systems. Among the variety of possible approaches to tackle the problem, Thomas and Fermi [50, 51] were the first to designate the charge density $\rho\left(\mathbf{r}\right)$, instead of the many-body wavefunction, as the basic quantity to describe the ground state properties of the system. The advantage is evident: the electron density,

$$\rho\left(\mathbf{r}\right) = N \int d\mathbf{x}_2 \ldots \int d\mathbf{x}_N \psi^*\left(\mathbf{r}, \mathbf{x}_2, \ldots, \mathbf{x}_N\right) \psi\left(\mathbf{r}, \mathbf{x}_2, \ldots, \mathbf{x}_N\right) , \tag{3.4}$$

is much easier to manage: it reduces the degrees of freedom from $3N$ to 3 and it is a measurable physical quantity.

3.1.1 The Hohenberg-Kohn theorem

The formal bases of DFT are the theorems formulated in 1964 by Hohenberg and Kohn [52]. The original proof is valid for a non-degenerate ground state and a w-representable particle density, i.e. the ground state density belongs to a system which undergoes an external local potential w. For the proofs of the theorems and their generalization (to, e.g., degenerate ground states, bosons, non-adiabatic systems, magnetic systems, fully relativistic systems, superconducting systems, N-representation of the particle density, etc. ...) we suggest to see Ref. [53]. Here we present the physical contents of the original theorems.

1st HK Theorem: Let us consider a system of N electrons, described by the Hamiltonian:

$$H = \sum_{i=1}^{N} \left(-\frac{1}{2}\nabla_{\mathbf{r}_i}^2 + w\left(\mathbf{r}_i\right) \right) + \frac{1}{2} \sum_{i \neq j}^{N} v\left(\mathbf{r}_i, \mathbf{r}_j\right) . \tag{3.5}$$

The electrons are thus subjected to an external potential $w\left(\mathbf{r}\right)$ and the ground state charge density is $\rho_0(\mathbf{r})$. If we substitute the potential $w'\left(\mathbf{r}\right)$ for the potential $w\left(\mathbf{r}\right)$ in 3.5 and we observe that the new electron density $\rho_0'(\mathbf{r})$, relative to the ground state, is equal to $\rho_0(\mathbf{r})$, then $w\left(\mathbf{r}\right)$ and $w'\left(\mathbf{r}\right)$ can only differ by

a constant:

$$w'(\mathbf{r}) = w(\mathbf{r}) + \text{const}\,. \tag{3.6}$$

2nd HK Theorem: Let us define the energy functional of the density $E[\rho]$ in the form

$$\begin{aligned} E[\rho] &= \langle N| -\frac{1}{2}\nabla^2_{\mathbf{r}_i} + \frac{1}{2}\sum_{i\neq j}^{N} v(\mathbf{r}_i,\mathbf{r}_j)\,|N\rangle + \int w(\mathbf{r})\,\rho(\mathbf{r})\,d\mathbf{r} \\ &= F[\rho] + \int w(\mathbf{r})\,\rho(\mathbf{r})\,d\mathbf{r}\,, \end{aligned} \tag{3.7}$$

where F is a universal functional of the density. Once the external potential $w(\mathbf{r})$ has been fixed, the energy functional $E[\rho]$ has its minimum, the ground state energy E_0, at the physical ground state density $\rho_0(\mathbf{r})$:

$$E_0 = E[\rho_0]\,. \tag{3.8}$$

The first theorem states that there is a bijective relation between the external potential $w(\mathbf{r})$ (to within a constant) and the ground state density $\rho(\mathbf{r})$: this implies that the Hamiltonian is completely described by knowing the ground state density, thus all the ground state properties of the N-electrons system (e.g. the total energy) are functionals of $\rho(\mathbf{r})$. The Hohenberg-Kohn (HK) theorems have the limited purpose to prove that a universal functional of the electron density exists, they do not derive its actual expression. A direct minimization of the functional (3.7) is usually not applicable, because no good expression for the kinetic energy as a functional of ρ is known, except for simple metals. The Kohn-Sham (KS) scheme, a reformulation of the theory based on the KS orbitals instead of the mere density, is the starting-point of most of the actual calculations.

3.1.2 The Kohn-Sham scheme

The variational scheme proposed by Kohn and Sham [54] is an useful tool to clarify the physical contents of the theory. Let us consider the system of N interacting electrons, described by the Hamiltonian (3.1):

$$H = T + W + V\,.$$

We introduce now an auxiliary system composed by N non-interacting particles in an external potential W', described by the one-particle Hamiltonian H':

$$H' = T + W' \,. \tag{3.9}$$

The KS scheme is based on the hypothesis that it exists such a local potential W', that makes the ground state electronic density $\rho'(\mathbf{r})$ of the non-interacting system equal to the ground state electronic density $\rho(\mathbf{r})$ of the interacting system:

$$\rho\left(\mathbf{r}\right) = \rho'\left(\mathbf{r}\right) \,. \tag{3.10}$$

It is clear that if a non-interacting system with the required characteristics exists, then, according to the HK theorems, it must be unique. At the moment, we assume that it is always possible to find such a potential W'; its existence is formally proved for w-representable densities (see Ref. [55]) and generalized to N-representable densities (see Ref. [53]). The charge density of the non-interacting system can be expressed as a sum of single-particle charge densities; this holds also for the real charge density thanks to the equality (3.10):

$$\rho\left(\mathbf{r}\right) = \rho'\left(\mathbf{r}\right) = \sum_{i=1}^{N} \left|\phi_i\left(\mathbf{r}\right)\right|^2 \,. \tag{3.11}$$

The sum includes the eigenfunctions ϕ_i relative to the N lower eigenvalues, coming from the solution of the Schrödinger equation for the non-interacting system:

$$\left[-\frac{1}{2}\nabla^2_{\mathbf{r}_i} + w'\left(\mathbf{r}\right)\right]\phi_i\left(\mathbf{r}\right) = \epsilon_i\phi_i\left(\mathbf{r}\right) \,. \tag{3.12}$$

The HK functional associated to the auxiliary system is:

$$E'\left[\rho\right] = T'\left[\rho\right] + \int w'\left(\mathbf{r}\right)\rho\left(\mathbf{r}\right)d\mathbf{r}\,, \tag{3.13}$$

where also the kinetic energy of the non-interacting electrons $T'\left[\rho\right]$ is a functional of the density $\rho(\mathbf{r})$, as a consequence of the fact that the eigenfunctions ϕ_i are functionals of the density:

$$T'\left[\rho\right] = \sum_{i=1}^{N}\int \phi_i^*\left(\mathbf{r}\right)\left[-\frac{1}{2}\nabla^2_{\mathbf{r}_i}\right]\phi_i\left(\mathbf{r}\right)d\mathbf{r}\,. \tag{3.14}$$

We can now rewrite the HK functional for the real system in a more profitable way:

$$E\left[\rho\right] = T'\left[\rho\right] + \frac{1}{2}\int d\mathbf{r}\int d\mathbf{r}'\rho\left(\mathbf{r}\right)\rho\left(\mathbf{r}'\right)v\left(\mathbf{r},\mathbf{r}'\right) + \int w\left(\mathbf{r}\right)\rho\left(\mathbf{r}\right)d\mathbf{r} + E_{xc}\left[\rho\right] \,. \tag{3.15}$$

The kinetic energy $T'[\rho]$ is now the kinetic energy of a non-interacting electron gas and the second term gives the Coulomb energy due to the classic interaction of an electron gas of density $\rho(\mathbf{r})$. By comparing the expression (3.7) and (3.15), we get a definition for the functional E_{xc}, which accounts for the many-body exchange and correlation effects among electrons:

$$E_{xc}[\rho] = F[\rho] - \frac{1}{2}\int d\mathbf{r}\int d\mathbf{r}'\rho(\mathbf{r})\,\rho(\mathbf{r}')\,v(\mathbf{r},\mathbf{r}') - T'[\rho]\ . \tag{3.16}$$

The form of the still unknown external potential W' can be fixed minimizing the energy functional $E[\rho]$ in (3.15), by imposing that his first variation vanishes:

$$\delta E[\rho] = 0\,. \tag{3.17}$$

It results that the searched potential for the non-interacting system is a function of the real external potential, the Coulomb potential and the so called exchange-correlation (xc) potential:

$$w'(\mathbf{r}) = w(\mathbf{r}) + \int d\mathbf{r}'\rho(\mathbf{r}')\,v(\mathbf{r},\mathbf{r}') + v_{xc}([\rho],\mathbf{r})\ , \tag{3.18}$$

where the xc potential is defined as

$$v_{xc}([\rho],\mathbf{r}) = \frac{\delta E_{xc}[\rho]}{\delta\rho(\mathbf{r})}\,. \tag{3.19}$$

If we now introduce the potential w' from Eq. (3.18) into the Schrödinger equation (3.12), we obtain the Kohn and Sham equations:

$$h_{KS}^{eff}\ \phi_i = \left[-\frac{1}{2}\nabla^2 + w'\right]\phi_i = \epsilon_i\ \phi_i\,. \tag{3.20}$$

The KS equations (3.20) and the expression of $w'(\mathbf{r})$ (3.18) have both a functional dependence on $\rho(\mathbf{r})$, which imposes a simultaneous self-consistent solution. The exchange-correlation term is a functional of the density, local in space, which makes the resolution of the equations easier than the solution of e.g. analogous Hartree-Fock equations. Looking at the form of the one-body potential $w'(\mathbf{r})$, we can see that the external ionic attractive potential w is modified by the screening due to the interaction between charges: this suggests to interpret it as the effective potential felt by one electron in the mean field created by the other electrons. Thanks to its construction, the effective potential $w'(\mathbf{r})$ of the non-interacting system gives the

correct density $\rho(\mathbf{r})$ of the interacting system. This quantity, together with the total energy of the electron system, has a real physical meaning within the KS scheme. The solutions of the KS equations, i.e. the one-particle wavefunctions ϕ_i and the eigenvalues ϵ_i, are instead, strictly speaking, nothing more than the eigenstates and energy levels of the non-interacting system. We remark that the HK theorems concern only the ground state properties of stationary systems: it is not correct to extract from the DFT, at least without further formal justifications, any information about the excited states or about time-dependent transitions. Nevertheless, we will see that the theory has proved to be a good basis for a perturbation approach and for time-dependent extensions, aiming at treating this kind of problems.

This scheme allows in principle the exact determination of the ground state energy. In practice, it is inevitable to make an approximation for the xc potential. The exchange-correlation functional is a universal functional, in the sense that once it is known for a model system, it can be simply transferred to all the others systems with the same internal interaction potential, whatever the external field is. Unfortunately, there are no solved models for arbitrary densities $\rho(\mathbf{r})$. The only available solution is the extremely accurate calculation for the electron jellium at the constant density $\rho(\mathbf{r}) = \rho_0$ [56, 57, 58]. Being the exchange-correlation energy E_{xc} in general unknown, the possibility to describe physical systems relies on the effective substitution of a simple and realistic approximation for this functional.

3.1.3 The Local Density Approximation

The Local Density Approximation (LDA) consists in expressing the functional dependence of the exchange-correlation energy on the density with a simple dependence on the local value of the density. It is defined by:

$$E_{xc}^{LDA}[\rho] = \int \rho(\mathbf{r})\, \epsilon_{xc}(\rho(\mathbf{r}))\, d\mathbf{r}\,, \tag{3.21}$$

where ϵ_{xc} is the exchange-correlation energy for a particle in an interacting homogeneous electron gas, which is known with a very satisfactory precision from many-body Monte Carlo numerical simulations [56, 57, 58]. The correlation energy occurring in our calculations has been parametrized as follows [57]:

$$\epsilon_{xc}^{hom}[\rho(\mathbf{r})] = \gamma/\left(1 + \beta_1\sqrt{r_s} + \beta_2 r_s\right)\,, \tag{3.22}$$

for $r_s \geq 1$, where

$$\rho(\mathbf{r}) = \left(\frac{4}{3}\pi r_s^3\right)^{-1}, \tag{3.23}$$

and

$$\gamma = -0.14230\,, \qquad \beta_1 = 1.05290\,, \qquad \beta_2 = 0.3334\,. \tag{3.24}$$

Since the LDA is exact in case of homogeneous systems, it has been thought to be suitable to describe those physical systems where the charge density varies slowly, like metals. This is a strong restriction, but the approximation has surprisingly turned out to be valid in a vaster range of circumstances, like in semiconductors. Such an unexpected success is due to the fact that the LDA, even in case of strongly inhomogeneous systems, satisfies exactly some sum rules which must hold for the real pair correlation function of the system. In general, quantities derived by comparing total energies, like ground state geometries, phonon frequencies, and moments of the density are well reproduced [59] within this simple approximation. These topics will be discussed further in Section 3.3. There are some possible generalizations of the LDA: including a correction dependent on the gradient of the density $\rho(\mathbf{r})$, as already suggested by Hohenberg and Kohn [52], we get the Gradient Density Approximation (GDA). Some other approaches beyond LDA, like the Generalized Gradient Approximation (GGA) [60, 61], the Average-Density Approximation (ADA), and the Weighted Density Approximation (WDA) [62], have been object of increasing interest in the last years. However exactly satisfied within the LDA, the sum rules are not satisfied within its generalizations. That's why an improvement of the LDA is not as straightforward as it might appear [59]. It is not clear yet if it exists an alternative non-local scheme which is able to guarantee better results if compared to the LDA. Up to now the LDA is widely applied in literature. The extension to spin-polarized systems is called Local Spin-Density Approximation (LSDA). In this work, however, we will always deal with spin-paired electrons.

3.2 Technical aspects

3.2.1 Plane wave basis

When studying an infinite system composed by a repeated periodic unit, both a cell or a supercell, the most natural choice for the expansion of the wavefunctions is the plane wave representation $\left\{e^{i\mathbf{G}\cdot\mathbf{r}}\right\}_{\mathbf{G}\in RL}$. In fact, according to the Bloch theorem, the single electron wavefunction can be expanded as follows:

$$\phi_{n,\mathbf{k}}(\mathbf{r}) = \frac{1}{\sqrt{\Omega}} e^{i\mathbf{k}\cdot\mathbf{r}} \sum_{\mathbf{G}} c_{n,\mathbf{k}}(\mathbf{G})\, e^{i\mathbf{G}\cdot\mathbf{r}}\,, \tag{3.25}$$

where Ω is the volume of the Wigner-Seitz cell (or of the supercell in case of superlattices) and $\mathbf{G}$ are the reciprocal lattice vectors. The wave-vectors $\mathbf{k}$, lying inside the first Brillouin zone, label the electronic states together with the band index n.

The choice of a plane wave basis presents some advantages:

- They simplify the evaluation of derivatives and integrals, making easier to calculate the matrix elements of the Hamiltonian.
- They allow the application of Fast Fourier Transform (FFT) formalism, allowing to move rapidly from the direct to the reciprocal space and vice-versa.
- They form a complete and orthonormal set.
- For open systems with some "vacuum", like cluster and surfaces or, in a future perspective, GaAs/vacuum superlattices, it is convenient that the set does not depend on the atomic positions.
- The truncation of the in principle infinite basis set is given by a cutoff in energy:

  $$\frac{1}{2}|\mathbf{k}+\mathbf{G}|^2 \leq E_{cutoff}\,, \tag{3.26}$$

  which is linked to the number of plane waves N_{PW} in the basis by the relation

  $$N_{PW} \simeq \Omega\,(E_{cutoff})^{3/2}\,. \tag{3.27}$$

  The achievement of convergence for total energy calculations can be controlled without ambiguity by increasing the cutoff.

A plane wave basis set is particularly suitable in case of a pseudopotential approach (see Appendix B). In such a case only the valence wavefunctions, which are less localized than the core ones, have to be calculated. Localized basis sets, on the other hand, should be preferred when one is interested in highly localized electronic states (e.g. core atomic-like states).

In our calculations, the convergence has been achieved working with plane waves up to a kinetic energy cutoff of 25 Ry for both GaAs and AlAs bulk crystals. Concerning the superlattices GaAs/AlAs, an higher cutoff of 35 Ry is needed to achieve the same degree of accuracy. We have proved that these sets guarantee an error within a few meV both for the total energy and for the KS eigenvalues.

3.2.2 Sets of k-points for integration over the Brillouin zone

All sums over the allowed **k**-points in the Brillouin zone become integrals in the limit of an infinite periodic crystal. In particular, the central quantity which defines the system, the charge density,

$$\rho(\mathbf{r}) = \frac{1}{N_{\mathbf{k}}} \sum_{n}^{occ} \sum_{\mathbf{k}}^{BZ} |\phi_{n,\mathbf{k}}(\mathbf{r})|^2 \ , \tag{3.28}$$

is transformed in:

$$\rho(\mathbf{r}) = \frac{\Omega}{(2\pi)^3} \int_{BZ} d\mathbf{k} \sum_{n}^{occ} |\phi_{n,\mathbf{k}}(\mathbf{r})|^2 \ . \tag{3.29}$$

To perform a numerical calculation, in practice, the integral must be turned back into a sum over a set of weighted **k**-points. If the function to be integrated, as it happens in expression (3.29), is symmetric in the reciprocal coordinates, these points, called *special points* can be chosen exploiting the symmetry properties. The introduction of the concept of special points is due to Baldereschi [63]. Then, Chadi and Cohen [64] and, later, Monkhorst and Pack [65] have elaborated his idea. Their methods are now widely used. In comparison with an arbitrary grid of points, which does not reflect the symmetries of the Brillouin zone, the special points reduce drastically the number of points needed to attain a specific precision in calculating integrals.

In the numerical computation of charge densities for bulk fcc GaAs and AlAs we have performed sums over a grid of 10 special **k**-points in the irreducible part of the Brillouin zone. This grid of points has been built following the procedure of

Monkhorst and Pack. Regarding the superlattices, we have used the tetrahedron integration scheme, as presented by Jepsen and Andersen [66, 67, 68]. In that case the biggest set which we have employed is a set of 30 **k**-points in the irreducible wedge of the tetragonal reciprocal supercell. The set of special points have been selected to guarantee the convergence of the total energy (the error is always smaller than a few tenths of meV). To solve the integrals occurring in the calculations of optical properties, much more points are needed, as we will precise discussing the convergence of the spectra.

3.3 Results for ground-state properties

The results of DFT-LDA calculations on atoms, molecules and solids (even ionic and covalent solids), collected in the last decades show without uncertainties that this theory is a powerful tool to study the structural properties of the matter.

To perform ground state calculations in this thesis, we have used the pseudopotential plane wave package PWSCF [69], originally developed by Baroni and Giannozzi. This code computes the electronic band structure, the electronic charge density and the total energy of a periodic crystal, characterized by a given Bravais lattice and a given space group symmetry. The algorithm is based on DFT and relies on two basic approximations: the frozen-core approximation (see Appendix B) and the local density approximation (though a gradient correction is available, it has not been used in our calculations). The use of a plane wave basis allows the transformation of the partial differential self-consistent KS equations into an algebraic eigenvalue problem, which is solved thanks to iterative techniques [70]. The choice of a plane wave representation, together with an efficient use of the Fast Fourier Transform, reduces drastically the computational time. The PWSCF code exploits the symmetries of the solid, to cut down the number of operations necessary to obtain the charge density and the total energy with a given precision. The computation of these quantities allows the study of structural (lattice constants, bulk modulus and elastic constants) and dynamical (zone-center phonon frequencies) properties, the study of structural phase transitions and the effects of pressure on the properties of the solids.

The equilibrium structural parameters (i.e. the Bravais lattice type and the lat-

tice parameters in solids) can be determined *ab initio*, by inspecting the minimum of the total energy. In practical applications, the absolute convergence of the total energy is not very important. The most important quantities are the energy differences between different states of the solid. Since energy differences converge more rapidly than the energy itself, it is usually possible to obtain a precision higher than the total energy error (in our case about a few meV). To illustrate this point, we have studied two structural properties: the lattice constant a_0 and the bulk modulus B_0. These quantities are related to the curvature of the function $E(\Omega)$ around the equilibrium volume Ω_0. The theoretical lattice constant has the value a_0, which corresponds to Ω_0, while the bulk modulus is related to the curvature of the energy curve at its minimum:

$$B_0 = -\Omega \left.\frac{\partial^2 E}{\partial \Omega^2}\right|_{\Omega=\Omega_0} . \tag{3.30}$$

With respect to our bulk material, it is known that both GaAs and AlAs at zero pressure have a cubic structure, based on tetrahedral units. Phase diagrams under pressure have been studied both experimentally and theoretically [71, 72, 73, 74, 75, 76, 77]. We have therefore imposed the zinc-blend structure and minimized the total energy as a function of the primitive cell volume Ω. Starting from the curves of the total energy $E(\Omega)$ and the pressure $P(\Omega)$ due to internal hydrostatic stress at a non-equilibrium volume, the cohesion energy and the bulk modulus can be easily determined, interpolating the values $E(\Omega)$ or $P(\Omega)$ with suitable equations of state. There are many choices for the interpolating curves. Close to the minimum the curve is a parabola, but the points deviate rapidly from the quadratic law and, at a large distance from a_0, it is necessary to fit the points to something more sophisticated. One of the most popular fitting curves is the Murnaghan equation [78], which depends on three parameters: Ω_0, B_0, B_0' (the derivative of the bulk modulus with respect to pressure):

$$E(\Omega) = \frac{\Omega_0 B_0}{B_0'}\left[\frac{1}{B_0'-1}\left(\frac{\Omega_0}{\Omega}\right)^{B_0'-1} + \frac{\Omega}{\Omega_0}\right] + \text{const}\,. \tag{3.31}$$

Often, it is preferred to adjust the pressure P, via the Birch-Murnaghan [79] equation of state:

$$P = \frac{3}{2}B_0\left(\left(\frac{\Omega}{\Omega_0}\right)^{-7/3} - \left(\frac{\Omega}{\Omega_0}\right)^{-5/3}\right)\left[1 + \frac{3}{4}\left(B_0'-4\right)\left(\left(\frac{\Omega}{\Omega_0}\right)^{-2/3} - 1\right)\right] . \tag{3.32}$$

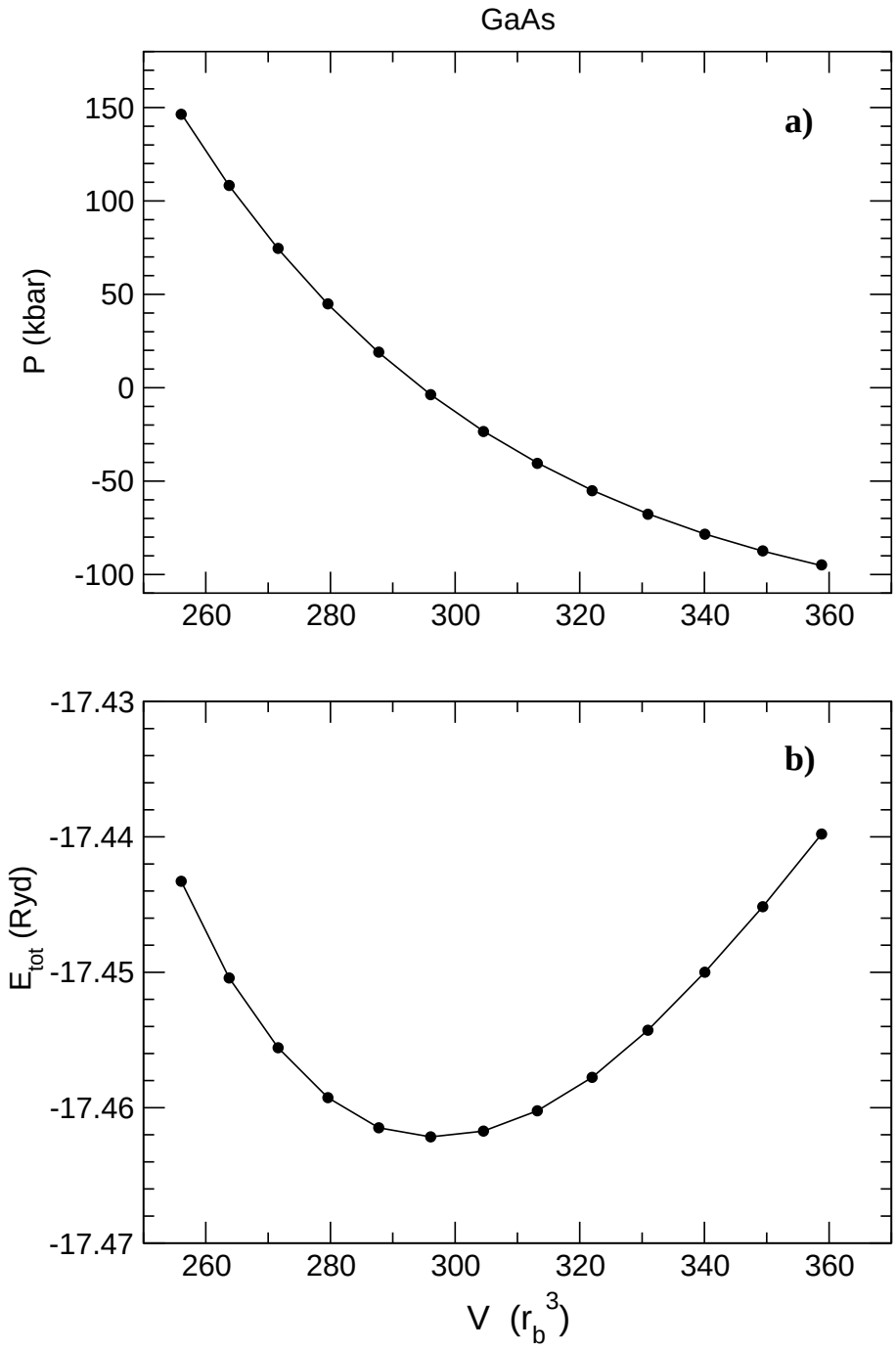

Figure 3.1: Pressure (a) and total energy (b) of GaAs for different values of the primitive cell volume. The numerical values (circles) are interpolated, respectively, with a Birch-Murnaghan equation and a Murnaghan equation (continuous lines). Both the curves (a) and (b) correspond to a cutoff of 25 Ry.

An example of interpolation is illustrate in Fig. 3.1. In Table 3.1 we summarize the obtained fitting parameters, in comparison with experimental measurements and analogous results found in literature. When the interpolating function is specified in the articles, the values in literature has to be compared with quantities we have obtained by the same equations of state.

We have shown these results, because a comparison with similar *ab initio* calculations and experimental values is extremely important to evaluate the reliability of the norm-conserving pseudopotential that we have generated. Some tests that can be executed directly on the atom, to assess the quality of the pseudopotentials, are discussed in Appendix B. Nevertheless, after executing the atomic tests, a final validation is still needed: the calculation of the structural properties for an infinite bulk crystal is, certainly, a proving test. An agreement within 1%-3% with the experiment for the lattice constant and an agreement within 5%-10% for the bulk modulus indicate that the calculations are reliable. In our case the agreement is even better. In LDA the errors on the lattice constants are systematic: all the bond strengths are overestimated [81], thus calculated lattice constants are too small.
At last, before applying calculations to superlattice systems, we have reproduced the ground state calculations of the bulk GaAs, choosing to describe the cubic structure in terms of simple tetragonal supercells, like $(GaAs)_2$, $(GaAs)_4$, $(GaAs)_6$, by lowering the symmetry of the fcc cubic point group. It is obvious that two different views of the same problem must lead to the same results. Thus, the test is intended to verify that the passage from the cubic symmetry of the bulk to the tetragonal symmetry of the superlattice does not introduce an additional font of numerical error in calculations. This occurrence has been excluded, by checking the convergence of the **k**-points set, assuring that the difference in the total energy between the fcc and the tetragonal description is less than 1 meV.

3.4 Kohn-Sham eigenstates and quasi-particle states

We are now leaving the study of structural properties to focus on the transitions to excited states. When dealing with an interacting particle system, the easier one-particle description can be retained at the price to introduce the concept of

Table 3.1: Structural parameters at zero pressure for the zinc-blend structure of GaAs and AlAs: equilibrium cell volume Ω_0 (in r_b^3), bulk modulus B_0 (in kbar), and pressure derivative of the bulk modulus B_0' (dimensionless). Our results are compared with experimental measurements and analogous *ab initio* calculations.

	GaAs	AlAs
Ω_0 (r_b^3)		
Present work	297.0[a]	298.9[a]
	294.6[b]	297.2[b]
Expt.	305.12[e]	306.3[b,g]
	304.89[f]	
Other theoretical works	298.1 [c,e]	300.7[c,e]
	297.0 [a,f]	308.8[a,f]
B_0 (kbar)		
Present work	731[a]	743[a]
	757[b]	765[b]
Expt.	754[b,d]	740 ± 40[b,g]
Other theoretical works	740[c,e]	750[c,e]
	708[a,f]	710[a,f]
B_0'		
Present work	4.8[a]	4.3[a]
	4.6[b]	4.2[b]
Expt.	4.5[b,d]	5.0 ± 1[b,g]
Other theoretical works	4.6[c,e]	4.3[c,e]
	3.36[a,f]	3.3[a.f]

[a] Murnaghan equation of state

[b] Birch-Murnaghan equation of state

[c] Chebyshev polynomial fit

[d] Reference [72]

[e] Reference [77]

[f] Reference [71]

[g] Reference [75]

quasi-particle (QP) states. A quasi-electron differs from a bare electron because it moves dressed by the interaction with a cloud of surrounding electrons. The screening change its effective mass and makes finite its lifetime. The quasi-particle energies are given by the energies needed to add/subtract an electron to/from the system. These quasi-particle levels can be measured respectively in inverse-photoemission or photoemission spectroscopy and can be calculated within a coherent many-body theory framework. The many-body problem can be approached thanks to the Green function formalism. We will not discuss this subject in this work. For further information about many-particle physics we suggest to read Ref. [82], and in particular for solid state applications Ref. [83]

The one-electron band structure is given by the dispersion of the energy level n, as a function of the wave-vector $\mathbf{k}$, which varies along the high symmetry directions inside the first Brillouin zone. The excited states are not a priori accessible through static ground state DFT: the eigenstates $\phi_{n,\mathbf{k}}$ and the energies $\epsilon_{n,\mathbf{k}}$, solutions of the KS equations, are not the "true" levels, i.e. the quasi-particle energies, of the electron in the solid. Only the highest occupied DFT-KS eigenvalue $\epsilon^{(N)}_{N,DFT}$ of an N-electron system, if obtained with the exact xc potential, equals the true ionization potential [80, 84], which in case of infinite systems is the chemical potential μ. Though a many-body calculation is the only means to calculate a completely reliable band structure, it is quite common to interpret the solutions of the KS equations to be electronic energies, and the results are sometimes a reasonably good representation of the energy levels, in particular concerning band dispersions. A justification can be found in the correct many-body approach. In fact, the Green-function theory yields a Schrödinger-like equation for the quasi-particles, which is extremely similar to the KS equation. The two equations differ for the substitution of the xc potential for a non-local and energy-dependent operator, called self-energy. One can then consider the KS equations as an approximation of the quasi-particle equations, where the self-energy operator $\Sigma\left(\mathbf{r}, \mathbf{r}', \epsilon^{QP}_{n,\mathbf{k}}\right)$ is approximated by the simpler local xc potential $V_{xc}(\mathbf{r})$. The KS orbitals $\phi_{n,\mathbf{k}}$ are thus usually considered a zero-order approximation of the wavefunctions of the interacting system. Hybertsen and Louie [85] have shown that this approximation has a very high precision for bulk states: $\left|\langle\phi^{QP}_{n,\mathbf{k}}|\phi^{LDA}_{n,\mathbf{k}}\rangle\right|^2 \simeq 0.999$. This result, together with the good qualitative agreement

of the DFT-LDA occupied density of states with the quasi-particle calculations and the experiments, gives a valid motivation to interpret the KS eigenstates in terms of one-electron wavefunctions and energies for the electron in the solid. Nevertheless, it is well known that a DFT band structure calculation always leads to a strong underestimation of band gaps, often by more than 50% [85, 86, 87, 88, 89, 90, 91].

There has been an interesting dispute about the origin of this gap problem. The more accredited idea is now that this is an intrinsic limit of DFT-KS [92, 93] and does not derive from the LDA. It is possible to show that the real gap and the KS gap are connected by the relation:

$$\epsilon_{gap} = \epsilon_{gap}^{KS} + \Delta_{xc}\,, \tag{3.33}$$

where the calculated DFT-LDA gap,

$$\epsilon_{gap}^{KS} = \epsilon_{N+1,DFT}^{(N)} - \epsilon_{N,DFT}^{(N)}\,, \tag{3.34}$$

is the difference between the energies of the lower empty state and the higher occupied state of the N-electron system and

$$\Delta_{xc} = V_{xc}^{(N+1)}\left(\mathbf{r}\right) - V_{xc}^{(N)}\left(\mathbf{r}\right)\,. \tag{3.35}$$

In fact, the discontinuity of order one experienced when an electron is added can only be due to the exchange-correlation term, which is not necessarily analytical in the number of electrons N, while the Hartree and the external potential are analytical. It could be thought that Δ_{xc} is small and that the LDA is the main cause of the band gap error. This does not seem to be the case, at least not for all the systems [59]: a rigorous model for monodimensional semiconductors [94] shows that Δ_{xc} is a significant fraction of the energy gap. Concerning real solids, in particular Si, GaAs and AlAs, there is evidence that the discontinuity is responsible for about 80% of the total error [87, 92, 95]. It is clear that the only satisfying solution of the gap problem goes through the many-body theory and the precise definition of the energy gap as the difference in the chemical potentials of an $(N+1)$-electron system and an N-electron system:

$$E_{gap} = E_{tot}^{(N+1)} - E_{tot}^{(N)} - \left(E_{tot}^{(N)} - E_{tot}^{(N-1)}\right)\,. \tag{3.36}$$

The many-body calculations are finally in good agreement with the experiments, but they have the disadvantage to require a very high computational effort. Quasi-particle calculations are usually carried out within the GW approximation [96]: for this reason the differences between DFT eigenvalues and quasi-particle energies are called GW corrections. In case of GaAs, AlAs, and some other simple materials, it has been observed that the GW corrections shift the conduction bands almost rigidly upwards [1] [86]. This result justify the "scissor operator" approximation, which consists in obtaining the quasi-particle band structure within an error of 0.1-0.2 eV in all the Brillouin zone, simply by adding a constant value to all the conduction band levels. It is worth reminding that this approximation is not valid for all kinds of materials. Some authors have applied the scissor operator to GaAs/AlAs superlattices [21], considering that the energy shift for the two bulk material is almost the same. We will get deeper into this subject in the following section, while presenting the DFT-LDA band dispersions.

3.5 Bulk band structure by DFT-LDA calculations

We are finally ready to provide a more detailed analysis of the bulk band structure obtained by means of the DFT-LDA, with norm-conserving pseudopotentials and a plane wave basis set. The diagonalization of the KS equations for bulk GaAs and AlAs has been done at the theoretical lattice constants calculated in section 3.3. In Figs. 3.2 and 3.3 we show the band structures obtained by interpreting the Kohn-Sham eigenvalues to be electronic energies, without applying any scissor operator. As expected, this approximation always leads to a strong underestimation of band gaps, even more than 50% for GaAs, while the form of the bands and their width is correct. We know from literature (see Ref. [86]) that GW quasi-particle energies, on the other hand, reproduce correctly experimental gaps to within 0.1 - 0.2 eV. We can have an idea of the real band structure applying a scissor operator: in fact, it has been proved that the GW corrections shift the conduction bands almost rigidly in GaAs and AlAs [86]. Displacing the GaAs and AlAs DFT-LDA conduction bands upwards respectively by 0.8 and 0.9 eV yields an error in comparison to the GW

[1] Because of the LDA approximation, the valence band maximum is not exact and the actual effect of GW corrections involve as well a slight shift downwards of the valence bands.

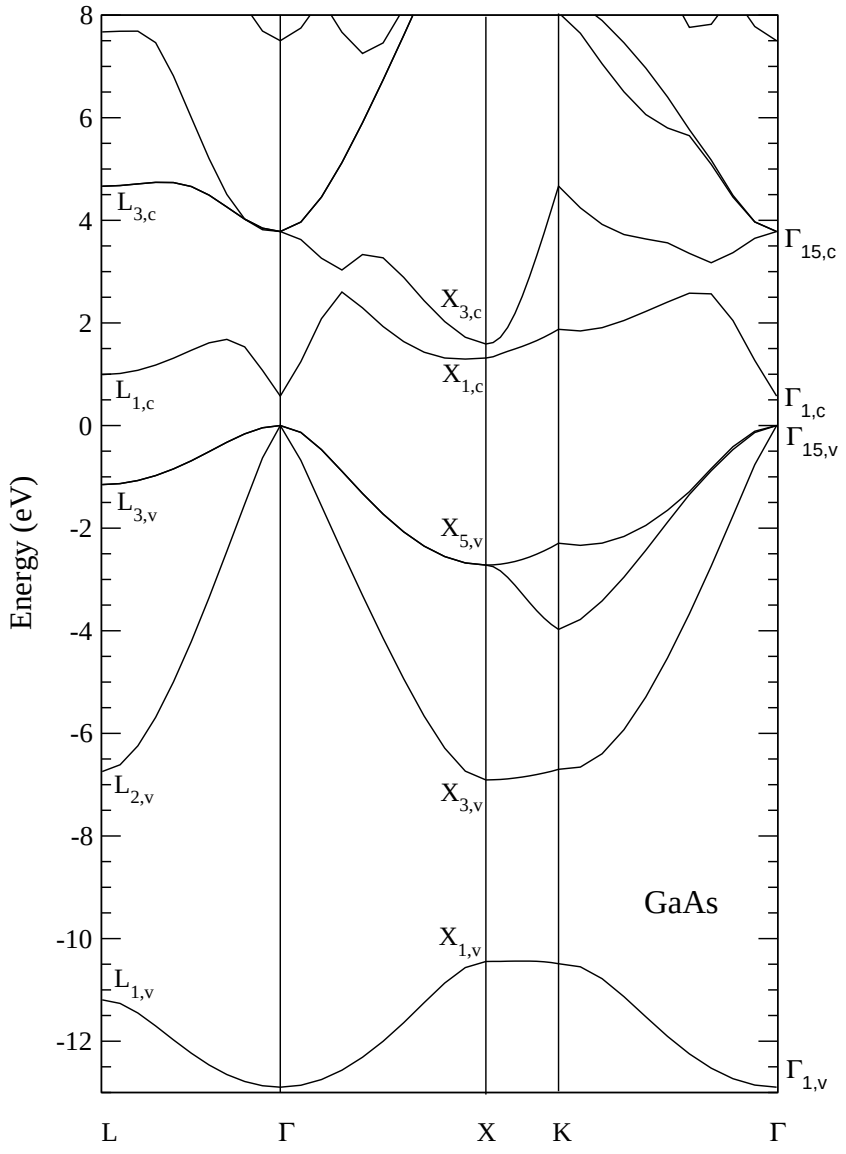

Figure 3.2: Kohn-Sham LDA scalar-relativistic band structure of GaAs for the valence bands and the lowest conduction bands. The energy zero is fixed at the valence band maximum.

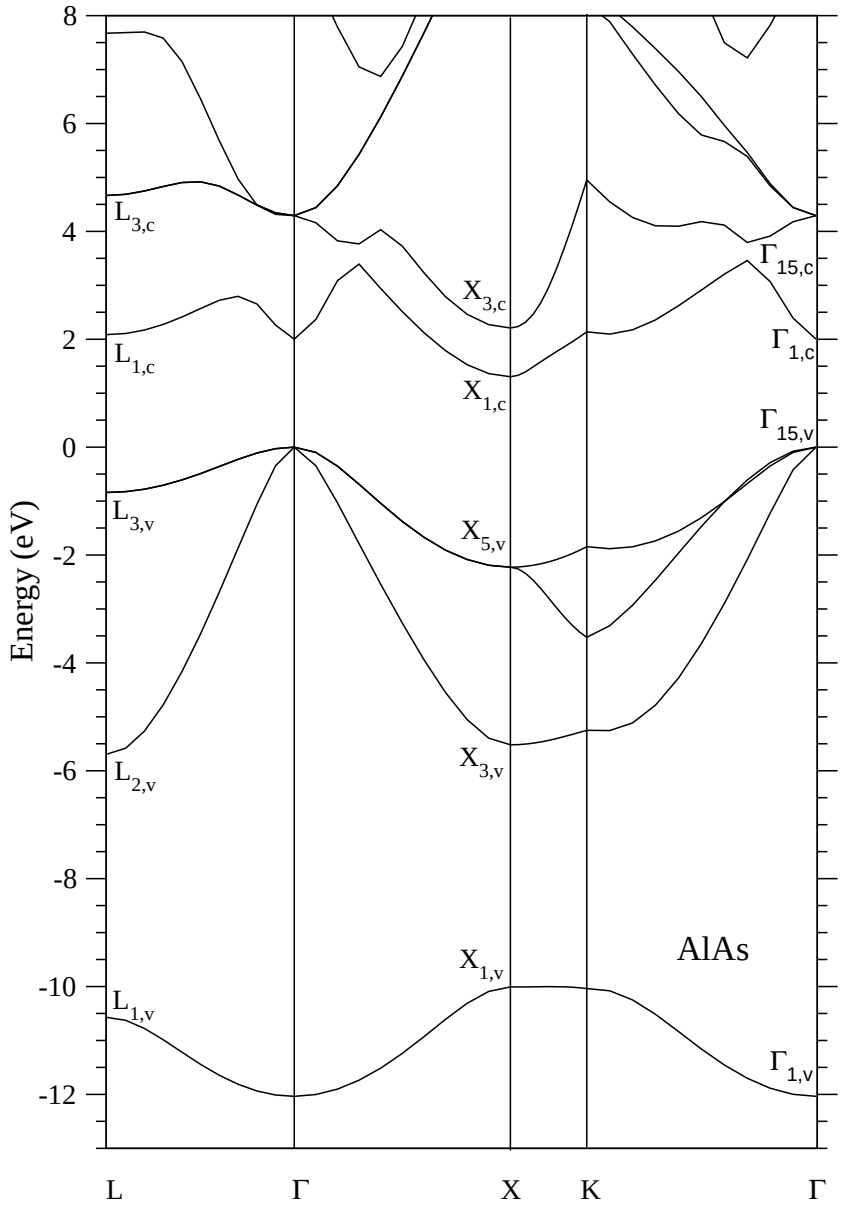

Figure 3.3: Kohn-Sham LDA scalar-relativistic band structure of AlAs for the valence bands and the lowest conduction bands. The energy zero is fixed at the valence band maximum.

results within 0.1 eV for the bands closest to the gap [86]. In Tables 3.2 and 3.3 we present the numerical values of the *ab initio* calculated (applying the scissor operator) energy levels at the high symmetry points together with the empirical results and experimental data. In the third column GW quasi-particle energies from Ref. [86] are reported, to better judge the efficacy of the scissor operator. The spin-orbit interaction is neglected in all the theoretical approaches considered here, whereas the measured energies present a spin-orbit splitting of the highest valence levels. We remark again that the KS-LDA eigenvalues are converged to within a few meV for both GaAs and AlAs crystals.

At last, we have compared our results with previous DFT-LDA calculations found in literature. We have found that a complete equivalence of the results is not possible, even within a DFT-LDA pseudopotential calculation, in a plane wave representation. In fact, considering that it is not known how exactly the different authors have built their norm-conserving pseudopotentials and sometimes it is not specified if they work at the experimental or theoretical lattice constant, it is not surprisingly to detect differences up to 0.25 eV. We find an overall excellent agreement to within less than 0.1 eV with calculations of Godby *et al.*, both for GaAs and AlAs, in Ref. [86]. Also the agreement with Bachelet *et al.* in Ref. [97] is satisfactory. As discussed in Ref. [86], the experimental values concerning AlAs conduction band edges, especially the value of the gap in L, are not obtained from direct measurements and are not completely reliable. Moreover, we have tried to calculate the band structure at the experimental lattice constant, showing that the behavior of the critical points under an hydrostatic pressure is both qualitatively and quantitatively the same as described by Fiorentini *et al.* in Ref. [98]. In fact, being the theoretical LDA lattice constants smaller than the experimental ones, executing calculations at the experimental values means applying a negative hydrostatic pressure to the crystal. We observe that the gap widths in Γ and L become smaller, both for GaAs and AlAs. The gap widths in X grow: this effect is stronger for the first gap X_1 in both materials and it is almost negligible for the second gap X_3 in AlAs.

Table 3.2: GaAs eigenvalues at some high symmetry points as obtained in the present work by the empirical pseudopotential method and the DFT-LDA *ab initio* theory. The DFT-LDA values are corrected by a scissor operator of 0.8 eV [86]. Our results are compared to GW quasi-particle energies [86] and experiments. The zero of energy is at the top of the valence band. The spin-orbit interaction term is omitted in all calculations and indicated in parenthesis for experiments.

Energy level	EPM	DFT-LDA	GW	Experiment
Γ_1^v	-12.11	-12.90		-13.10[b]
Γ_{15}^v	0.00	0.00	0.00	0.00 (-0.34)[a]
Γ_1^c	1.51	1.37	1.47	1.52[a]
Γ_{15}^c	4.01	4.58	4.52	4.72[b]
X_1^v	-10.00	-10.45		
X_3^v	-6.16	-6.91		
X_5^v	-2.31	-2.72	-2.73	-2.78 (-2.85)[a]
X_1^c	2.02	2.12	2.08	1.98[c] - 2.01[d]
X_3^c	2.39	2.39	2.30	2.38[e]
L_1^v	-10.64	-11.19		
L_2^v	-5.98	-6.74		
L_3^v	-0.96	-1.15	-1.11	-1.19 (-1.40)[a]
L_1^c	1.83	1.79	1.82	1.82[c] - 1.84[d]
L_3^c	4.84	5.46	5.41	

[a] Reference [99]

[b] Reference [100]

[c] Reference [101]

[d] Reference [102]

[e] Reference [103]

Table 3.3: AlAs eigenvalues at some high symmetry points as obtained in the present work by the empirical pseudopotential method and the DFT-LDA *ab initio* theory. The DFT-LDA values are corrected by a scissor operator of 0.9 eV [86]. Our results are compared to GW quasi-particle energies [86] and experiments. The valence band maxima are aligned. The spin-orbit interaction term is omitted in all the calculations and indicated in parenthesis for experiments.

Energy level	EPM	DFT-LDA	GW	Experiment
Γ_1^v	-11.67	-12.03		
Γ_{15}^v	0.00	0.00	0.00	0.00 (-0.28)[a]
Γ_1^c	3.03	2.90	3.26	3.11[c]
Γ_{15}^c	4.21	5.11	5.05	4.34[b]
X_1^v	-9.49	-10.01		
X_3^v	-5.62	-5.52		
X_5^v	-2.25	-2.23	-2.34	-2.30 (-2.45)[d]
X_1^c	2.22	2.21	2.09	2.24[a]
X_3^c	3.20	3.11	2.99	2.68[e]
L_1^v	-10.14	-10.57		
L_2^v	-5.59	-5.69		
L_3^v	-0.93	-0.84	-0.88	-1.31 (-1.51)[a]
L_1^c	2.87	2.99	3.03	2.49[c] - 2.54[d]
L_3^c	5.00	5.57	5.48	

[a] Reference [99]

[b] Reference [104]

[c] Reference [102]

[d] Reference [101]

[e] Reference [105]

3.6 Superlattice band structure by DFT-LDA calculations

Finally, we present *ab initio* calculations of (001) GaAs/AlAs superlattice band structures, obtained by means of the DFT-LDA, with norm-conserving pseudopotentials and a plane wave basis set. These calculations are formally analogous to the calculations for bulk systems presented in the previous section. The cubic T_d point group is replaced by the smaller tetragonal D_{2d} point group and each supercell contains p Ga atoms, p Al atoms and $2p$ As atoms (see Fig. 1.1 on page 11). The symmetry of the system is fully described: in particular, the As atoms at the interface do not entail any artificial asymmetry, because the As norm-conserving pseudopotential is independent of the environment (Ga or Al neighbors) where the As atoms are placed. We have studied (001) $(\mathrm{GaAs})_p/(\mathrm{AlAs})_p$ superlattices with a superlattice period p ranging from 1 to 8. The number of plane waves involved in the calculations grows as p, thus the computational expense becomes higher and higher at large superlattice periods (as a term of comparison, on a NEC SX-5 machine, to compute $10 \times 2p$ bands relative to p=1 the time needed is 2 minutes, whereas calculating the corresponding number of bands for p=8 requires a time more than 100 times longer).

The resolution of the KS equations for the almost lattice-matched heterostructures has been done at the averaged theoretical lattice constants. We do not need to perform a structural minimization to determine the relaxed geometry of the cell, since the lattice mismatch is small enough to make negligible stress and strain effects, which do not affect the band structure, as usually assumed in literature (see, e.g., [106, 107, 108, 109]). We have however verified that the total energy does not change significantly when moving from the GaAs lattice constant to the AlAs lattice constant. Moreover, the total energy is close to its minimum at this averaged value.

In Figs. 3.4 and 3.5 we present the two extreme examples of superlattice bands for p=1 and p=8: all the $4 \times 2p$ valence states and the conduction states up to 8 eV are shown in the tetragonal Brillouin zone. We remind that, since $2p$ **k**-points in the fcc Brillouin zone are always folded onto the same point **q** in the smaller tetragonal Brillouin zone, the number of occupied superlattice bands is $2p$ times the number of bulk bands for a GaAs/AlAs superlattice. The p=1 superlattice (see Fig. 3.4)

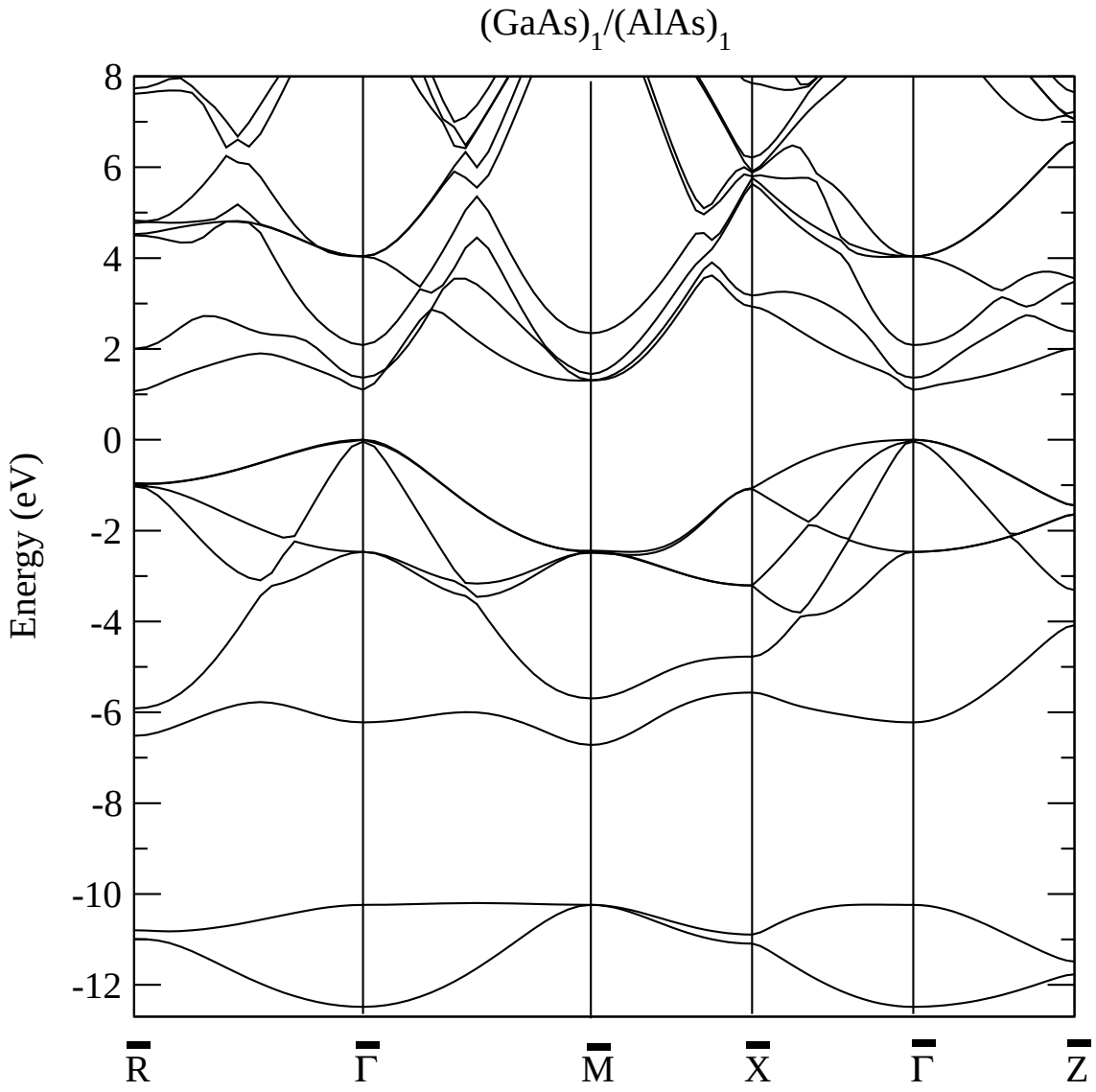

Figure 3.4: Kohn-Sham LDA scalar-relativistic band structure of a $(GaAs)_1/(AlAs)_1$ (001) superlattice along the high symmetry directions. The energy zero is taken at the valence band maximum.

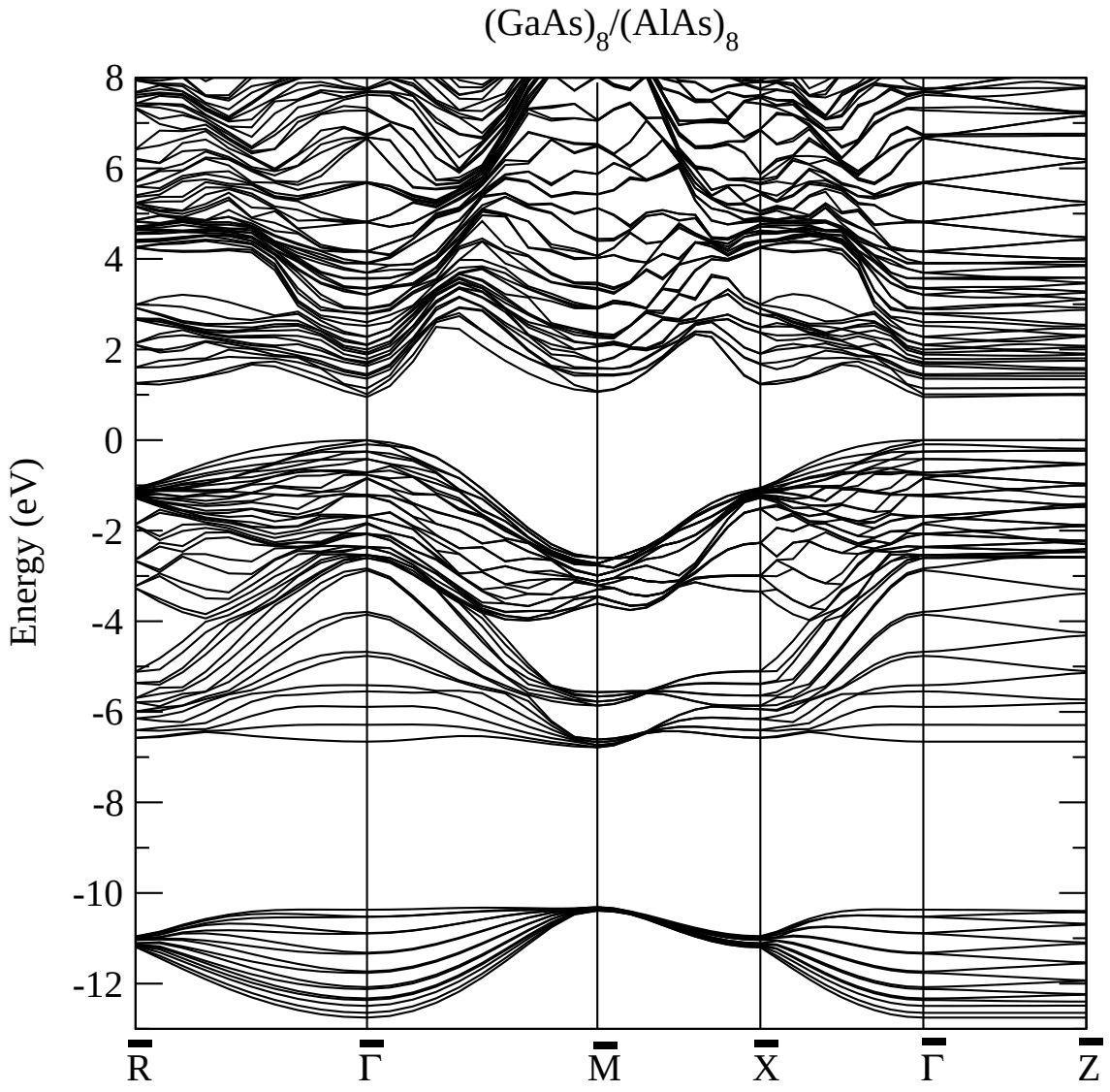

Figure 3.5: Kohn-Sham LDA scalar-relativistic band structure of a $(GaAs)_8/(AlAs)_8$ (001) superlattice along the high symmetry directions. The energy zero is taken at the valence band maximum.

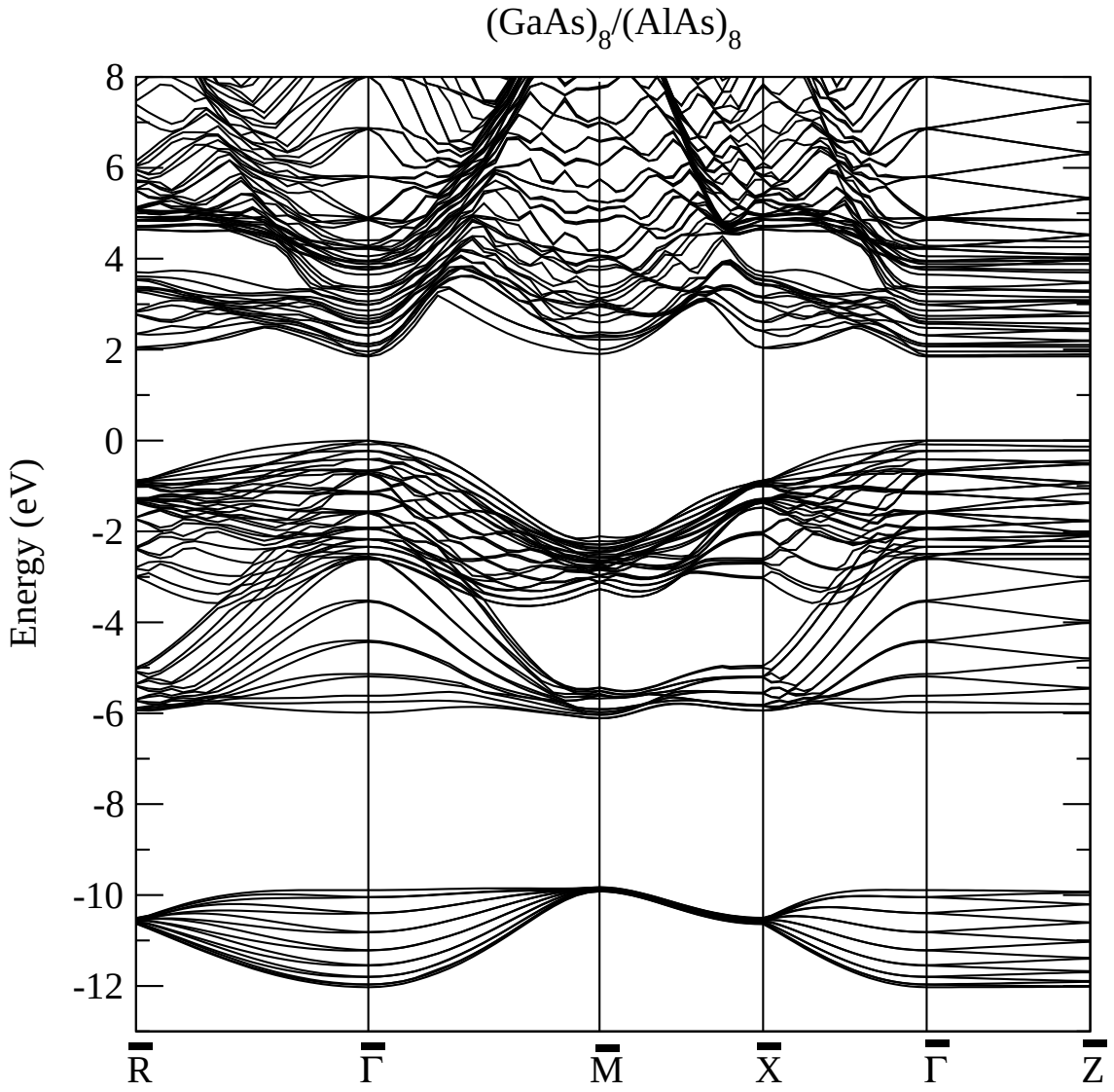

Figure 3.6: Semi-empirical LCBB band structure of a $(GaAs)_8/(AlAs)_8$ (001) superlattice along the high symmetry directions. The energy zero is taken at the valence band maximum.

is the more instructive one, because the number of bands is only doubled and the figure is more readable and easy to compare to the band structure in Fig. 3.2. This case was not studied within the semi-empirical framework, because a description in terms of bulk states is not reliable for very short period superlattices. The p=1 Brillouin zone can be obtained by folding once the bulk zone. Hence, the point $\bar{\Gamma}$ corresponds to both points Γ and X_z, the point $\bar{M}$ corresponds to both points X_y and X_x, and point $\bar{R}$ corresponds to both points L_z and L_{-z} of the corresponding bulk Brillouin zone. The lowering in the crystal symmetry is responsible for the removal of level degeneracies at the high symmetry points. The spin orbit splitting is not included. The direct LDA band gap measures 1.1 eV: it is almost twice larger than the bulk GaAs gap, pointing to strong confinement effects. The $\bar{R}_{1c}$ state is the conduction band minimum, in agreement with the DFT-LDA and quasi-particle results reported in Refs. [44, 21]. Following the suggestion in Ref. [21], we have applied a scissor operator of 0.92 eV to calculated conduction band energies and compared our energies at the high symmetry points with analogous DFT-LDA results, available only for p=1,2,3, by Dandrea *et al.* [21]. The differences never exceed 0.1 eV. The good agreement of short-period results suggests that also the results for larger periods are reliable. To improve these results, quasi-particle corrections and/or all electron and/or full relativistic (including spin-orbit interaction) calculations would be needed.

Finally, the Fig. 3.6 shows the band structure of the $(GaAs)_8/(AlAs)_8$ superlattice, as calculated by the semi-empirical LCBB method adopted in the previous chapter. The Figs. 3.6 and 3.5 are here presented on the same scale, to allow an easy comparison of the two band dispersions. As expected, the gap is better reproduced by the semi-empirical calculations. Except for that, the band dispersions and widths are surprisingly similar, both in valence and in conduction bands.

In conclusions, in this chapter we have presented DFT-LDA calculations for bulk GaAs, bulk AlAs and GaAs/AlAs superlattices. By calculating the ground states properties of the bulk materials, we have proved the reliability of the norm-conserving pseudopotentials we have constructed. The results for bulk LDA energy levels, after the application of a suitable scissor operator, have been compared with corresponding results, which we have obtained in the semi-empirical LCBB approach, and with

experimental and theoretical data found in literature. The ab initio GaAs/AlAs band structure is compared to the corresponding semi-empirical band structure and to some data available in literature for short-period superlattices. We have found an overall agreement of all the different results, which confirms the analysis developed in Chapter 1 and attests without doubts the high quality of the electronic states, both semi-empirical and DFT-LDA, which will be the basis of the optical absorption calculations in the following chapters.

Chapter 4

Semi-empirical calculations of optical properties

In a spectroscopic experiment the sample is excited from its ground state: the response to the perturbation is the object of both experimental measurements and theoretical calculations. A big variety of phenomena can occur. In Fig. 4.1 we show three model excitations: direct photoemission, inverse photoemission, and absorption. Direct/inverse photoemission processes are one-quasi-particle excitations: a quantum of energy $h\nu$ is absorbed/emitted while an electron is ejected/absorbed. The ejected/incoming electron is supposed to be completely decoupled from the system after/before the process takes place. These kinds of experiments give insight, respectively, on the density of occupied and unoccupied states. Here we are more interested in absorption processes in solids. In a naive picture, the incoming radiation causes the transition of an electron from an occupied state in the valence band to an empty state in the conduction band. However, even if one uses quasi-particle instead of one-electron states, one faces the problem that this process is not the simple combination of an inverse photoemission and a direct photoemission process, because the electron does not leave the sample and continues interacting with it. The electron which has undergone a transition to the conduction band and the relative hole left in valence band feel each other via a Coulomb interaction: this is the so-called excitonic effect, which introduces the main complexity in computations, since it forces to abandon the independent quasi-particle picture, to move to

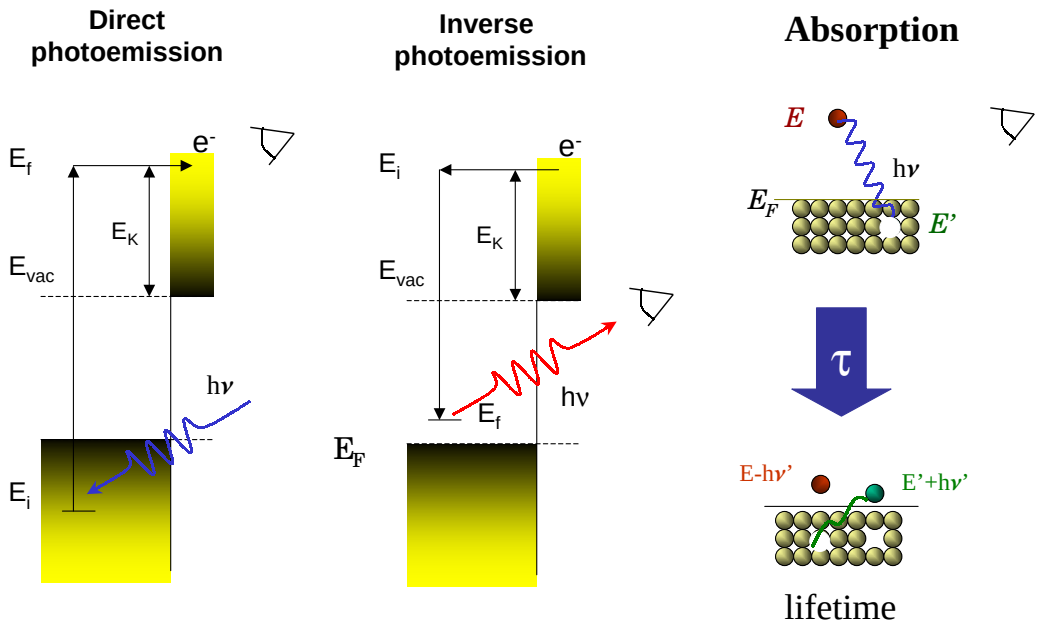

Figure 4.1: Schematic representation of the excitations involved in photoemission, inverse photoemission, and absorption.

a two-particle excitation picture.

Nevertheless, in the study of the optical properties, independent particle schemes maintain their usefulness, and are preliminary to full many-body treatments. The most used approach is the semi-classical theory of interband transitions [9, 110]. In this chapter, we will discuss how to combine it with semi-empirical band structure calculations, to gain information about the absorption spectra of semiconductor superlattices. This simple formalism allows to reproduce all the features present in an absorption spectrum which are connected to one-quasi-particle excitations. Moreover, it allows to describe the absorption process in terms of the intuitive concepts of *joint density* of occupied and unoccupied states and of transition probabilities from occupied to unoccupied states.

As we have already discussed in Section 3.4, strictly speaking, electrons in a solid are never independent particles. In spite of this, the one-particle picture can be retained at the price to renormalize the single electron energy levels by the presence of the surrounding electrons, defining the concept of quasi-particles. This is sufficient only for situations where the electron-hole interaction is not important. The quasi-particles are still described by a one-particle Schrödinger-like equation, where the effective potential has to include the effects due to the electron-electron interaction. In case of empirical/semi-empirical band structure calculations, these renormalizations are at least partially included – to what extent it depends by the complexity of the model – thanks to the parameterization of the Hamiltonian, which is directly fitted to reproduce the experimental spectra. On the other hand, excitonic effects lead inevitably to the need of a two-particle description of the system. Within an empirical/semi-empirical approach, they can be qualitatively included thanks to an effective mass approximation [111, 112]. Together with the so-called local field effects, excitonic effects give essential contributions to estimate the height of the peaks in absorption spectra. In empirical/semi-empirical calculations, however, the peak positions can be already in good agreement with experiments (within a few tenth of eV) without the inclusion of these corrections. In fact, the empirical parameters can be expressly fitted to reproduce the correct peak positions. Being mainly interested in determining the peak positions and their evolution as a function of the well/barrier width, we have decided, at this stage, to neglect both the

contributions of excitons and local fields. We will discuss at the end of the chapter the limits of this approximation.

One further point of interest is the birefringence. The calculations presented here yield only the contribution to the birefringence arising from quantum-confinement-induced modifications of the electronic states; they do not account for the intrinsic dielectric anisotropy of a multilayer, arising from different boundary conditions for an electric field parallel or perpendicular to the layers [113, 114]. This second contribution to the birefringence is in fact equivalent to the inclusion of local-field effects in the dielectric response [115, 116, 117, 118].

In the following section we will organize the results obtained, discussing the optical properties of GaAs/AlAs and GaAs/vacuum superlattice systems, via the calculated real and the imaginary parts of the components of their macroscopic dielectric tensor. We have written a computational code, which adopts the LCBB technique, as presented in Chapter 2, to perform the calculations of the optical spectra. We will explain why the method succeeds in reproducing the experimental behavior of the peak positions under confinement, whereas it fails to describe the low-frequency optical birefringence of the GaAs/AlAs systems and, in particular, its behavior as a function of the number of monolayers p.

4.1 Semi-classical theory of interband transitions

The macroscopic dielectric properties of a solid are intimately connected with its band structure: we want to discuss how the optical spectra can be reproduced, already to a satisfactory extent even if at a first level of approximation, starting from the simple knowledge of the one-electron band structure. The discussion which follows is valid for isotropic materials, like bulk zinc-blend crystals, where a simple scalar dielectric function (more precisely its real and imaginary parts) is all we need to determine the optical response of the medium. In case of anisotropic crystals, like superlattices, it is necessary to define a dielectric tensor: the expressions we will get for the dielectric functions are easily adaptable for the single components of the dielectric tensor. We will deal with an electromagnetic field, which is supposed weak, acting as a perturbation. The wavelength of the incoming radiation is long in

comparison to the lattice constant and we suppose, at the moment, that the medium can be considered homogeneous. The theory is called semi-classical because, while the Bloch electrons are described as a quantum system, the radiation is treated as a classical field. The core ions are kept "frozen" in their lattice sites, thus excluding the occurrence of phonon-assisted electronic transitions. Undoubtedly, phonons are responsible for broadening spectral features: these lifetime effects can be approximately taken into account by a small imaginary constant added to the absorption energy.

The complete Hamiltonian, which describes an electron in a solid in presence of the electromagnetic field, is:

$$H = \frac{1}{2}\left(\mathbf{v} - \frac{\mathbf{A}(\mathbf{r},t)}{c}\right)^2 + V^{PP} - \Phi(\mathbf{r},t)\,, \tag{4.1}$$

where A is the vector potential and Φ the scalar potential of the radiation field. In the Coulomb gauge ($\nabla \cdot \mathbf{A} = 0$, $\Phi = 0$), neglecting non-linear effects, the electron-radiation interaction term reads:

$$H^{loc}_{e-rad} = -\frac{1}{c}\mathbf{A}(\mathbf{r},t)\cdot\mathbf{p}\,. \tag{4.2}$$

The relation (4.2) is correct only if the potential is local (the semi-empirical pseudopotential is local), otherwise we need to take into account the non-vanishing commutator of the non-local term with the coordinate operator:

$$H^{non-loc}_{e-rad} = -\frac{1}{c}\left(\mathbf{p}\cdot\mathbf{A}(\mathbf{r},t) + i\left[V_{nl},\mathbf{r}\right]\cdot\mathbf{A}(\mathbf{r},t)\right)\,. \tag{4.3}$$

For an incoming plane wave characterized by a frequency ω, the vector potential $\mathbf{A}$ has the form:

$$\mathbf{A}(\mathbf{r},t) = A_0\,\mathbf{e}\,e^{i(\mathbf{q}\cdot\mathbf{r}-\omega t)} + c.c.\,, \tag{4.4}$$

where $\mathbf{e}$ is the polarization unitary vector and c.c. indicates the complex conjugate of the precedent term. The first term in (4.4) is responsible for absorption, the second for stimulated emission.

Following Bassani and Pastori Parravicini [110], the probability per unit time and unit volume that a perturbation of the form $\mathcal{H}\,e^{\pm i\omega t}$ induces a transition from an initial state $|i\rangle$ to a final state $|f\rangle$ is given by the Fermi's golden rule:

$$\mathcal{W}_{i\to f}(\omega) = 2\pi\left|\langle f|\mathcal{H}|i\rangle\right|^2\delta\left(\omega_f - \omega_i \mp \omega\right)\,, \tag{4.5}$$

conductivity	$\sigma = \sigma_1 + i\sigma_2$
dielectric function	$\epsilon = \epsilon_1 + i\epsilon_2 \qquad \epsilon = 1 + (4\pi i\sigma)\,/\,(\omega)$
complex refractive index	$N = n + ik \qquad \epsilon = N^2 \qquad ; \epsilon_1 = n^2 - k^2\ ,\ \epsilon_2 = 2nk$
absorption coefficient	$\alpha = (2k\omega)\,/\,(c) = (\omega\epsilon_2)\,/\,(nc)$
reflectivity at normal incidence	$R = [(n-1)^2 + k^2]/[(n+1)^2 + k^2]$

Table 4.1: Relationships between optical response functions [119].

where the sign $-$ refers to absorption and the sign $+$ to emission of a quantum ω. The absorption and emission rates are the starting points to calculate whatever optical function, which describes the response of the system to an incoming radiation. Once a complex response function is known, all the others are related to it by means of the relations summarized in Table 4.1. Moreover, the real part and the imaginary part of a complex dielectric function are related by a Kramers-Kronig transformation [119].

Inserting Eqs. (4.2) and (4.4) in the matrix element of Eq. (4.5), in case of absorption, we find:

$$\langle c, \mathbf{k}'|\, \mathcal{H}\, |v, \mathbf{k}\rangle = \frac{A_0}{c}\, \langle \psi_{c\,\mathbf{k}'}|\, e^{i\mathbf{q}\cdot\mathbf{r}}\, \mathbf{e}\cdot\mathbf{p}\, |\psi_{v\,\mathbf{k}}\rangle = \frac{A_0}{c}\, \mathbf{e}\cdot\mathbf{M}_{cv}\,, \tag{4.6}$$

where the spatial integral, which describes the transition probability, is

$$\mathbf{e}\cdot\mathbf{M}_{cv} = \sum_s \int_\Omega d\mathbf{r}\, e^{-i(\mathbf{k}'-\mathbf{q})\cdot\mathbf{r}}\, u^*_{c\,\mathbf{k}'}(\mathbf{r}, s)\, \mathbf{e}\cdot(-i\nabla)\, e^{i\mathbf{k}\cdot\mathbf{r}}\, u_{v\,\mathbf{k}}(\mathbf{r}, s)\,. \tag{4.7}$$

When neglecting the spin-orbit interaction term, the Hamiltonian operator (4.1) is independent of spin, hence spin states are conserved in the transitions induced by the electromagnetic radiation. Adding a factor 2 in Eq. (4.7), we can account for the the spin degeneracies and be free to eliminate the dependence on spin coordinates in

the matrix element (4.7). The translational invariance of the wavefunction periodic parts $u^*_{c\mathbf{k}'}(\mathbf{r}, s)$ and $u^*_{v\mathbf{k}}(\mathbf{r}, s)$ imposes that, under the hypothesis of long wavelength λ ($\mathbf{q} = \mathbf{q}_{rad} \simeq 0$), only direct transitions, i.e. between valence and conduction states labelled by the same $\mathbf{k}$ vector, are permitted. This selection rule represents the respect of the momentum conservation in a periodic medium, whereas the energy conservation is expressed by the presence of the delta function in Eq. (4.5). To obtain the absorption probability per unit time and per unit volume, it is necessary to sum over all the possible initial and final states $|n, \mathbf{k}\rangle$, remembering that the level occupancy is described by the Fermi function $f_{n,\mathbf{k}}$. We obtain:

$$\mathcal{W}_{abs}(\omega) = 4\pi \left(\frac{A_0}{c}\right)^2 \sum_{v,c} \sum_{\mathbf{k}\in BZ} f_{v\mathbf{k}} \left(1 - f_{c\mathbf{k}}\right) \left| \mathbf{e} \cdot \mathbf{M}_{cv} \right|^2 \delta\Big(\omega_c(\mathbf{k}) - \omega_v(\mathbf{k}) - \omega\Big) . \quad (4.8)$$

In a completely analogous way we can get the emission probability per unit time and unit volume:

$$\mathcal{W}_{em}(\omega) = 4\pi \left(\frac{A_0}{c}\right)^2 \sum_{v,c} \sum_{\mathbf{k}\in BZ} f_{c\mathbf{k}} \left(1 - f_{v\mathbf{k}}\right) \left| \mathbf{e} \cdot \mathbf{M}_{vc} \right|^2 \delta\Big(\omega_c(\mathbf{k}) - \omega_v(\mathbf{k}) + \omega\Big) . \quad (4.9)$$

The absorption coefficient is defined as the coefficient α in the relation

$$I = I_0 e^{-\alpha d} , \quad (4.10)$$

which describes the intensity I of the radiation propagating in the medium at a distance d from the surface: the intensity decreases from the incoming value I_0 on the surface, following an exponential law. The determination of the absorption spectra requires the knowledge of the absorption coefficient, or equivalently, the imaginary part of the dielectric function $\epsilon = \epsilon_1 + i\epsilon_2$:

$$\alpha = \frac{\omega}{nc} \epsilon_2 . \quad (4.11)$$

Here n is the real part of the refractive index. We can obtain α dividing the difference between the absorbed and the emitted energy per unit time and per unit volume by the incident radiation flux:

$$\alpha(\omega) = \frac{(\mathcal{W}_{abs} - \mathcal{W}_{em})\, \omega}{n\, A_0^2\, \omega^2 / \, 2\pi\, c} . \quad (4.12)$$

The following equality is verified:

$$|\mathbf{e} \cdot \mathbf{M_{cv}}(\mathbf{k})|^2 = |\mathbf{e} \cdot \mathbf{M_{vc}}(\mathbf{k})|^2 ; \quad (4.13)$$

it is the quantum formulation of the detailed balance principle. Thus, the final result for the imaginary part of the dielectric function is:

$$\epsilon_2(\omega) = 2\frac{4\pi^2}{\omega^2}\sum_{c,v}\int_{BZ}\frac{d\mathbf{k}}{8\pi^3}\left(f_{v,\mathbf{k}} - f_{c,\mathbf{k}}\right)\left|\mathbf{e}\cdot\mathbf{M_{cv}}(\mathbf{k})\right|^2\delta\left(\omega_c(\mathbf{k}) - \omega_v(\mathbf{k}) - \omega\right) . \quad (4.14)$$

It is usually preferred to calculate ϵ_2 rather than α, because it does not depend on the index of refraction n, which is a function of the energy ω as well. By exploiting the Kramers-Kronig transformation, the expression of the real part of ϵ can be immediately derived from the knowledge of the imaginary part over all the frequency range (4.14):

$$\epsilon_1(\omega) = 1 + \frac{2}{\pi}\mathcal{P}\int_0^\infty \frac{\omega'\,\epsilon_2(\omega')}{\omega'^2 - \omega^2}\,d\omega' . \quad (4.15)$$

The transition rate depends on the factor $\left|\mathbf{e}\cdot\mathbf{M_{cv}}(\mathbf{k})\right|^2$. Close to a critical point, if the transition is not forbidden, this factor is different from zero and does not vary significantly with $\mathbf{k}$, so that we can extract it from the integral in (4.14), giving:

$$\epsilon_2(\omega) = \frac{4\pi^2}{\omega^2}\sum_{c,v}\left|\mathbf{e}\cdot\mathbf{M_{cv}}(\mathbf{k})\right|^2 J_{cv}(\omega)A_{cv}(\omega) , \quad (4.16)$$

where

$$A_{cv}(\omega) = f_{v,\mathbf{k}} - f_{c,\mathbf{k}} \quad (4.17)$$

is the band filling factor and

$$J_{cv}(\omega) = \int_{BZ}\frac{d\mathbf{k}}{4\pi^3}\delta\left(\omega_c(\mathbf{k}) - \omega_v(\mathbf{k}) - \omega\right) = \frac{1}{4\pi^3}\int_S \frac{dS}{\left|\nabla_{\mathbf{k}}\left(\omega_c(\mathbf{k}) - \omega_v(\mathbf{k})\right)\right|_{\omega_c-\omega_v=\omega}} \quad (4.18)$$

is the joint density of states (JDOS) for interband transitions. The JDOS shows strong variations in the neighborhood of the values of ω which satisfy the relation:

$$\nabla_{\mathbf{k}}\omega_c(\mathbf{k}) = \nabla_{\mathbf{k}}\omega_v(\mathbf{k}) . \quad (4.19)$$

The requirement (4.19) defines the critical points in the Brillouin zone and is usually satisfied in the high symmetry points or along the symmetry lines. Close to an extreme $\mathbf{k}_0$ of the band dispersion, the energy difference in the denominator of Eq. (4.18) can be developed in a series of $(\mathbf{k} - \mathbf{k}_0)$, up to the quadratic term in the expansion. Thanks to this simple analytical procedure, it is possible to deduce the form of the absorption curves close to the direct gap ω_g, in 1, 2 and 3 dimensions:

$$3D: \qquad J_{cv}(\omega) \;=\; \frac{1}{2\pi^2}\left(2m^*\right)^{3/2}\left(\omega - \omega_g\right)^{1/2}\theta\left(\omega - \omega_g\right) , \quad (4.20)$$

$$2D: \qquad J_{cv}(\omega) = \frac{m^*}{\pi}\theta\left(\omega-\omega_g\right), \tag{4.21}$$

$$1D: \qquad J_{cv}(\omega) = \frac{1}{\pi}\left(\frac{m^*}{2}\right)^{1/2}\left(\omega-\omega_g\right)^{-1/2}\theta\left(\omega-\omega_g\right). \tag{4.22}$$

With m^* we indicate the effective mass and θ is a step function. At zero dimension, the JDOS is obviously equal to a delta function. In Fig. 4.2 we illustrate the behavior of the JDOS in different semiconductor nanostructures. We will work at a zero

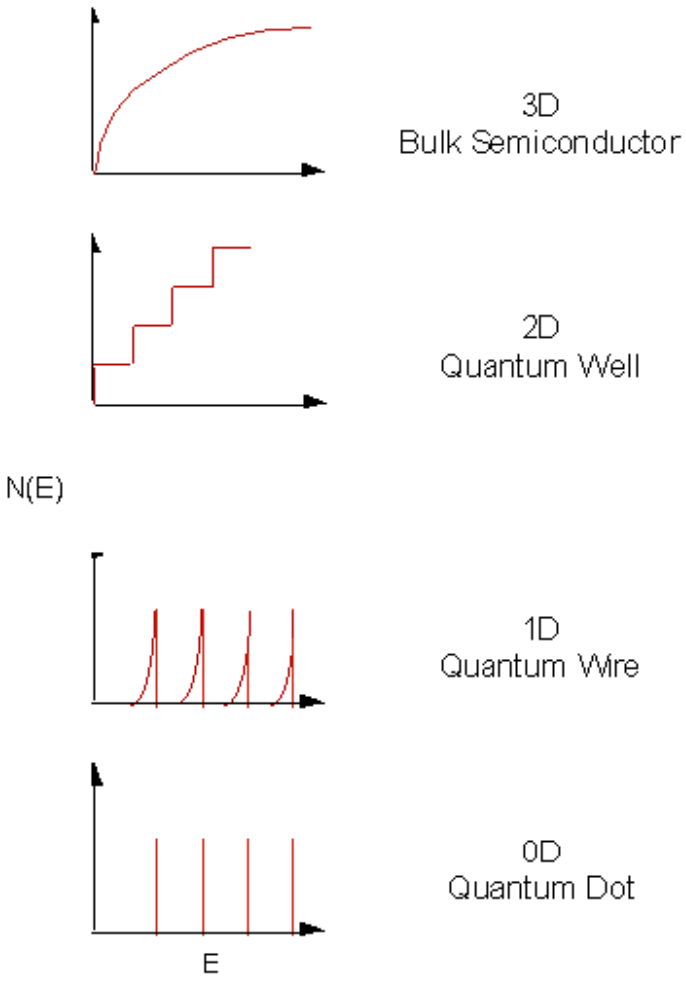

Figure 4.2: Schematic illustration of the joint density of states in semiconductor systems.

temperature: all valence bands are occupied and all conduction states are empty, thus making the band filling factor $A_{cv}(\omega)$ always equal to 1.

The polarization unitary vector **e** in Eq. (4.14) can assume whatever direction in case of an isotropic material, without affecting the physical properties, which are not dependent on the orientation of the sample. In case of an anisotropic crystal, a scalar quantity is no more sufficient to define the optical properties of the material: a dielectric tensor is needed instead. By choosing **e**, in three successive steps, along the three principal optical axes, we can calculate the three components of the diagonal dielectric tensor of the superlattice.

4.2 Results for bulk optical spectra

GaAs and AlAs present similar absorption properties: this is easy to understand, remembering that the two bulk semiconductors have extremely similar band structures (see Figs. 2.2 and 2.3 on pages 25 and 27). Interband absorption spectra of tetrahedral semiconductors are dominated by two prominent features, denoted E_1 and E_2 [8, 9]. The E_1 peak (and its spin-orbit counterpart $E_1 + \Delta_1$, which is not present in our calculated spectra) originates from band-to-band transitions along the Γ-L direction, where valence and conduction bands are nearly parallel: this results in a M_1-type critical point, i.e. a saddle point in the JDOS, which also gives a strong excitonic character to the transition. The E_2 peak, instead, has contributions from different parts of the Brillouin zone, but mainly from a region centered around the special point $(\frac{3}{4}, \frac{1}{4}, \frac{1}{4})$ (in units of $2\pi/a$, where a is the lattice constant). The E_2 peak has essentially no excitonic character. In a superlattice made of alternating GaAs and AlAs layers (or GaAs and vacuum layers), on the basis of the analysis we have presented for the superlattice band structures, we expect to recognize again the same characteristic features. In particular, in the region along the Γ-L direction, the electrons which contribute to the E_1 peak are confined in GaAs layers (see Fig. 2.5 on page 30). We are interested in comparing the bulk GaAs E_1 peak to the superlattice E_1 peaks at different well/barrier widths. In Fig. 4.3 we show the calculated real and imaginary parts of dielectric functions for bulk GaAs and AlAs crystals. Starting from the one-electron semi-empirical band structure, the complex dielectric function $\epsilon(\omega) = \epsilon_1 + i\epsilon_2$ is evaluated in a straightforward way by means of the semi-classical theory of interband transitions. The curves can be compared

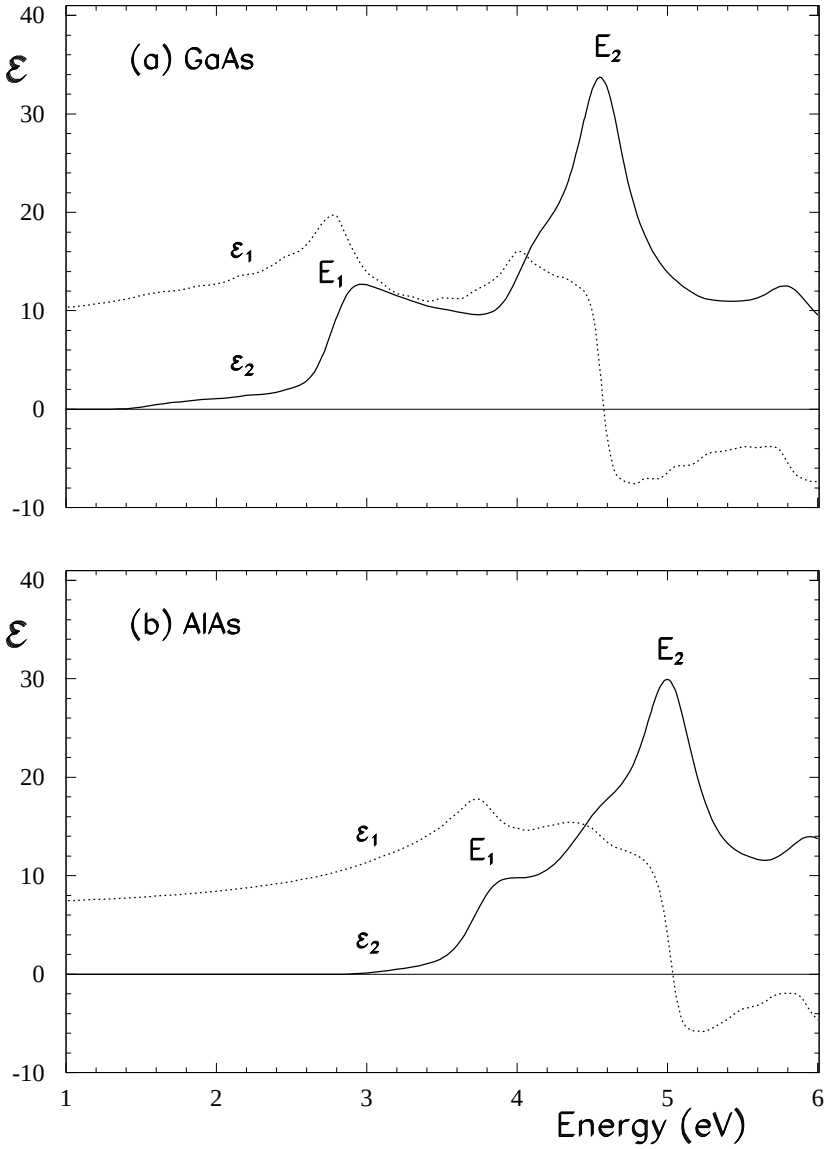

Figure 4.3: Calculated semi-empirical dielectric function (real and imaginary parts) of (a) GaAs and (b) AlAs.

with analogous measured data [120, 121], shown also later in Figs. 5.5 and 5.6 on pages 116 and 119. The agreement with the experimental positions of the peaks, is within a few tenths of an eV: we underline that the semi-empirical approach is free of the band gap problem. The height of the peaks, especially E_1, cannot be correctly estimated without the inclusion of the excitonic contributions and the local field effects.

Before calculating superlattice spectra, we have previously calculated bulk spectra for (001) $(GaAs)_{2p}$, i.e. we have described the cubic material as a periodic array of tetragonal supercells, repeating the test for different supercell lengths in the direction z. Integrating over the fcc Brillouin zone and the corresponding folded tetragonal Brillouin zone, using equivalent sets of Chadi and Cohen special points, we have verified the exact equivalence of the two results. An empirical Gaussian broadening of 0.1 eV has been used to produce smooth curves. The spectra obtained by the two different descriptions of the same system are perfectly superimposable. This check guarantees now the right to compare the bulk absorption curves with analogous superlattice curves, knowing that the differences cannot be due to uncontrollable errors in the numerical integration.

4.3 Optical spectra for GaAs/AlAs and GaAs/vacuum superlattices

We discuss now the spectra obtained for superlattice systems. Tetragonal Brillouin zone integrations are performed using Fourier quadrature with 1056 Chadi and Cohen special points in the irreducible wedge [64, 122]. The same set of special points had already been used for bulk $(GaAs)_{2p}$, to allow a direct comparison of results. The experimental broadening is simulated again by an empirical Gaussian broadening of 0.1 eV. The calculated imaginary part of the dielectric function $\epsilon_2(\omega)$ for both GaAs/AlAs and GaAs/vacuum systems are shown in Fig. 4.4 for different superlattice periods p. At this stage we are not interested in the absorption anisotropy, thus we average over the three orthogonal polarization directions to obtain a scalar dielectric function. Like the optical spectra of bulk GaAs and AlAs, superlattice spectra show two prominent features, namely E_1 and E_2 peaks (see Fig. 4.3): in

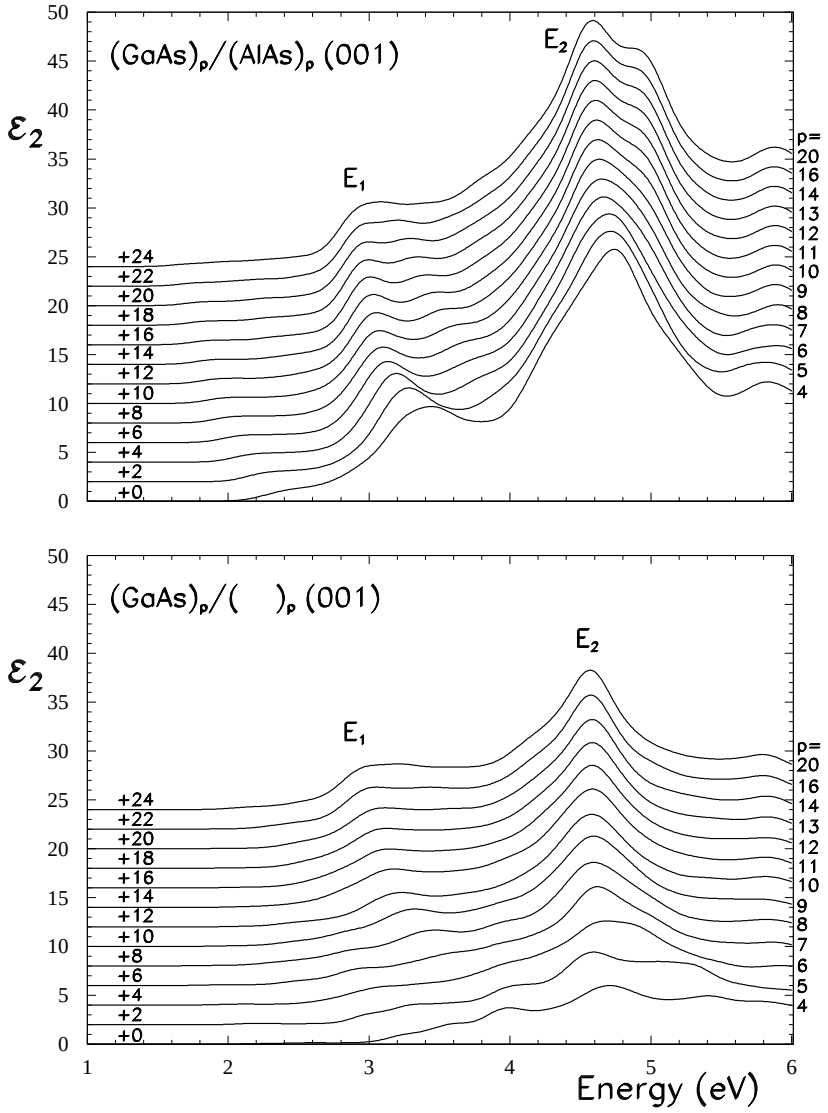

Figure 4.4: Imaginary part of the dielectric function for $(\mathrm{GaAs})_p/(\mathrm{AlAs})_p$ and $(\mathrm{GaAs})_p/(\mathrm{vacuum})_p$ superlattices, for different values of the period p, by semi-empirical calculations. Different curves are offset for clarity. E_1 splitting cannot be easily seen in the figure: the peak positions have been determined by an enlargement of the spectral region of interest.

fact, even if in a superlattice selection rules allow more transitions, as a consequence of zone-folding, the tetragonal Brillouin zone is smaller and, at last, all transitions which contribute to superlattice peaks have their equivalent counterparts in the bulk Brillouin zone. Another way to understand the similarity between bulk and superlattice optical spectra is to remember how close the superlattice band dispersion in Fig. 2.6 on page 33 is to the bulk band dispersion projected on the tetragonal Brillouin zone in Fig. 2.4 on page 28. As a general remark, the E_1 transition is found to blue shift and to split into two peaks for decreasing superlattice periods; the confinement-induced shift is larger for the GaAs/vacuum system. On the other hand the E_2 transition is split for large-period GaAs/AlAs superlattices, where the electronic states are confined in the two bulk layers leading to a superimposition of the two bulk spectra; the two peaks merge into a single one for small periods. A single E_2 peak with a small blue shift is found for GaAs/vacuum superlattices.

In Fig. 4.5 the peak energies are plotted as a function of the superlattice period p. First we comment on the behavior of E_1: in zinc-blend crystals it comes from transitions along the Λ line, in a region where bulk bands are almost parallel. When the system is confined in the [001] direction, it is not intuitive to describe the consequences of folding along $\langle 111 \rangle$ directions. The calculated spectra show that along the folded Λ line transitions subdivide in two main groups and lead to a splitting of the E_1 peak in the absorption curves. The two peaks have different oscillator strengths and, except for an intermediate period length, the lowest energy one becomes much stronger and covers the other one. Both peaks undergo confinement effects and are moved towards higher energies in comparison with their bulk position: the confinement and the consequent shifts are stronger at smaller well widths. A splitting of the E_1 transition with a blue shift of both peaks was indeed observed experimentally in GaAs/AlAs superlattices [10]. In the present calculation this is attributed to a splitting of the bulk valence band at the point L and along the Λ-line, as indicated by the band energies. The results of Figs. 4.4 and 4.5 show also that E_1 peak displacements are more relevant in GaAs/vacuum superlattices, where quantum confinement effects are stronger due to the vacuum barrier.

The behavior of the E_2 peak is substantially different: its main contribution

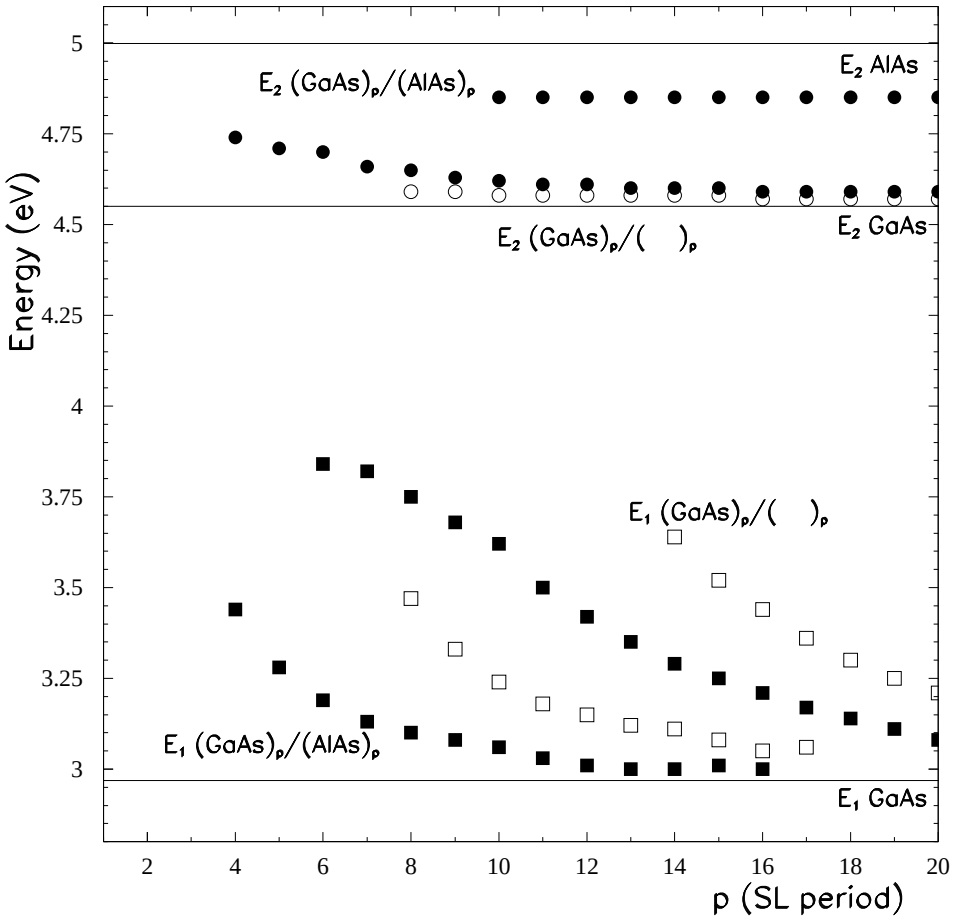

Figure 4.5: E_1 and E_2 peak positions for GaAs/AlAs (closed symbols) and GaAs/vacuum (open symbols) as a function of superlattice period p. The horizontal lines represent the peak energies in the bulk.

comes from transitions in a region close to the special point $\mathbf{k} = \frac{2\pi}{a}\left(\frac{3}{4}, \frac{1}{4}, \frac{1}{4}\right)$ [1]. At this **k**-point the alignment of both valence and conduction GaAs and AlAs bands is almost flat and the electronic wave functions are completely delocalized all over the heterostructure. This explains why E_2 peak in GaAs/AlAs superlattices is at an intermediate energy between bulk GaAs and AlAs E_2 peak positions and does not shift when the superlattice period p decreases. Our calculated peak positions are in good agreement with experimental data [123, 10, 11], and in particular a splitting of E_2 is reported in Ref. [11]. In GaAs/vacuum superlattices the situation changes: the electrons near the special point are confined in GaAs layers and the superlattice E_2 peak has a weak blue shift at small superlattice periods p, going back to the bulk GaAs E_2 energy when p grows. A single peak obviously arises in this case since there is no AlAs contribution. At last, we present in Fig. 4.6 some curves for the real part of the dielectric function ϵ_1 for GaAs/AlAs heterostructures. We observe that the average, or Penn gap (defined as the energy at which ϵ_1 goes through zero) does not depend on the superlattice period. This proves that the center of gravity of valence and conduction bands is preserved, as suggested in Ref. [16]: this follows from compensating effects of a blue shift at the bottom of the band (positive curvature) and a red shift at the top of the band (negative curvature).

4.4 Optical anisotropy and macroscopic dielectric tensor

In $(\mathrm{GaAs})_p/(\mathrm{AlAs})_p$ (001) superlattices the T_d cubic point group of the zinc-blend structure is replaced by the D_{2d} symmetry group. Cubic crystals present isotropic optical properties, while in a superlattice the reduction in symmetry leads to optical anisotropy in the real part of the dielectric constant (birefringence) and in the imaginary part (absorption anisotropy, or dichroism). The optical response can no longer be characterized by a complex dielectric function, in its place a complex dielectric tensor must be introduced. The GaAs/AlAs system is uniaxial, with the optical axis directed along the growth direction z, thus the dielectric tensor has the form:

$$\epsilon_{ij}(\omega) = \epsilon_{ii}(\omega)\ \delta_{ij}\,, \tag{4.23}$$

[1] What we call E_2 peak may in fact contain weak contributions from the E_0' transition, which can be clearly resolved only in derivative spectra. See e.g. Refs.[8, 10].

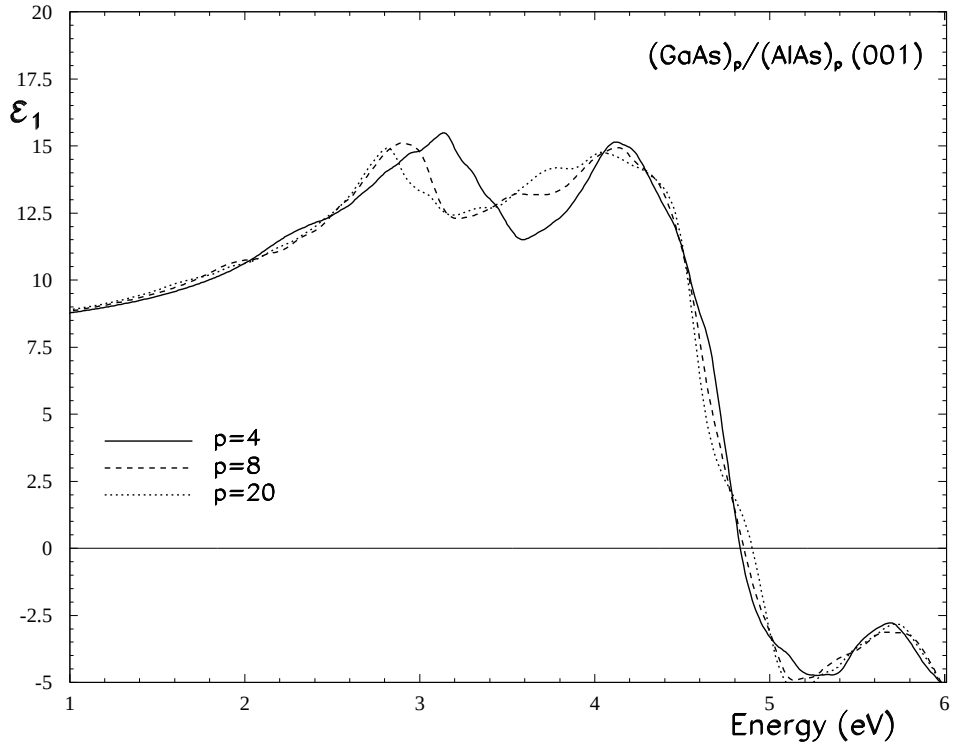

Figure 4.6: Real part of dielectric function for $(\mathrm{GaAs})_p/(\mathrm{AlAs})_p$ (001) superlattices, by semi-empirical calculations, for different values of the superlattice period p.

where $\epsilon_{xx} = \epsilon_{yy} = \epsilon_\perp$ and $\epsilon_{zz} = \epsilon_\parallel$ [2].

However, we do not hide that there are further complications. Besides the effects of spatial anisotropy, there are effects due to the spatial inhomogeneity of the solid, independently of his symmetry group. These are the local field effects, which will be discussed in the next chapter (see Section 5.2). The inclusion of local fields in calculations allow to account naturally for the intrinsic dielectric anisotropy of a multilayer, arising from different boundary conditions for an electric field parallel or perpendicular to the layers [113, 114]. This contribution to birefringence can be estimated for long wavelength of the incoming radiation and large superlattice periods p, in a classical effective medium model [27]. If boundaries are assumed abrupt and the constituent materials are supposed to conserve their bulk dielectric functions up to the interfaces, we can apply approximate expressions for $\epsilon_\perp$ and $\epsilon_\parallel$ in terms of bulk constituent scalar dielectric functions, ϵ_1 and ϵ_2 [113]:

$$\epsilon_\perp(\omega) = \frac{1}{l_1 + l_2}\left(\epsilon_1(\omega)\, l_1 + \epsilon_2(\omega)\, l_2\right) , \tag{4.24}$$

$$\epsilon_\parallel^{-1}(\omega) = \frac{1}{l_1 + l_2}\left(\frac{l_1}{\epsilon_1(\omega)} + \frac{l_2}{\epsilon_2(\omega)}\right) , \tag{4.25}$$

where l_1, l_2 are the layer thicknesses of the two different materials. Using semi-empirical calculated values of bulk static dielectric constants in expressions (4.24) and (4.25) we find a rough estimate $\Delta n \simeq 0.03$ for the local field contribution to birefringence at zero frequency. We know that this sizeable contribution at large superlattice periods will be missed in our calculations, as long as we neglect local field effects. Local field effects are known to depend on the superlattice period [3]. At this stage we decide not include local field effects: we directly take into account only the effects of electronic confinement and band folding on optical transitions. Comparison with birefringence data from Ref. [16], reported in Fig. 4.9, should allow to determine if the confinement and the band folding contributions to anisotropy

[2] In GaAs/vacuum superlattices, where the point group is C_{2v}, the system is biaxial with principal axes along [110], [1$\bar{1}$0], [001] and the dielectric constant for in-plane polarization has a slight additional anisotropy. The situation is analogous to heterostructures with no-common atom, where the in-plane anisotropy has been measured [124].

[3] The macroscopic treatment remains valid as long as the superlattice period remains much smaller than the wavelength of light, otherwise the superlattice should better be viewed as a one-dimensional photonic crystal, where local-field effects embodied in $\epsilon(\mathbf{G}, \mathbf{G}')$ lead to the formation of a band gap for light propagation [125].

can be sufficient to explain the behavior of the birefringence, at least when the superlattice period is intermediate/small.

4.5 Calculations of birefringence

In Fig. 4.7 we present an example of the calculated frequency dispersion of $\epsilon_{\parallel}$ and $\epsilon_{\perp}$, both for the real and imaginary parts: the birefringence is dispersionless up to energies close to the direct gap, while at higher energies it presents resonant contributions. We see, as expected, that folding and confinement can have a greater influence on the resonant part of the birefringence: indeed, transitions from valence subbands couple differently with xy or z-polarized electric fields. Note that the interband absorption edge is higher in energy for z-polarized light: this is in agreement with well known quantum well and superlattice physics, in which the lowest transition is a heavy hole one and is forbidden for light polarized along z [4]. Once again the effect is greater when confinement is stronger (small superlattice period p). There is a dispersionless contribution to birefringence at low frequencies of the order of 10^{-3}-10^{-2} that cannot be distinguished in Fig. 4.7. As proposed in Ref. [16], we decouple this low energy background birefringence, describing $\Delta n(\omega) = (\epsilon_{\perp})^{1/2} - (\epsilon_{\parallel})^{1/2}$ in terms of a fitting function,

$$\Delta n(\omega) = \Delta n_{bg} - \Delta n_{gap} \ln\left(1 - \left(\frac{\omega}{\omega_g}\right)^2\right), \tag{4.26}$$

where Δn_{bg} is the background contribution we want to isolate, the second term refers to the resonant contribution and ω_g is the gap frequency. In Ref. [16] the three parameters Δn_{bg}, Δn_{gap} and ω_g are extracted by fitting with expression (4.26) the experimental data. We also fit our calculated $\Delta n(\omega)$ curves by means of expression (4.26). In Fig. 4.8 we display the fit parameters as a function of the well width: the graphs can be easily compared with the analogous experimental curves presented in Fig. 4.9. The gap frequencies we extract by the fit agree both with directly calculated gaps (barely visible in Fig. 4.4) and with the measured ones [16]. Δn_{gap} shows an increase of the resonance for small periods: the theoretical curve reproduces the

[4] The polarization selection rule follows immediately from $\mathbf{k}\cdot\mathbf{p}$ theory, although a precise calculation of absorption spectra close to the fundamental gap should of course include the spin-orbit interaction [126].

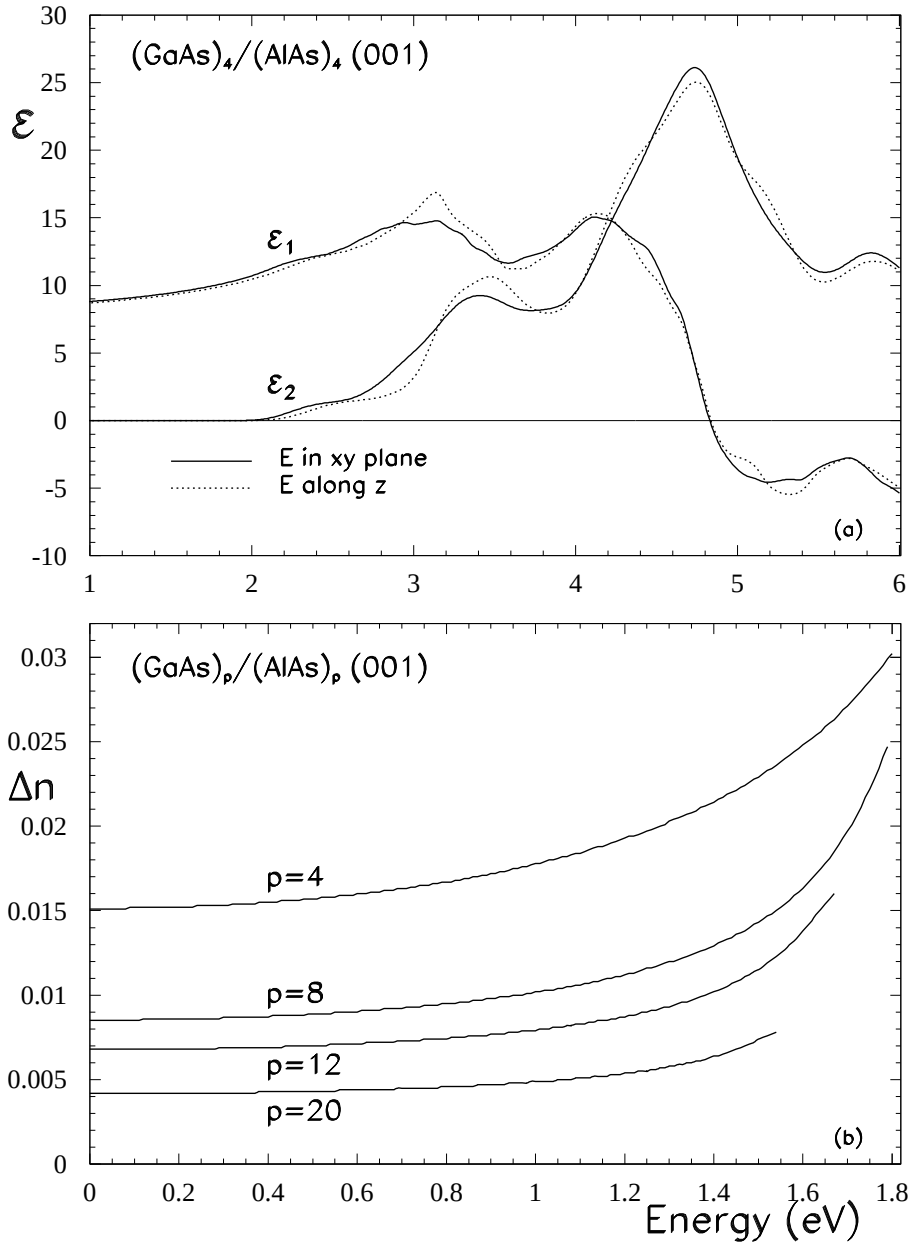

Figure 4.7: (a) Components of the dielectric tensor (real and imaginary parts) for a $(GaAs)_4/(AlAs)_4$ (001) superlattice and (b) linear birefringence Δn for $(GaAs)_p/(AlAs)_p$ (001) superlattices, by semi-empirical calculations.

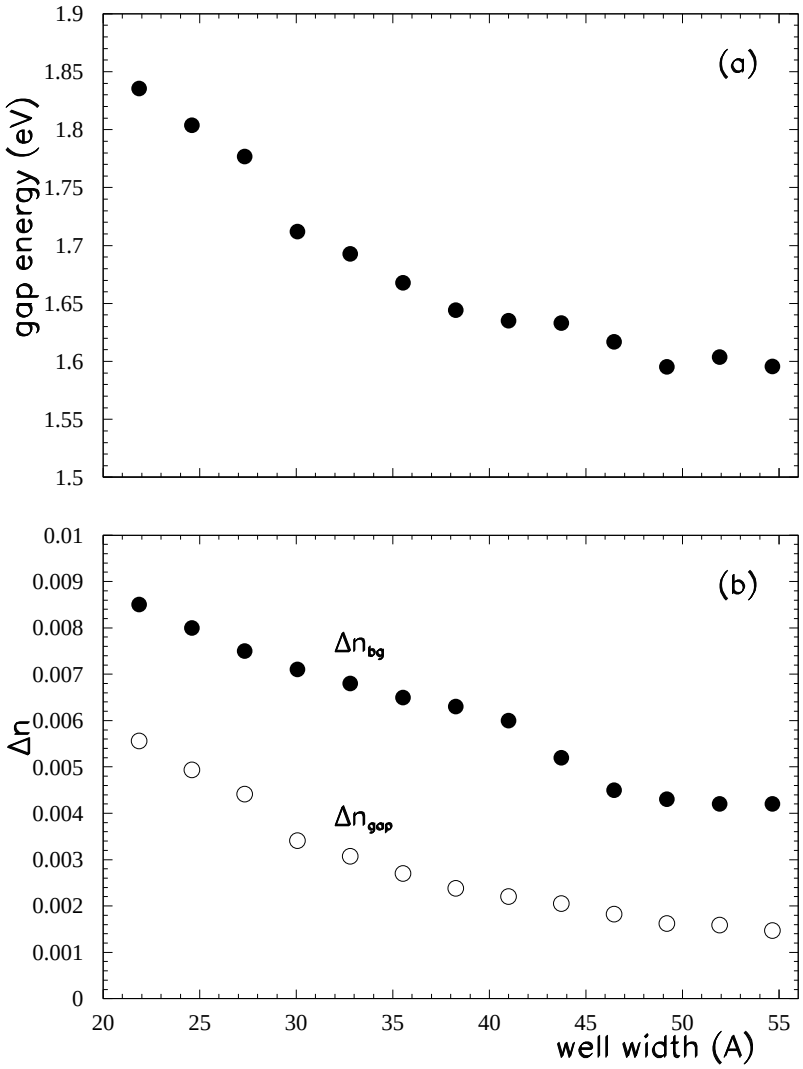

Figure 4.8: Parameters of equation (4.26) as a function of well width (half of a superlattice period): (a) energy gap, (b) Δn_{gap} and Δn_{bg}. The results can be compared with the analogous experimental graphs in Fig. 4.9.

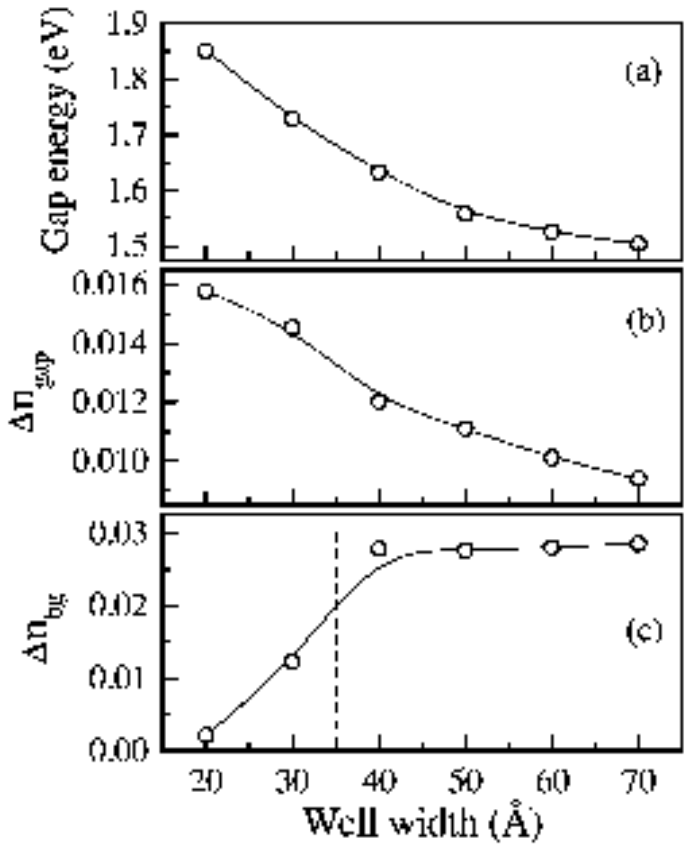

Figure 4.9: Experimental parameters of equation (4.26) as a function of well width (half of a superlattice period): (a) energy gap, (b) Δn_{gap} and Δn_{bg} from Ref. [16]

trend of the experimental curve, although the calculated values are significantly smaller. The sudden decrease of the measured background birefringence Δn_{bg} below 40 Å, on the other hand, is completely missing in our results. Moreover, the calculated magnitude of this term above 40 Å is remarkably underestimated. The fact suggests that folding effects give only a minor contribution, while the origin of the behavior of Δn_{bg} must be attributed to local field effects, as already suggested in Ref. [16]. Similar considerations can be made for the GaAs/vacuum systems.

The magnitude of the background birefringence related to local field effects can be estimated in the case of a long wavelength of the incident radiation and a not too small superlattice period p, thanks to the expressions in (4.24) and (4.25). The obtained value, i.e. 0.03, is much larger than the calculated values in Fig. 4.8, for all superlattice periods p, and it is of the same order of magnitude as the the experimental results at intermediate/large p. Only for small periods p, when relations (4.24) and (4.25) do not hold, the local field correction may not respect the analytic limit value. Nevertheless, the effects included in calculations fail to describe the small superlattice period region as well. Further calculations of the optical properties including local-field effects are obviously required to clarify this point.

In this chapter we have applied the semi-empirical LCBB technique and the semi-classical theory of interband transitions to cast light on how the optical spectra of bulk semiconductors evolve to superlattice spectra. We have discussed the adopted approximations, namely the independent-particle picture neglecting local field effects.

First, we have considered the average dielectric function. Quantum-confinement induced shifts of the critical point energies are calculated for both kinds of superlattices and are found to be larger for the GaAs/vacuum systems, where coupling between different GaAs layers is only due to quantum-mechanical tunneling and has a negligible effect. For both GaAs/AlAs and GaAs/vacuum superlattices, the E_1 peak in the absorption spectrum splits into two peaks with increasing blue shifts for decreasing superlattice period. This result agrees with the observations of Ref. [10] on GaAs/AlAs superlattices, and is attributed to a symmetry splitting of the valence bands along the line Γ-L. The blue shifts are always larger for the GaAs/vacuum systems. The E_2 transition instead is found to be split for large-period GaAs/AlAs superlattices, where the electronic states of the bulk are confined in each layer and

the absorption spectrum is the superimposition of the two bulk ones. The energy of the E_2 peak depends weakly on the superlattice period. The average or Penn gap, defined as the first zero of the real part of the dielectric constant, does not depend on the superlattice period, confirming the expectation that a blue shift at the lower absorption edges is compensated by red shifts in the upper parts of the absorption spectrum.

Second, we have studied the optical anisotropy. The band contribution to linear birefringence of GaAs/AlAs superlattices is calculated and compared with recent experimental results of Ref. [16]. The zero-frequency birefringence is found to be much smaller than the experimental results: we suppose that the missing contribution to observed static birefringence may be attributed to local-field effects, as already suggested in the experimental analysis of Ref. [16]. The frequency-dependent part of the birefringence arising from band folding and quantum confinement increases with decreasing superlattice period, as found in the experiment, although the calculated values are smaller. Once again, a better qualitative agreement could be obtained thanks to the inclusion of local field effects.

The presented results state the validity of the LCBB method, and its underlying approximations, to describe the averaged optical properties. Nevertheless, a deeper study is needed to understand optical anisotropy, in particular the origin of the behavior of the static birefringence as a function of the superlattice period.

Chapter 5

Ab-initio calculations of optical properties

After having discussed the empirical approach, we are going to turn our interest to first principle theoretical and computational tools in spectroscopic properties calculations. We have introduced in the previous chapter the complex problem of determining optical spectra in the whole visible region. A completely satisfactory solution of this task requires a description, which takes into account at the same time not only the detailed electronic structure, but also the many-body effects and the microscopic inhomogeneity of the medium. Non-trivial systems, like surfaces, clusters, semiconductor nanostructures, are today successfully treated in the *ab initio* framework, most often by constructing the excitation spectrum of the system as a sum over independent transitions between the states determined in the ground state calculation (i.e. using the one-electron energies and wavefunctions of the Kohn-Sham equation). This degree of approximation can be equivalent to the one adopted in our semi-empirical calculations of the optical spectra, which has provided a detailed analysis of the effects of band folding and confinement in semiconductor superlattices [28]. However, no quantitative agreement with the experiment has been found concerning the static birefringence, nor could semi-empirical independent-transition calculations explain, even qualitatively, the increase of the static birefringence with increasing superlattice period. One might suspect that the semi-empirical approach is not sufficiently precise to describe such a small effect as the birefringence. The

other strongly suspected reason for failure is the inadequacy of the basic approximations used to determine the macroscopic dielectric function. In particular, we expect that the local field effects can play a very important role. Both the points call for a more detailed investigation into the anisotropy of the optical response.

In order to go beyond the simple independent-transition picture for the description of two-particle excitations, like absorption spectroscopy, the most important corrections to be included are the full electron-electron and electron-hole interactions and local field effects. Let us discuss now more in detail these effects. Local field effects express the fact that, related to the inhomogeneity of the material, its response to an external potential with given spatial frequency will include, in principle, all other spatial frequencies determined by the reciprocal lattice vectors of the periodic system. This implies that, technically, the size of the problem which has to be dealt with is considerably bigger than for the simple sum of transitions and, in fact, local field effects are often omitted in calculations. However, superlattices are intrinsically inhomogeneous, and these effects can therefore be expected to play an important role in their optical and dielectric properties. The Kohn-Sham eigenvalues are not meant to describe electron addition and removal energies: only quasi-particle energies, which can be obtained within the many-body theory, are suitable to describe the changes in total energy occurring in direct and inverse photoemission processes. However, quasi-particle corrections are still not enough to describe all the effects arising in an absorption process, where interacting electron-hole pairs are created. In fact, another effect, well known to be important for optical spectra, is the electron-hole interaction, or excitonic effect. This effect is due to the fact that the created electron-hole pair may interact more or less strongly, leading to bound states within the gap and/or to strong deformations above the continuum absorption edge. The importance of these effects depends on the size of the screening of the electron-hole interaction and on the details of the band structure. In particular for flat bands, which are linked to the existence of localized (confined) states, this effect is expected to be very strong. Hence, due to the confinement properties of superlattices, their spectra are expected to show relevant excitonic effects. At the moment we want to focus on the superlattice birefringence at zero frequency and not on the whole absorption spectra: as the static birefringence is a ground state property, we

can expect that neglecting quasi-particle corrections and excitonic effects has not a dramatic influence on the results. As a matter of fact, we will show that only when local field effects are included qualitative and even quantitative agreement with the experiment can be achieved. These results will be discussed in the first part of this chapter.

In the second part, we will go back to the problem of electron-electron and electron-hole interactions, to study the line-shape of absorption spectra up to 7 eV for bulk GaAs and AlAs systems. The calculation of optical spectra for bulk semiconductors is a widely investigated subject. In the last decades the many-body perturbation theory has produced expressions both for the self-energy and the electron-hole interaction, which are successfully used in computational physics. The self-energy Σ is usually obtained within Hedin's GW approach, starting from DFT results as a zero-order solution. Similarly, the excitonic effects are well described by the Bethe-Salpeter equation (BSE), via a functional derivative of the self-energy Σ. However, the many-body perturbation theory is not the only approach developed to deal with response properties. The limits of DFT comes from the fact that excited states, are not accessible through static ground state DFT. In principle, these problems can be overcome, at least as far as optical excitations are concerned, by taking into account the fact that in the absorption experiment the system is responding to a time-dependent external field. Therefore a generalization of static DFT to Time-Dependent DFT (TDDFT) has been proposed [127, 128], i.e. all potentials are now functionals of the *time-dependent* density. Besides the potentials, also their functional derivatives with respect to the density are needed (at least implicitly), since the system is responding self-consistently to the applied perturbation. As it happened in static DFT, again, the main problem resides in finding a good approximation to the exchange-correlation contribution. The time-dependent DFT approach still keeps the advantage of the static one to be computationally very efficient, and could in principle replace other successful, but more cumbersome methods like the Bethe-Salpeter approach (BSE)[129, 130, 131, 132]. However, there are some additional difficulties with respect to the case of static DFT: in the present chapter we will mainly deal with the determination of reliable approximations for the time-dependent density variation of the exchange-correlation potential V_{xc}, i.e.

the so-called exchange-correlation (xc) kernel, $f_{xc} = \delta V_{xc}/\delta\rho$.

Real calculations are dependent on the chosen approximation for the xc kernel f_{xc}: the lowest level of approximation (RPA) consists in neglecting the kernel, another simple approximation is the adiabatic local density approximation (TDLDA) [133, 134], where the kernel is calculated from the LDA exchange-correlation potential V_{xc}^{LDA}. At present, the simple adiabatic local density approximation for the TDDFT kernel has given promising results for finite systems, but does not succeed in describing absorption spectra in solids. Improvements might come through the inclusion of dynamical (memory) effects and/or long-range nonlocal terms [128, 135]. Recently, Reining *et al.* [30] have shown that a *static* long-range contribution (LRC) can simulate the strong continuum excitonic effect in the absorption spectrum of bulk Silicon. Here we present the results for GaAs and AlAs spectra. We will show that the optical absorption, which exhibits a strong continuum exciton effect, is considerably improved with respect to calculations where the adiabatic local density approximation is used.
We underline that the calculations concerning the superlattice zero-frequency birefringence have been performed within a time-dependent DFT formalism as well. Also in this case, we will discuss the different approximations adopted to describe the xc kernel f_{xc}.

5.1 Time Dependent Density Functional Theory

We discuss here the essential formalism of the time-dependent generalization of DFT. For detailed information on this subject, we suggest to refer to some recent reviews [128, 136, 137, 138, 139]. The Density Functional Theory, as described in Chapter 3, is a ground state theory, thus unable to account for electronic excitations. These restrictions can be overcome within the DFT formalism, generalizing it by allowing a time dependence for the external field. As in classical mechanics, the DFT ground state is determined by the energy minimum:

$$\delta E[\rho]/\delta\rho(\mathbf{r}) = 0\,. \tag{5.1}$$

Extending the analogy, as the trajectory of a classical system is given by the extrema of the classical action $\int_{t_0}^{t_1} dt L(t)$, where L is the Lagrangian, the evolution of a

quantum system, which undergoes an external time-dependent potential $V_{ext}(\mathbf{r},t)$, is given by the extrema of the quantum mechanical action:

$$A = \int_{t_0}^{t_1} dt \langle \Psi(t)| i\frac{\partial}{\partial t} - \hat{H}(t)|\Psi(t)\rangle \,. \tag{5.2}$$

Of course, there are some theorems [127], exactly analogous to the Hohenberg-Kohn theorems (see Section 3.1.1) and presented within a framework similar to the Kohn-Sham scheme (see Section 3.1.2). A first theorem proves that there is a bijective correspondence between time-dependent external potentials $V_{ext}(\mathbf{r},t)$ and v-representable time-dependent densities $\rho(\mathbf{r},t)$. A second theorem proves that the evolution of the system is determined by the extrema of the quantum mechanical action. Van Leeuwen [140] has shown that the time-dependent density, which characterizes a many-body system can be, in principle, reproduced by a time-dependent external potential, in a many-body system with no two-particle interactions. This property allows to represent at any time the density of a many-body system by means of a non-interacting system, which reproduce the exact interacting density $\rho(\mathbf{r},t)$. The evolution of the system is described by the time-dependent KS-equations:

$$\left[-\frac{1}{2}\nabla^2 + V_{eff}(\mathbf{r},t)\right]\psi_i(\mathbf{r},t) = i\frac{\partial}{\partial t}\psi_i(\mathbf{r},t)\,, \tag{5.3}$$

$$\rho(\mathbf{r},t) = \sum_{i=1}^{N} |\psi_i(\mathbf{r},t)|^2\,, \tag{5.4}$$

where

$$V_{eff}(\mathbf{r},t) = V_H(\mathbf{r},t) + V_{xc}(\mathbf{r},t) + V_{ext}(\mathbf{r},t) \tag{5.5}$$

is, as in the static case, the effective potential felt by the electrons. It consists of the sum of the external time-dependent applied field, the time-dependent Hartree term, plus the exchange-correlation potential (defined through the equivalence between the interacting and fictitious non-interacting systems). From the variational principle, it is possible to define:

$$V_{xc}(\mathbf{r},t) = \frac{\delta A_{xc}[\rho]}{\delta\rho(\mathbf{r},t)}\,, \tag{5.6}$$

where $A_{xc}[\rho]$ is the exchange-correlation part of the action functional A. Besides its elegance, the most remarkable quality of the time dependent DFT is in its computational simplicity, in comparison to other available methods.

5.1.1 Derivation of an expression for the dielectric function

The linear response of the charge density to an external time-dependent perturbation is determined by the polarizability χ of the medium:

$$\chi(\mathbf{r},t,\mathbf{r}',t') = \left.\frac{\delta\rho(\mathbf{r},t)}{\delta V_{ext}(\mathbf{r}',t')}\right|_{V_{ext}=0} . \tag{5.7}$$

The Eq. (5.7) means that the density $\rho(\mathbf{r},t)$ and the external potential are related in the following way :

$$\rho(\mathbf{r},t) = \rho(\mathbf{r},t_0) + \int \chi(\mathbf{r},t,\mathbf{r}',t')V_{ext}(\mathbf{r}',t')d\mathbf{r}'dt' + \mathcal{O}(V_{ext}^2)\,. \tag{5.8}$$

The independent-particle polarization χ_0 relates, in a fully equivalent way, the electron density $\rho(\mathbf{r},t)$ to the effective potential $V_{eff}(\mathbf{r},t)$:

$$\chi_0(\mathbf{r},t,\mathbf{r}',t') = \left.\frac{\delta\rho(\mathbf{r},t)}{\delta V_{eff}(\mathbf{r}',t')}\right|_{V_{eff}=0} . \tag{5.9}$$

Remembering the definition of the effective-potential, $V_{eff} = V_{ext} + V_H + V_{xc}$, it is easy to obtain:

$$\begin{aligned}\frac{\delta V_{eff}(\mathbf{r},t)}{\delta V_{ext}(\mathbf{r}',t')} &= \delta(\mathbf{r}-\mathbf{r}')\delta(t-t')+ \\ &\int\left[\frac{\delta(t-t'')}{|\mathbf{r}-\mathbf{r}''|} + f_{xc}(\mathbf{r},t,\mathbf{r}'',t'')\right]\chi(\mathbf{r}'',t'',\mathbf{r}',t')d\mathbf{r}''dt''\,,\end{aligned} \tag{5.10}$$

where

$$f_{xc}(\mathbf{r},t,\mathbf{r}',t') = \left.\frac{\delta V_{xc}[\rho(\mathbf{r},t)]}{\delta\rho(\mathbf{r}',t')}\right|_{V_{ext}=0} \tag{5.11}$$

is the time-dependent xc kernel and

$$v(x,x') = v(\mathbf{r},\mathbf{r}')\,\delta(t-t') = \frac{\delta(t-t'')}{|\mathbf{r}-\mathbf{r}''|} \tag{5.12}$$

accounts for the variation of the Hartree potential. After deriving the simple relation:

$$\delta\rho/\delta V_{ext} = (\delta\rho/\delta V_{eff})(\delta V_{eff}/\delta V_{ext}) \equiv \chi_0\delta V_{eff}/\delta V_{ext}\,, \tag{5.13}$$

a Dyson-like equation, which connects the two polarizabilities χ and χ_0, follows in a straightforward way:

$$\begin{aligned}\chi(\mathbf{r},\mathbf{r}';\omega) &= \chi_0(\mathbf{r},\mathbf{r}';\omega)+ \\ &\int d\mathbf{r}_1 d\mathbf{r}_2\chi_0(\mathbf{r},\mathbf{r}_1;\omega)\left[\frac{1}{|\mathbf{r}_1-\mathbf{r}_2|} + f_{xc}(\mathbf{r}_1,\mathbf{r}_2,\omega)\right]\chi(\mathbf{r}_2,\mathbf{r}';\omega)\,.\end{aligned} \tag{5.14}$$

This scheme allows to describe the exact linear response of an interacting system in terms of the response of a non-interacting system with external potential $V_{eff}(\mathbf{r}, t)$. The exact exchange-correlation contributions are of course unknown, and the application of the theory relies on some approximations. The lowest level of approximation (RPA) consists in neglecting the kernel:

$$f_{xc}^{RPA} = 0\,. \tag{5.15}$$

Another simple approximation is the adiabatic local density approximation (TDLDA) [133, 134], where the kernel is calculated from the LDA exchange-correlation potential used in ground state calculations:

$$f_{xc}^{TDLDA}(\mathbf{r}) = \delta\left(\mathbf{r}, \mathbf{r}'\right) \frac{dV_{xc}^{LDA}(\mathbf{r})}{d\rho(\mathbf{r})}\,. \tag{5.16}$$

Inverting formally Eq. (5.14), one obtains a compact equation

$$\chi = \left[1 - \chi_0(v + f_{xc})\right]^{-1} \chi_0\,, \tag{5.17}$$

where v is the Coulomb potential. The inverse dielectric function ϵ^{-1} measures the screening in the system:

$$\epsilon^{-1}\left(\mathbf{r}, t, \mathbf{r}', t'\right) = \frac{\delta V_{eff}(\mathbf{r}, t)}{\delta V_{ext}(\mathbf{r}', t')}\,. \tag{5.18}$$

In practice, we need the inverse dielectric function in the momentum space, which is related by a Fourier transform to real space:

$$\epsilon^{-1}\left(\mathbf{r}, \mathbf{r}'; \omega\right) = \frac{1}{(2\pi)^3} \int_{BZ} d\mathbf{q} \sum_{\mathbf{G},\mathbf{G}'} e^{i(\mathbf{q}+\mathbf{G})\cdot\mathbf{r}}\, \epsilon^{-1}_{\mathbf{G}\mathbf{G}'}\left(\mathbf{q}, \omega\right)\, e^{-i(\mathbf{q}+\mathbf{G}')\cdot\mathbf{r}'}\,. \tag{5.19}$$

Some care must be taken in the origin of the induced screening. If the probe is assumed to be a test particle, it is only affected by the electrostatic Hartree term in equation (5.10). From Eq. (5.10) it follows that the inverse dielectric function is connected to the polarizability by the relation:

$$\epsilon^{-1} = 1 + v\chi\,. \tag{5.20}$$

The random phase approximation (RPA) response function is obtained, simply imposing $f_{xc} = 0$:

$$\epsilon^{-1}_{RPA} = 1 + v\left(1 - \chi_0 v\right)^{-1} \chi_0\,. \tag{5.21}$$

Then, inverting the matrix relation and using the matrix equality

$$(1 - \chi_0 v)^{-1} \chi_0 = \chi_0 (1 - v\chi_0)^{-1}, \tag{5.22}$$

we obtain:

$$\epsilon_{RPA} = 1 - v\chi_0 . \tag{5.23}$$

In conclusion, all we need to perform calculations is an explicit formulation of the polarizability. Application of first-order perturbation theory to the Kohn-Sham equations (3.20) yields the standard result for the independent-particle polarization χ_0 in the Adler-Wiser formulation [115, 116]:

$$\chi_0 (\mathbf{r}, \mathbf{r}'; \omega) = 2 \sum_{i,j} (f_i - f_j) \frac{\phi_i(\mathbf{r}) \phi_j^*(\mathbf{r}) \phi_i^*(\mathbf{r}') \phi_j(\mathbf{r}')}{\epsilon_i - \epsilon_j - \omega - i\eta}, \tag{5.24}$$

where f_i are the occupation numbers $(0, 1)$ and η is a positive infinitesimal number. The small imaginary constant added in the denominator accounts for causality, and describes lifetime effects when it is small, but finite; the factor 2 stems from spin degeneracy. The explicit Fourier transformation of the independent-particle polarization results:

$$\chi_0^{\mathbf{G}\mathbf{G}'} (\mathbf{q}, \omega) = 2 \sum_{i,j} (f_i - f_j) \frac{\langle j | e^{-i(\mathbf{q}+\mathbf{G})\cdot\mathbf{r}} | i \rangle \langle i | e^{i(\mathbf{q}+\mathbf{G}')\cdot\mathbf{r}'} | j \rangle}{\epsilon_i - \epsilon_j - \omega - i\eta} . \tag{5.25}$$

5.1.2 RPA approximation without local field effects

It is interesting to establish a link between the formula (4.14) in Section 4.1. for the imaginary part of the dielectric function and the analogous formula within the RPA approximation, which we can derive starting from the expression for χ_0 in Eq. (5.25). At this stage, we continue neglecting local field effects, to preserve the correspondence with the semi-empirical calculations. From Eqs. (5.23) and (5.25) we obtain:

$$\epsilon_M (\omega) = 1 + 2\frac{4\pi}{\Omega} \lim_{\mathbf{q}\to 0} \frac{1}{q^2} \sum_{\mathbf{k}\in BZ} \sum_{v,c} \left[\frac{|\langle n_c, \mathbf{k}+\mathbf{q} | e^{i\mathbf{q}\cdot\mathbf{r}} | n_v, \mathbf{k} \rangle|^2}{\epsilon_{n_c,\mathbf{k}+\mathbf{q}} - \epsilon_{n_v,\mathbf{k}} - (\omega + i\eta)} + \frac{|\langle n_c, \mathbf{k}-\mathbf{q} | e^{-i\mathbf{q}\cdot\mathbf{r}} | n_v, \mathbf{k} \rangle|^2}{\epsilon_{n_c,\mathbf{k}-\mathbf{q}} - \epsilon_{n_v,\mathbf{k}} + (\omega + i\eta)} \right], \tag{5.26}$$

where we have used the Fourier transformation of the Coulomb potential:

$$\frac{1}{|\mathbf{r}|} = \frac{4\pi}{\Omega} \sum_{\mathbf{q},\mathbf{G}} \frac{e^{i(\mathbf{q}+\mathbf{G})\cdot\mathbf{r}}}{|\mathbf{q}+\mathbf{G}|^2} \,. \tag{5.27}$$

Since the second term (anti-resonant) does not contribute to the absorption, we can reject it:

$$\epsilon_2(\omega) = 2\frac{4\pi}{\Omega} \lim_{\mathbf{q}\to 0} \frac{1}{q^2} \sum_{\mathbf{k}\in BZ} \sum_{n_v,n_c} Im\left[\frac{|\langle n_c, \mathbf{k}+\mathbf{q}|e^{i\mathbf{q}\cdot\mathbf{r}}|n_v,\mathbf{k}\rangle|^2}{\epsilon_{n_c,\mathbf{k}+\mathbf{q}} - \epsilon_{n_v,\mathbf{k}} - (\omega + i\eta)} \right] . \tag{5.28}$$

For a non-local Hamiltonian H, the commutator with the coordinate operator is given by:

$$\frac{d}{dt}\mathbf{r}_i = i\left[H, \mathbf{r}_i\right] = \mathbf{p}_i + i\left[V_{nl}, \mathbf{r}_i\right] \,, \tag{5.29}$$

where V_{nl} is the non-local part of the Hamiltonian. Another way to write the previous expression is [141]:

$$v_\alpha = \lim_{q\to 0} \left[H, e^{iqr_\alpha}\right]/q \,, \tag{5.30}$$

where v_α and r_α are, for $\alpha = x, y, z$, the Cartesian components of $\mathbf{v}$ and $\mathbf{r}$. Applying now Eqs. (5.29) and (5.30) to simplify Eq. (5.28), we obtain

$$\lim_{q\to 0} \langle n_c, \mathbf{k}+\mathbf{q}|e^{i\mathbf{q}\cdot\mathbf{r}}|n_v,\mathbf{k}\rangle/q = \frac{\mathbf{e}\cdot\langle n_c,\mathbf{k}|\frac{\nabla}{i} + i\left[V_{nl},\mathbf{r}\right]|n_v,\mathbf{k}\rangle}{\epsilon_c^{KS} - \epsilon_v^{KS}} \,, \tag{5.31}$$

where $\mathbf{e}$ is a polarization unitary vector, pointing in the direction of $\mathbf{q}$. We have indicated explicitly that the eigenvalues in the denominator are Kohn-Sham eigenvalues, because they derive by the application of the Kohn-Sham Hamiltonian, even if GW corrections are added. In fact, the use of the quasi-particle Hamiltonian to calculate the commutator would be much more demanding, because the self-energy operator Σ is non-local and dynamical. Hence, the final formula in the RPA approximation, neglecting local field effects is:

$$\epsilon_2(\omega) = 2\frac{4\pi}{\Omega} \lim_{\mathbf{q}\to 0} \sum_{\mathbf{k}\in BZ} \sum_{n_v,n_c} \left| \frac{\mathbf{e}\cdot\langle n_c,\mathbf{k}|\frac{\nabla}{i} + i\left[V_{nl},\mathbf{r}\right]|n_v,\mathbf{k}\rangle}{\epsilon_c^{KS} - \epsilon_v^{KS}} \right|^2 \left[\frac{1}{\epsilon_{n_c,\mathbf{k}+\mathbf{q}} - \epsilon_{n_v,\mathbf{k}} - (\omega + i\eta)} \right] . \tag{5.32}$$

We want to show that the expression (5.28) is equivalent to the expression (4.14):

$$\epsilon_2(\omega) = 2\frac{4\pi^2}{\Omega}\frac{1}{\omega^2} \sum_{n_c,n_v} \sum_{\mathbf{k}\in BZ} |\mathbf{e}\cdot\mathbf{M}_{\mathbf{cv}}(\mathbf{k})|^2 \,\delta\left(\omega_c(\mathbf{k}) - \omega_v(\mathbf{k}) - \omega\right) \,. \tag{5.33}$$

Exploiting once again Eqs. (5.29) and (5.30), we can rewrite it in a slightly different way:

$$\epsilon_2(\omega) = 2\frac{4\pi^2}{\Omega}\lim_{\mathbf{q}\to 0}\frac{1}{q^2}\sum_{n_c,n_v}\sum_{\mathbf{k}\in BZ}\left|\langle n_c,\mathbf{k}+\mathbf{q}|e^{i\mathbf{q}\cdot\mathbf{r}}|n_v,\mathbf{k}\rangle\right|^2\delta\left(\omega_c(\mathbf{k})-\omega_v(\mathbf{k})-\omega\right)\,, \tag{5.34}$$

which is the imaginary part of Eq. (5.28). In fact:

$$\lim_{\eta\to 0}\frac{1}{x\pm i\eta} = P\frac{1}{x}\mp i\pi\delta\left(x\right)\,. \tag{5.35}$$

5.2 Local field effects

A solid which possesses lattice-potential symmetry is non-homogeneous on the microscopic scale, even when it is characterized by a cubic symmetry group, which yields isotropic optical properties. When an external perturbing field of small wave vector $\mathbf{q}$ and frequency ω is applied to the system, the local field will in general contain "Bragg reflected" terms, i.e. dependent on the wave vector $\mathbf{q}+\mathbf{G}$, where $\mathbf{G}$ is a reciprocal lattice vector. These microscopically varying terms fluctuate on the wavelength of the interatomic spacing. The frequency ω is not affected, supposing the homogeneity of the time. The difference between the local and the macroscopic field constitutes the local-field corrections in the electromagnetic response.

Let us consider an electric field $\mathbf{E}$, incoming on a non-homogeneous medium. In the linear approximation, the polarization effects are described by the electric displacement vector $\mathbf{D}$:

$$\mathbf{D}(\mathbf{q}+\mathbf{G},\omega) = \sum_{\mathbf{G}'}\epsilon_{mic}(\mathbf{q}+\mathbf{G},\mathbf{q}+\mathbf{G}';\omega)\,\mathbf{E}(\mathbf{q}+\mathbf{G}',\omega)\,. \tag{5.36}$$

We are interested in a relation which, in the limit of a negligible $\mathbf{q}$, consider only macroscopic quantities:

$$\mathbf{D}_M(\omega) = \epsilon_M(\omega)\mathbf{E}_M(\omega)\,. \tag{5.37}$$

According to Adler [115] and Wiser [116], the macroscopic dielectric tensor can be related to the inverse of the microscopic dielectric matrix [117, 118]:

$$\epsilon_M(\omega) = \lim_{\mathbf{q}\to 0}\left.\frac{1}{\epsilon^{-1}_{\mathbf{G}\mathbf{G}'}\left(\mathbf{q},\omega\right)}\right|_{\mathbf{G}=\mathbf{G}'=0}\,. \tag{5.38}$$

The difference between an homogeneous and non-homogeneous medium lies in the off-diagonal terms. In the direct space this means that the microscopic dielectric function $\varepsilon(\mathbf{r}, \mathbf{r}')$ depends explicitly on the positions $\mathbf{r}$ and $\mathbf{r}'$, and not simply on the distance $|\mathbf{r} - \mathbf{r}'|$. If the medium were homogeneous, the macroscopic dielectric function would be

$$\epsilon_M = \lim_{q \to 0} \epsilon_{\mathbf{G}=0,\mathbf{G}'=0} \,, \tag{5.39}$$

i.e. the spatial average of the microscopic dielectric function. In case of isotropic media, the direction in which the limit of the small $\mathbf{q}$ vector has to be taken is non-influent. In case of a GaAs/AlAs superlattice, taking the limit of $\mathbf{q}$ in the z or x/y directions gives respectively the components $\epsilon_{\parallel}$ and $\epsilon_{\perp}$ of the dielectric tensor, which include local field effects (LFE).

5.3 Results for the birefringence of GaAs/AlAs superlattices

The reduction of the original cubic symmetry of the diamond or zinc-blend structure gives rise to an optical anisotropy in GaAs/AlAs superlattices [16]. As we have already discussed in the previous chapter, the birefringence in perturbed bulk semiconductors has two well-known contributions [142, 143], namely a dispersionless term related to virtual direct transitions involving high energy gaps between valence and conduction bands, and a resonant term which represents the isolated effects of the virtual transitions associated with the small energy gaps between the top valence bands and the first conduction bands. We have calculated the static birefringence of (001) $(\mathrm{GaAs})_p/(\mathrm{AlAs})_p$ superlattices for the barrier/well period p=1 to p=8, employing the *ab initio* DFT approach which should a priori describe details of the band structure in a more reliable way, if compared to an empirical approach. In fact, one might suspect that the semi-empirical approach is not sufficiently precise to describe such a quantity as the birefringence which requires calculations of high precision, being a very small (of the order of 10^{-2}) difference between two dielectric constants. However, we will see that this rather technical point turns out not to be the main source of error in the calculations in Chapter 4. We have proved in Section 5.1.2 that TDDFT calculations without local field effects, within the RPA

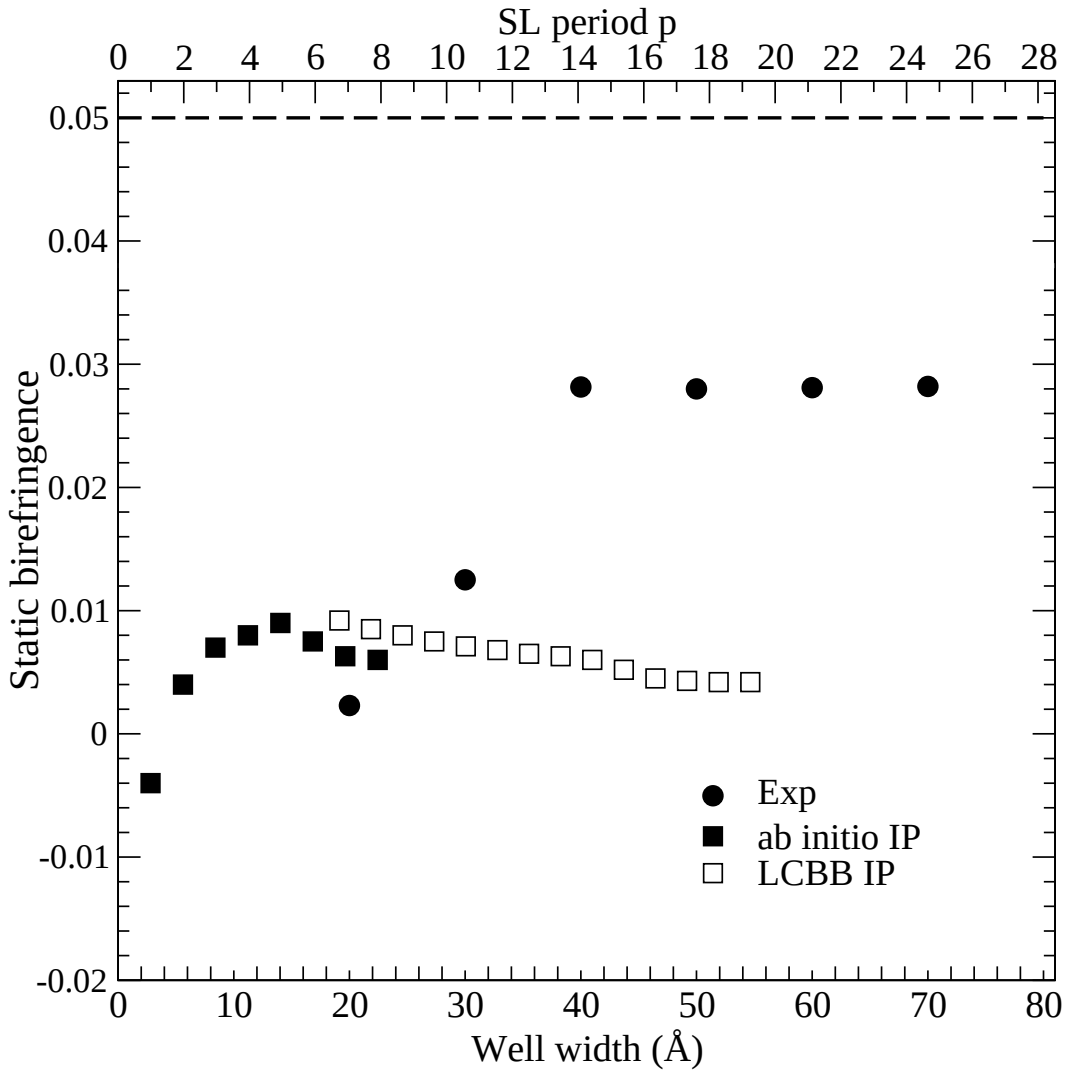

Figure 5.1: Static birefringence for $GaAs_p/AlAs_p$ superlattices as a function of p. Circle: experiment from Ref. [16]. Filled square: RPA theoretical values without local fields. Empty square: semi-empirical theoretical values without local fields. The effective medium value calculated with the theoretical RPA (with local fields) dielectric constants of bulk GaAs and AlAs is indicated by the horizontal dashed line (see text).

approximation for the xc-kernel, yield optical spectra totally equivalent to the ones we have calculated within the semi-empirical framework. In Fig. 5.1 we compare *ab initio* and semi-empirical calculations without local field effects. The two curves show the same trend as a function of the superlattice period p. The values of the birefringence are moreover completely compatible: the TDDFT calculations confirm hence the semi-empirical results. In our *ab initio* calculation we have carefully checked the symmetries of the wavefunctions and of the energy levels. In particular, the symmetry operation which makes x and y axes equivalent for a tetragonal superlattice belongs to a non-symmorfic point group, whereas the codes used can consider only symmorfic point groups. Thus, we had to work on improving the convergence of the wavefunctions, to assure that the x and y components of the dielectric tensor could be equal up to 10^{-5}, and, as a consequence, that the calculated birefringence could not contain uncontrolled errors due to asymmetries.

It is well known that many-body effects beyond the simple independent-particle picture often drastically alter the dielectric properties of materials. Self-energy and excitonic effects can have a significant contribution to the absorption spectra of even simple bulk semiconductors, and by consequence also change their dielectric constants. These effects are due to variations of the exchange-correlation potential upon excitation. Of course, there are also contributions stemming from variations of the Hartree potential, including the so-called local field effects, which express the fact that these variations reflect the charge inhomogeneity of the responding material. Therefore, local field effects can be of moderate importance, compared to the exchange-correlation contributions, for example in the absorption spectra of simple bulk semiconductors, but show up increasingly when one considers more inhomogeneous systems. In electronic spectra of clusters (which are to be considered as a strong inhomogeneity in empty space), and for spectra involving excitations from strongly localized states [144], local field effects alone explain already most of the drastic disagreement between results obtained in the independent-transition approach, and the experimental spectra. One can hence suspect that, as already suggested by [16] and indirectly confirmed by the results of the previous chapter, local field effects play a crucial role for the description of the anisotropy of the dielectric properties of superlattices, and should not be neglected, independently of

the fact whether semi-empirical or *ab initio* approaches are used. Thus, we have decided to investigate the role of local field effects. The RPA values of the birefringence $\Delta n = \sqrt{\varepsilon}_{\perp} - \sqrt{\varepsilon}_{\parallel}$ calculated without and with local fields (respectively empty and filled squares) are reported on Fig. 5.2 as a function of the well width, together with the experimental results of Ref. [16] (filled circles). Once again, we remark that the neglect of local fields leads to an anisotropy much smaller than in the experiment. The inclusion of the off-diagonal elements in the inversion of $\varepsilon^{-1}_{G,G'}$ drastically changes the behavior of the birefringence: the amplitude increase up to the expected effective medium value $\Delta n = 0.05$, calculated with $\varepsilon_{\perp} = (\varepsilon_{GaAs} + \varepsilon_{AlAs})/2$ and $\varepsilon^{-1}_{\parallel} = (\varepsilon^{-1}_{GaAs} + \varepsilon^{-1}_{AlAs})/2$ [27]. Since any calculation of the static dielectric constant within the RPA approximation, increases the dielectric mismatch between GaAs and AlAs compared to experiment [145], the effective medium plateau calculated with theoretical dielectric constants has a higher value than the experimental one. The inclusion of local field effects perfectly reproduces the increase of the anisotropy with increasing superlattice period, which was completely absent in the independent-transition calculations. We find that, for $p > 3$, the optical anisotropy in $(\mathrm{GaAs})_p/(\mathrm{AlAs})_p$ superlattices is completely determined by the anisotropy of the local fields.

It is now interesting to analyze these results more in detail, in order to understand better the importance of local field effects. Eqs. (5.25) and (5.23) show that, indeed, χ_0 and the microscopic RPA dielectric tensor ε_{RPA} are sums over independent transitions, but the relation between the macroscopic dielectric constant and χ_0 (even in RPA) is much more complicated than the simple linear relation (5.23), that is used in calculations neglecting local field effects. The inversion (5.38) leads in fact to an effective mixing of transitions. Therefore, it is worthwhile to see, as a first step, which transitions determine the anisotropy of the dielectric response. We explore this idea by examining the effects of the highest valence and lowest conduction bands on the birefringence for the well/barrier period p=3 and p=8. In a first step we consider "all" the conduction bands (i.e. those necessary to achieve convergence) as possible final states for the transitions, but we restrict the initial states to the v first valence bands (Fig. 5.3, lower panel). Note that in order to scale the results of the three superlattices, the abscissa axis varies from lattice to lattice,

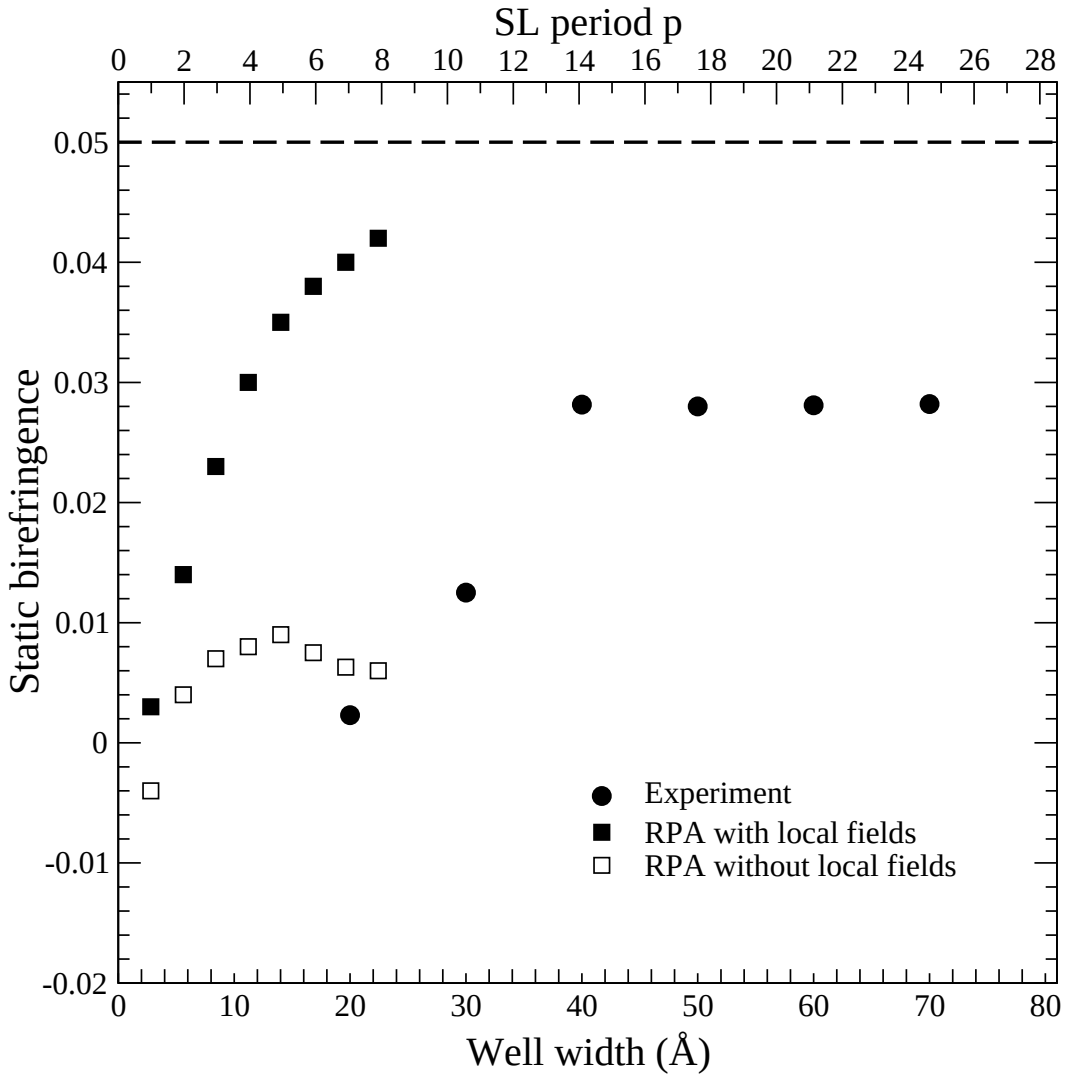

Figure 5.2: Static birefringence for $GaAs_p/AlAs_p$ superlattices as a function of p. Circle: experiment from Ref. [16]. Empty square: theoretical values without local fields. Filled square: theoretical values with local fields. The theoretical values are calculated at the average of the theoretical lattice parameters. The effective medium value calculated with the theoretical dielectric constants of bulk GaAs and AlAs is indicated by the horizontal dashed line (see text).

with $v = ip$, p being the well/barrier period and i an integer. The dependence of the birefringence on the number of valence bands included in the calculation shows the same behavior for all the studied superlattices. The bands 1 to $2p$ do not contribute to the birefringence. A large positive contribution arises from bands $4p$ to $6p$, which is almost completely canceled by the (folded) light-hole and heavy-hole bands from $6p$ to $8p$. If local field effects are neglected the cancellation is total. Also the contributions of the bands to the birefringence due to the local fields cancel, and even lead to a change in sign; the final results is dominated by the anisotropy of the local fields arising from transitions involving the top valence bands.

In a second step, we consider "all" the valence bands, and restrict final states to the c upper conduction bands as final states (Fig. 5.3, upper panel). Here the conduction band number is $c = (i-1)p + 1$, and i and p have already been defined. The highest conduction bands do not contribute to the birefringence. The high step-like positive contribution of the intermediate bands are canceled by the (folded) last conduction bands. Once again, the local fields are not important but for the bottom conduction bands. The cancellation effects are essential: in fact, a calculation involving only the highest valence and the lowest conduction bands yields a contribution of local field effects which is overestimated by about a factor 10. The observed anisotropy can hence not be explained in a simple model involving few transitions. The evolution of the top valence region is most characteristic for what is going on in this system: due to the anisotropy, to be precise the confinement in z-direction, the top valence at Γ splits into a double degenerate heavy-hole and a single light-hole state. We find that the light hole state at Γ couples to light polarized along the growth direction, whereas the heavy-hole states respond to light polarized in-plane. Of course, the order and character of the states change throughout the Brillouin zone, which prevents a simple one-to-one analysis, but, as it is also evident from Fig. 5.4, this lifting of degeneracy in the region close to the Fermi level is sufficient to explain the observed anisotropies in calculations without local field effects.

A deeper analysis of the birefringence passes through an analysis of its single components, i.e. the dielectric constant for light polarized in plane and perpendicular to the growth direction. In Fig. 5.4 the upper panel shows the results for $\epsilon_\perp$

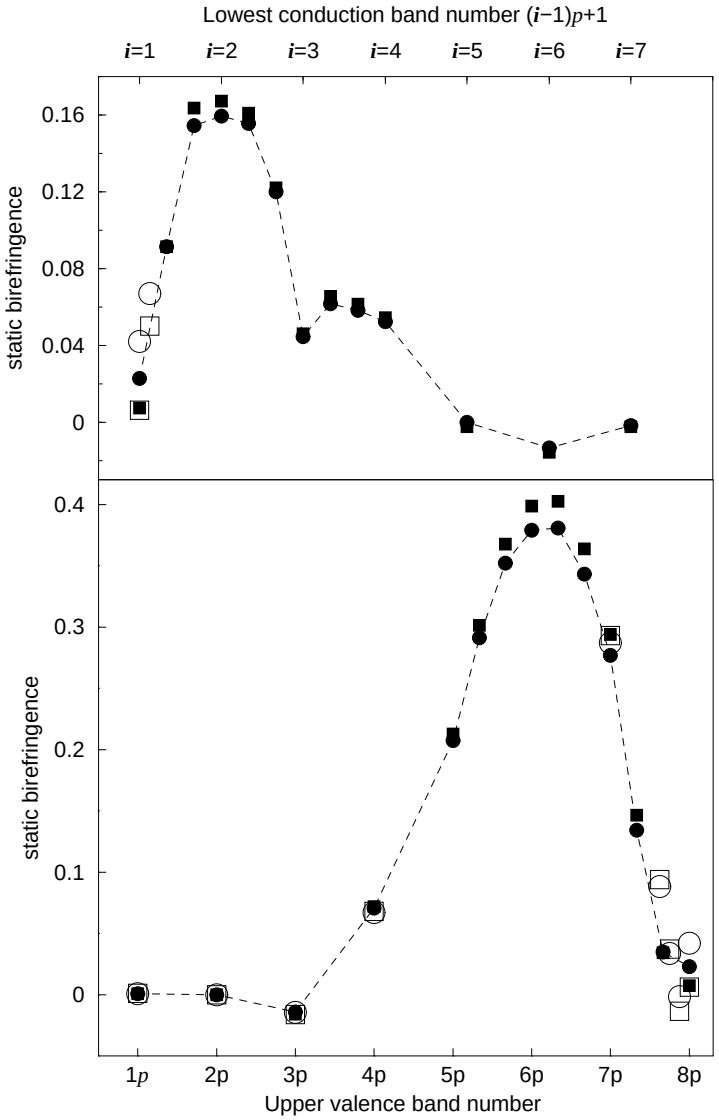

Figure 5.3: Contribution to the birefringence of the valence bands (lower panel) and of the conduction bands (upper panel) for p=3 (filled symbols) and p=8 (empty symbols). Circles: contributions with LFE; squares: contributions without LFE. The dashed line is a guide to the eyes for the p=3 SL with LFE.

and $\epsilon_{\|}$ without local field effects, the lower panel including local field effects, as a function of the superlattice period p. First, ε is essentially increasing with increasing p, which can be directly attributed to the confinement effects: the average gap between occupied and empty states decreases, due to a decrease of confinement. Second, for large superlattice periods, ε tends to the average of the bulk dielectric constants of GaAs and AlAs[145] calculated without local field effects (arrow on the upper panel of Fig. 5.4). This occurs for both polarizations, so that the birefringence tends to zero, in consistency with the fact that the weight of the contributions of the interfaces relative to the weight of the bulk states vanishes for increasing p. Third, $\varepsilon_{\perp}$ is always closer to the average value than $\varepsilon_{\|}$ for $p > 2$, which comes from the fact that the gap is smaller for light polarized in-plane than in growth direction. In other words, the confinement is rather "seen" in growth, than in in-plane direction, making the birefringence slightly positive at those p [143].

Turning to the lower panel of Fig. 5.4, which shows the same quantities calculated with local field effects, we note that as expected, local field effects decrease the absolute value of the dielectric components, because higher energy transitions are mixed in the important gap region. The decrease of ε is found to be less effective for $\varepsilon_{\perp}$ than for $\varepsilon_{\|}$. In growth direction, local field effects increase linearly with the period (see inset in Fig. 5.4), and $\varepsilon_{\|}$ is consequently always close to the effective medium value estimated with the theoretical bulk constants $\varepsilon_{\|}^{-1} = (\varepsilon_{GaAs}^{-1} + \varepsilon_{AlAs}^{-1})/2$ (dashed line) [27, 145]. In the in-plane direction however, the direct effect of quantum confinement on the independent transitions is found to be larger than its effect on the local fields. The latter are constant with the period, and the slope of of the linear behavior of $\varepsilon_{\perp}$ remains unchanged (see inset in Fig. 5.4). Consequently, the effective medium value $\varepsilon_{\perp} = (\varepsilon_{GaAs} + \varepsilon_{AlAs})/2$ (dotted line) is reached at 90% for a period as small as $p \simeq 10$. The different behaviors of $\varepsilon_{\|}$ and $\varepsilon_{\perp}$ can be understood either from the transition mixing formalism, the states coupling to light polarized in growth direction being more sensitive to the presence of an interface, or from the expression of local field effects through the matrix inversion: in fact, in the latter case it is clear that the head element of ε alone describes some average homogeneous medium. The off-diagonal elements bring the inhomogeneity into play. Now, the screening of the interaction between two charges placed at a characteristic distance

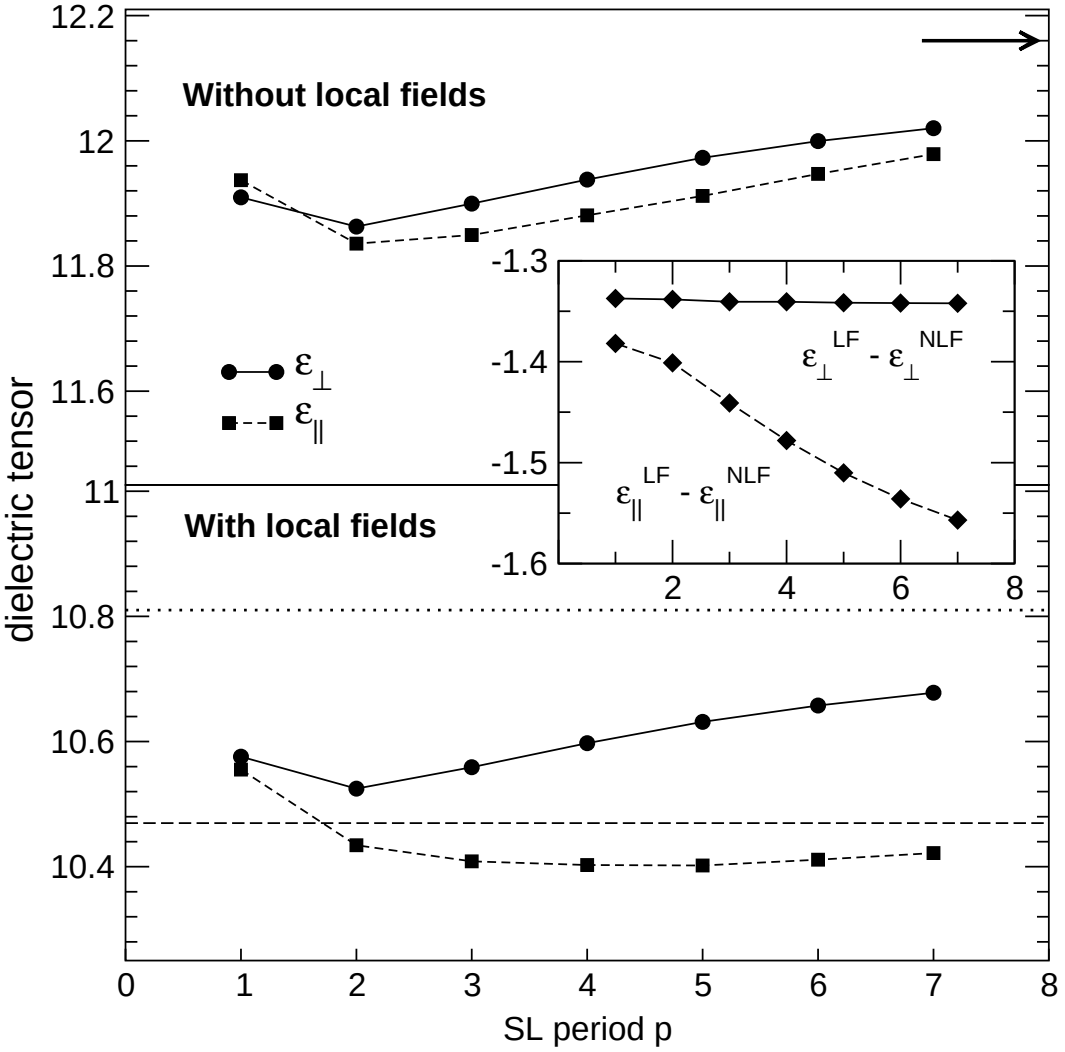

Figure 5.4: Dielectric tensor calculated without (ε^{NLF}, upper panel) and with (ε^{LF}, lower panel) LFE and their difference (inset), as a function of the SL period p. Arrow: average of bulk GaAs and AlAs dielectric constants, calculated without LFE. Dotted (dashed) line: effective medium value of $\varepsilon_\perp$ ($\varepsilon_\parallel$).

d depends only on |**d**| in a homogeneous medium, but it feels also its direction and the absolute position of the charges when the medium is inhomogeneous. When **d** is put in growth direction, the probability that the charges "see" where they are is larger than when **d** is in-plane. Thus, local field effects are stronger on $\varepsilon_{\parallel}$ than on $\varepsilon_{\perp}$. Last and most importantly, it remains to explain why local field effects increase with increasing p in growth direction (see inset in Fig. 5.4), since it is finally this fact which lets the birefringence tend to a plateau value instead of zero, as for large superlattice period the lh and hh states are again degenerate. This point can in fact be understood on the basis of the previous considerations: given a characteristic interaction length |**d**| in the system, the bigger p the bigger is the probability that the two charges are found either entirely in a region of GaAs or in a region of AlAs, instead of experiencing a screening perfectly averaged over GaAs and AlAs.

All qualitatively observed tendencies can hence be explained. It remains to be discussed what could be the origin of the remaining small quantitative discrepancies with experiment. Besides possible uncertainties coming from the transmission measurements, these might be sought on the theoretical side. Apart from various approximations like the pseudopotential approach and the neglect of spin-orbit splitting, one might suspect, first, a contribution from the geometry of the system. In fact, the band structure of bulk semiconductors has been shown to be very sensitive to a small hydrostatic pressure [98]. This change in band structure could than have significant effects on the dielectric properties. We have explored this possibility by comparing the above results, obtained using the average theoretical LDA lattice constant, with a calculation performed at the average experimental lattice constant. The latter corresponds to a negative pressure of 20 kbar in the calculation. No improvement is obtained; rather, for p=5 the birefringence has increased by 17%. There is hence some visible influence of the choice of the geometry in the calculations on the results, and, although the most straightforward guess (i.e. the ad hoc correction of the average LDA lattice constant) does not solve the problem, we cannot exclude that a geometry closer to the exact (unknown) experimental one might improve the situation. However, another point seems more crucial, namely, the inclusion of exchange-correlation effects beyond the RPA. One can do this in principle within the TDDFT scheme; in practice, calculations on realistic extended

	GaAs	AlAs
EXP	10.9	8.2
semi-empirical without local fields	10.12	7.63
RPA without local fields	14.19	10.21
RPA with local fields	12.77	8.92
LDA with local fields	13.55	9.52

Table 5.1: Experimental [43] and calculated dielectric constants for the bulk GaAs and AlAs semiconductors. We report the results of semi-empirical calculations and RPA-TDDFT calculations, both without local field effects, and the results of RPA-TDDFT and TDLDA calculations including local field effects.

systems are at the best done using the TDLDA approximation. It is known that the inclusion of the LDA xc kernel gives a minor contribution to optical absorption spectra, but a (on the scale of our problem) significant effect on dielectric constants, which might well change the birefringence. We have therefore checked this possibility by adding the exchange-correlation effects within TDLDA. In Table 5.1 we show all the calculated dielectric constants for GaAs and AlAs in comparison to the experimental values [43]. When working within the TDLDA, the bulk dielectric constants of both constituent materials increase as by much as 7 % [146]. However, those changes cancel out in the birefringence, and both the plateau value as well as the birefringence at intermediate distances remain virtually unchanged. This does not necessarily imply that exchange-correlation effects are in fact negligible. TDLDA is an approximation, and the fact that above we have related the birefringence to the near-gap transitions of the optical spectra rises the suspicion that only a theory which perfectly describes that region would be able to yield precise quantitative values for the birefringence. Such an approach does today exist for the *ab initio* calculation of optical properties, namely the simultaneous solution of the self-energy Dyson equation and the Bethe-Salpeter equation describing excitonic effects. It is of course out of reach at present to apply the full theory here.

In conclusion, concerning superlattice optical properties, we have calculated the dielectric tensor and the static birefringence of GaAs/AlAs superlattices as a function of the superlattice period. The use of an effective medium theory to describe

the dielectric tensor is found to be justified in the growth direction. In the in-plane direction, however, the direct effect of quantum confinement is large and a classical theory fails. Having learned in the previous chapter that confinement and band-mixing effects alone are not sufficient to reproduce the experimental data, we have included local field effects in present calculations. We have pointed out that quantum confinement effects are important to understand the fine structure of the optical spectra even of relatively weakly confined systems like GaAs/AlAs, but that it is completely insufficient to take them into account only via the band structure in an independent-transition picture: local-field effects, which reflect the inhomogeneity of the superlattice, effectively mix the formerly independent transitions and can therefore drastically enhance the anisotropy, up to a factor of 7 even for periods as small as $p = 8$. Moreover, we have confirmed the results of previous semi-empirical calculations based on the independent-transition scheme, by performing ab-initio calculations in the same approximation (RPA without local fields). Only by including local field effects experiments [16] can be interpreted even qualitatively. Further exchange-correlation effects seem to cancel to a large extent on the anisotropy results, and can therefore be neglected unless a fine quantitative analysis is required. Due to limitations in the computational resources, at the moment a many-body Green's function approach, which fully account for electron-electron and electron-hole interaction is out of reach. This fact calls for the search of an alternative approach to the problem and makes particularly interesting the following section, in which we are presenting an alternative way to account for many-body effects.

5.4 Effects of the long-range contribution to the xc kernel on the bulk spectra

We move now to the problem absorption spectra up to 7 eV, for bulk GaAs and AlAs systems. We want to discuss the effects of a static long-range contribution $-\alpha/q^2$ to the xc kernel f_{xc} of time dependent density functional theory. The time dependent DFT approach still keeps the advantage of the static one to be computationally very efficient, and could in principle replace other successful, but more cumbersome methods like the Bethe-Salpeter approach (BSE)[129, 147, 131, 132].

However, there are two additional difficulties with respect to the case of static DFT: (i) the approximate V_{xc} should now in principle not only be good enough to reproduce the ground state density and total energy, but the KS equation should also yield eigenvalues close to the ones that would be obtained using the unknown *exact* V_{xc} (not to be confused with the measurable quasi-particle energies) (ii) also the time-dependent density variation of V_{xc}, i.e. the so-called xc kernel $f_{xc} = \delta V_{xc}/\delta\rho$, has to be well described. Here we will mainly deal with the problem (ii). It has turned out that TDDFT yields good results using the local and adiabatic LDA approximation (TDLDA) for the xc kernel f_{xc}[128], provided that finite systems are considered. Also electron energy loss spectra of solids are well described in TDLDA. However, in both cases the main improvement with respect to the independent-particle KS spectrum (i.e. with respect to a simple sum over independent transitions between KS states) comes from the density variation of the Hartree potential (local field effects in the solid) which is described exactly, and *not* from f_{xc}. By the way of contrast, the Hartree contribution is not sufficient to yield good *absorption* spectra of *solids*, and taking into account f_{xc} within TDLDA does not lead to a significant (if at all) improvement [148]. Therefore, it would be extremely desirable to find a better, generally applicable, f_{xc}. Improvements might come through the inclusion of dynamical (memory) effects and/or long-range nonlocal terms [128, 135]. Recently, Reining *et al.* [30] have shown that a *static* long-range contribution (LRC) of the form $f_{xc}(\mathbf{q}, \mathbf{G}, \mathbf{G}', \omega) = -\delta_{\mathbf{G},\mathbf{G}'}\alpha/|\mathbf{q}+\mathbf{G}|^2$ can simulate the strong continuum exciton effect in the absorption spectrum of bulk Si ($\mathbf{q}$ is a vector in the first Brillouin zone (BZ), $\mathbf{G}$ and $\mathbf{G'}$ are reciprocal lattice vectors, and α is a material dependent parameter). Here, we discuss the effects of such a contribution more in detail, by considering also the real part of the dielectric function ε, for bulk GaAs and AlAs. Analogous results for Si and other materials are discussed in Refs. [30] and [149]. We show that the real and imaginary parts of ε at low energy are extremely well reproduced when just this long-range contribution is taken into account. It is possible to show [149] that the the approximation is not valid for the loss function, for reasons which will be discussed. We also examine the dependence of the parameter α on the material.

Before showing the results, we briefly review the origin of the long-range con-

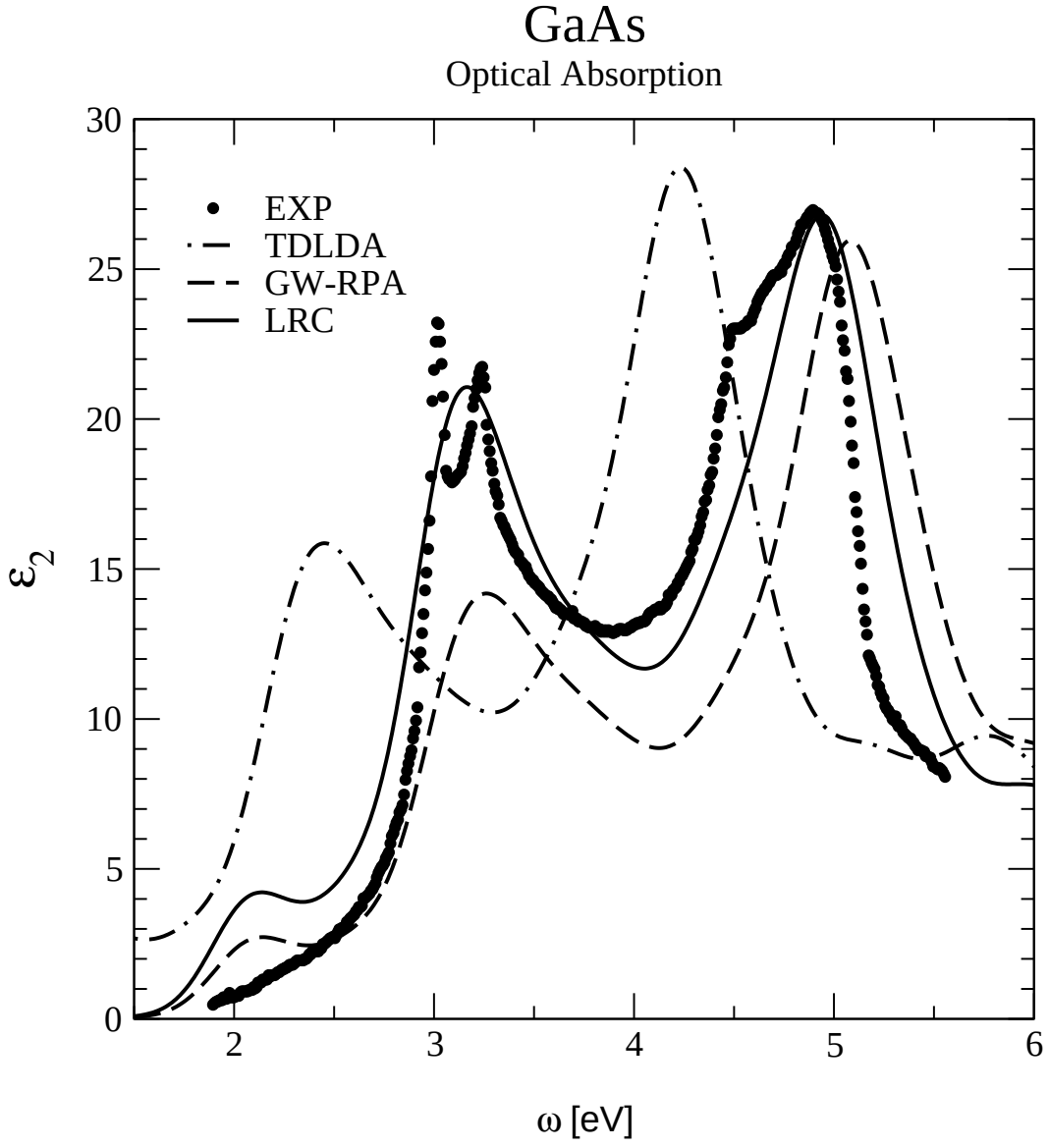

Figure 5.5: Imaginary part of the dielectric function of GaAs by *ab initio* calculations. The dots are the experimental results (Ref. [120]). The dot-dashed curve is the result of the standard TDLDA calculation, the dashed curve of the GW-RPA calculation, the continuous curve of our LRC calculation.

tribution and its implementation. In TDDFT, the inverse dielectric function of a periodic system is constructed from $\varepsilon^{-1}(\mathbf{q},\mathbf{G},\mathbf{G}') = \delta_{\mathbf{G},\mathbf{G}'} + v(\mathbf{q})_{\mathbf{G}}\chi(\mathbf{q},\mathbf{G},\mathbf{G}')$, where χ obeys the matrix equation

$$\chi = \chi_0 + \chi_0 \left(v + f_{xc}\right) \chi, \tag{5.40}$$

χ_0 being the independent-particle response function and v the bare Coulomb interaction. A similar equation can also be written for the macroscopic dielectric function which describes absorption, namely $\varepsilon_M(\mathbf{q},\mathbf{G},\mathbf{G}') = \delta_{\mathbf{G},\mathbf{G}'} - v(\mathbf{q})_{\mathbf{G}}\bar{\chi}(\mathbf{q},\mathbf{G},\mathbf{G}')$, with

$$\bar{\chi} = \chi_0 + \chi_0 \left(\bar{v} + f_{xc}\right) \bar{\chi}. \tag{5.41}$$

Here, $\bar{v}(\mathbf{q})_{\mathbf{G}}$ equals $v(\mathbf{q})_{\mathbf{G}}$ for all $\mathbf{G}$, except for the long-range term $\bar{v}(\mathbf{q})_{(G=0)}$ which is zero. Both the equations for χ and for $\bar{\chi}$ can be transformed to transition space, as it is often done for χ in the framework of quantum chemistry [136]. This allows a direct comparison to the BSE, for which this formulation is naturally adopted [129, 147, 131, 132]. One finds then that a static f_{xc} which yields the same spectrum as the BSE should be of the form

$$\begin{aligned} f_{xc}(\mathbf{q},\mathbf{G},\mathbf{G}') = & \sum_{n_1 n_2 n_3 n_4} \frac{1}{(f_{n_1} - f_{n_2})} \\ & \Phi^{-1}(n_1,n_2;\mathbf{G}) \mathcal{F}_{(n_1 n_2)(n_3 n_4)} (\Phi^*)^{-1}(n_3,n_4;\mathbf{G}'), \end{aligned} \tag{5.42}$$

with

$$\begin{aligned} \mathcal{F}_{(n_1 n_2)(n_3 n_4)} = & \left(\epsilon^{\mathrm{QP}}_{n_2} - \epsilon^{\mathrm{QP}}_{n_1} - \epsilon^{\mathrm{DFT}}_{n_2} + \epsilon^{\mathrm{DFT}}_{n_1}\right) \delta_{n_1 n_3} \delta_{n_2 n_4} \\ & + (f_{n_1} - f_{n_2}) F^{\mathrm{BSE}}_{(n_1 n_2)(n_3 n_4)} \end{aligned} \tag{5.43}$$

and

$$F^{\mathrm{BSE}}_{(n_1 n_2)(n_3 n_4)} = -\int d\mathbf{r} d\mathbf{r}' \, \Phi(n_1,n_3;\mathbf{r}) W(\mathbf{r}',\mathbf{r}) \Phi^*(n_2,n_4;\mathbf{r}'),$$

the matrices Φ being defined as

$$\Phi(n_1,n_2;\mathbf{r}) := \psi_{n_1}(\mathbf{r}) \psi^*_{n_2}(\mathbf{r}). \tag{5.44}$$

Here, f_n are occupation numbers and ϵ^{DFT} are KS eigenvalues. ϵ^{QP} are quasiparticle (QP) eigenvalues, which are supposed to be calculated within Hedin's GW approach[96]. W is the statically screened Coulomb interaction, and the ψ_n are KS

orbitals, which are assumed to be equal to the QP ones. The matrices Φ can be invertible if only a subspace of transitions is considered, which is actually the case for absorption spectra. In a solid, the pairs of indices (n_1, n_2) are to be understood as a pair of an occupied and an empty state, with $(n_1; n_2) = (v, \mathbf{k}; c, \mathbf{k}+\mathbf{q})$. $\Phi(v, \mathbf{k}, c, \mathbf{k}+\mathbf{q}; \mathbf{G} = 0)$ is going to zero as q for small q. Since $\mathcal{F}_{(v,c),(v,c)}$ in this limit behaves as a constant, this implies immediately that $f_{xc}(\mathbf{q}, \mathbf{G} = \mathbf{G}' = 0)$ behaves as $1/q^2$. There is in fact a positive long-range contribution stemming from the QP shift of eigenvalues (as also predicted in Ref. [152]), and a negative one resulting from the electron-hole interaction, which is the main point of interest here.

Comparing Eqs. (5.40) and (5.41), one can understand why the long-range contribution is much more important for absorption spectra than for the electron energy loss spectra of solids: in the former case, in Eq. (5.41) f_{xc} is added to a coulombian $\bar{v}$ which does not contain the long-range term, i.e. $v(\mathbf{G} = 0)$ is set to zero. Obviously in that case, a neglect of the divergence in f_{xc} makes an essential difference, whereas in the case of loss spectra, determined via Eq. (5.40), this argument does not hold. In order to focus the discussion about the long-range contribution on the second, i.e. the electron-hole interaction contribution, we assume in the following that we absorb the first, positive contribution in the energy shift of our starting $\chi^{(0)}$ (since anyway we do not know the eigenvalues of the exact exchange-correlation potential which would go along with the exact kernel). Furthermore, we suppose that we have a system where the long-range term is completely dominating the rest of the exchange-correlation contribution, namely, where we can approximately write $f_{xc}(\mathbf{q}, \mathbf{G}, \mathbf{G}') = -\delta_{\mathbf{G},\mathbf{G}'}\alpha/|\mathbf{q} + \mathbf{G}|^2$. This long-range approximation for the screened electron-hole interaction should of course work best for systems with weakly bound excitons. This does not mean that the excitonic effects themselves are necessarily weak, since the electron-hole interaction often drastically changes the spectral lineshape, even when the joint density of states is not affected. In fact, we will consider two materials that exhibit such a behavior, namely gallium arsenide and aluminum arsenide. We have first determined their DFT-LDA electronic structure. Second, we have constructed $\chi^{(0)}$, but with the eigenvalues shifted to approximate GW ones, in order to simulate the first part of the kernel as explained above. The GW eigenvalues are obtained by applying a scissor operator of 0.8 eV and 0.9 eV for GaAs

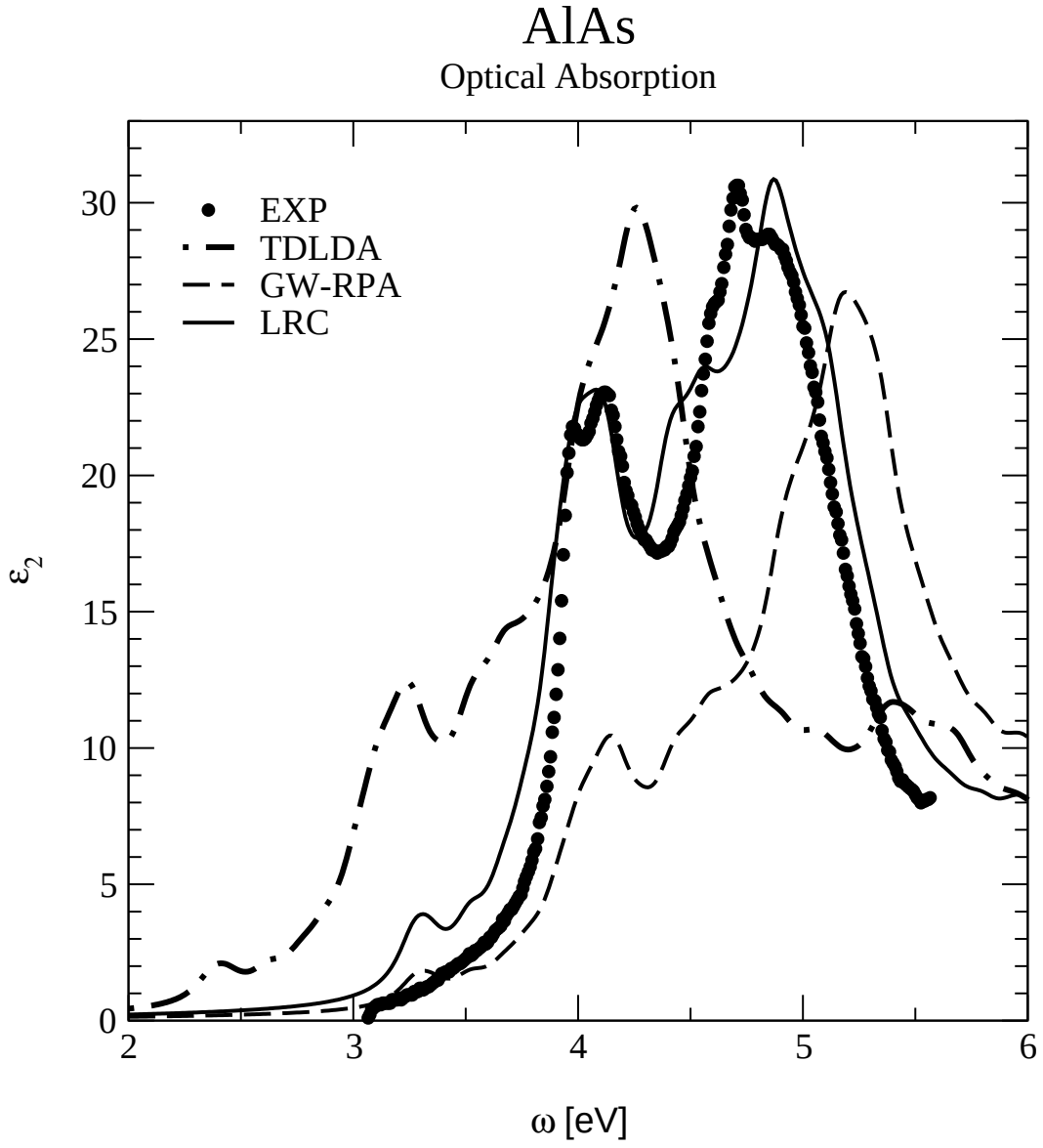

Figure 5.6: Imaginary part of the dielectric function of AlAs by *ab initio* calculations. The dots are the experimental results (Ref. [121]). The dot-dashed curve is the result of the standard TDLDA calculation, the dashed curve of the GW-RPA calculation, the continuous curve of our LRC calculation.

and AlAs [86], respectively. Third, we have used $f_{xc}(\mathbf{r},\mathbf{r}') = -\alpha/\left(4\pi|\mathbf{r}-\mathbf{r}'|\right)$, with an empirical value for α fitted to the experiment. The spectra have been obtained using 864 off-symmetry shifted k-points in the Brillouin zone.

We are ready to discuss the results. Let us first look at absorption spectra. Figs. 5.5 and 5.6 show the results for GaAs and AlAs. The dots are the experimental results (Refs. [120] and [121], respectively). The dot-dashed curve stems from a standard TDLDA calculation (i.e. using DFT-LDA eigenvalues and the static short-range LDA xc kernel). Like other authors (see e.g. [148]), we find a result close to the RPA one, showing the well-known discrepancies with experiment: peak positions are wrong (the spectrum exhibits a redshift), and the intensity of the first main structure (the E_1 peak) is strongly underestimated. The dashed curve is the result obtained by replacing KS eigenvalues with GW quasi-particle energies in the RPA form of ε. This calculation, called GW-RPA in the following, corresponds to the first step of our approach, as outlined above. Again, we find the well-known discrepancies with experiment: now the calculated spectrum shows a blueshift. Moreover, the intensity of the E_1 structure has not been corrected. Finally, the continuous curve is the result of our LRC calculation. For all three materials, a very good fit to experiment is obtained using $\alpha = 0.2$, 0.35 for GaAs and AlAs, respectively. One parameter is hence enough for each of the materials in order to correct both the peak positions and the intensities, which is far from trivial. Moreover, other features of ε are very well reproduced using the *same* α, as we will discuss in the following. The next quantity we can examine is in fact the real part of ε, $\mathrm{Re}(\varepsilon)$. Figs. 5.7 and 5.8 demonstrates the failure to reproduce the experimental results (dots) of the RPA (continuous curve), TDLDA (dot-dashed curve), and the GW-RPA (dashed curve) approaches. Again, both peak positions and line shapes are wrong. Instead, the LCR result (continuous curve) is compared to experiment: the improvement with respect to the GW-RPA situation is clear, for both materials. Alternatively, a similar agreement of both real and imaginary part of the dielectric function can only be found using the much more cumbersome BSE approach (see e.g. [147, 131, 132, 150, 151]).

We have discussed the effects of a static long-range contribution $-\alpha/q^2$ to the exchange-correlation kernel f_{xc} of TDDFT. We have shown that the real and imaginary dielectric functions of GaAs and AlAs, exhibiting a strong continuum exciton

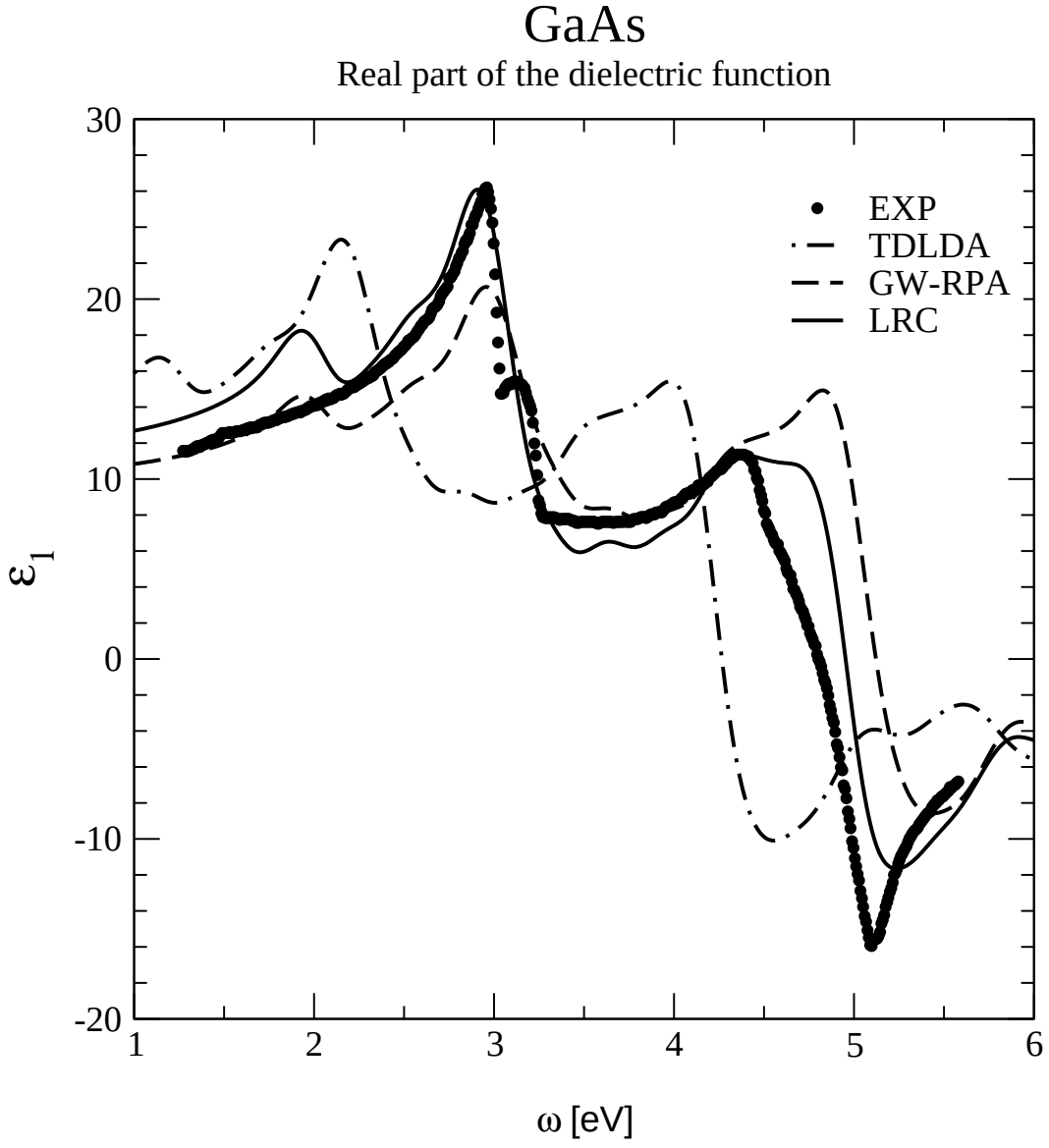

Figure 5.7: Real part of the dielectric function of GaAs by *ab initio* calculations. The dots are the experimental results (Ref. [120]). The dot-dashed curve is the result of the standard TDLDA calculation, the dashed curve of the GW-RPA calculation, the continuous curve of our LRC calculation.

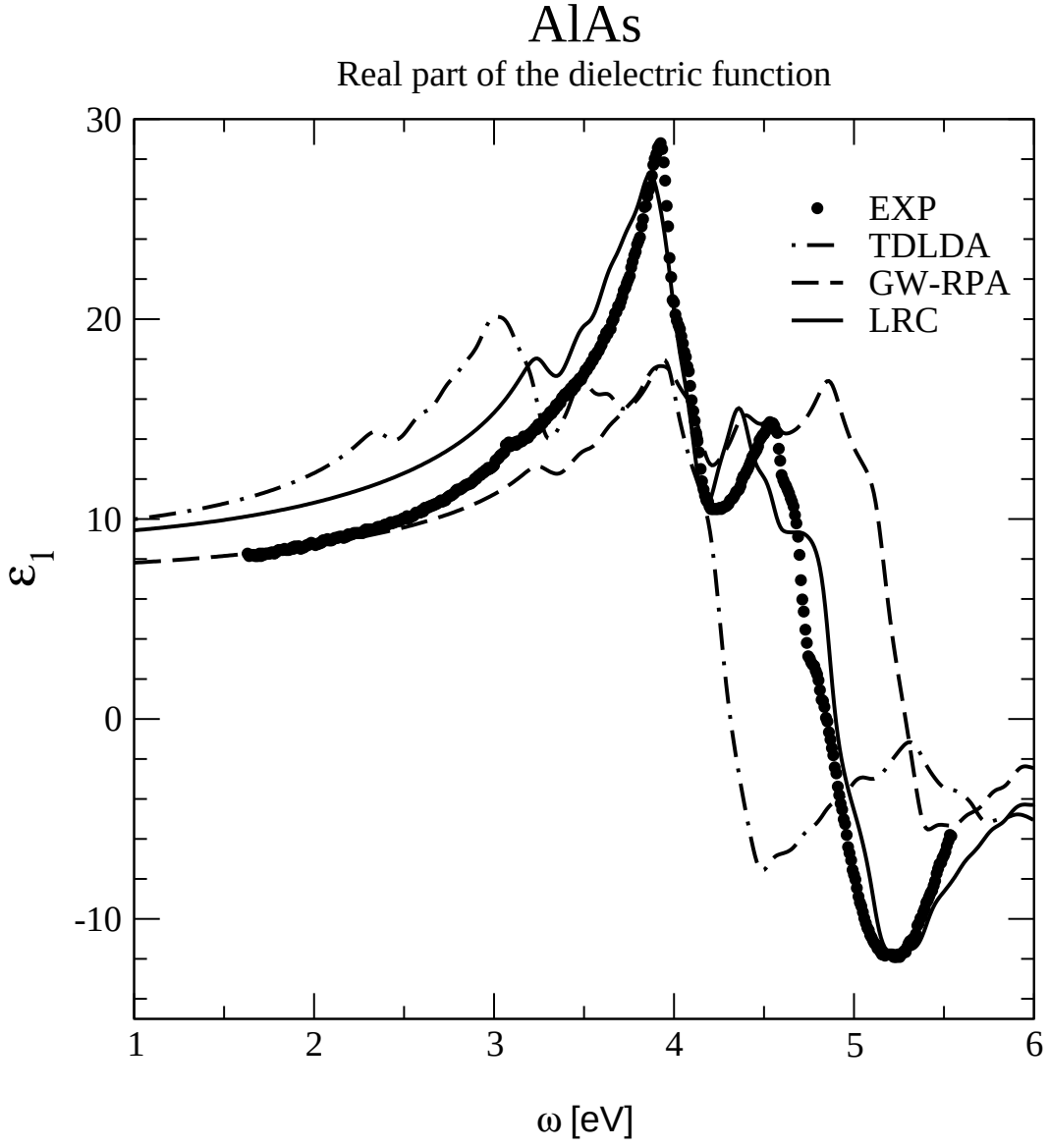

Figure 5.8: Real part of the dielectric function of AlAs by *ab initio* calculations. The dots are the experimental results (Ref. [121]). The dot-dashed curve is the result of the standard TDLDA calculation, the dashed curve of the GW-RPA calculation, the continuous curve of our LRC calculation.

effect, are considerably improved with respect to calculations where the adiabatic local density approximation is used. The findings allow to conclude that, for these materials, the problem of absorption spectra can be solved by just determining the one number α. Of course, the method is neither valid for all kind of materials, nor for all kind of excitation spectra. In spite of this, the good results for GaAs and AlAs encourage a future application of the theory to GaAs/AlAs superlattices, where it could be an alternative to the too expensive many-body Green's function formulation.

Chapter 6

Summary and discussion

Arriving at the end of this work, the easiest way to summarize the results achieved is first to go back and read the four objectives presented in the introduction, to follow then in this conclusive discussion how they have been developed in the course of the chapters.

In Chapters 2 and 4, the energy bands and optical response functions of (001)-oriented $(GaAs)_p/(AlAs)_p$ and $(GaAs)_p/(vacuum)_p$ superlattices, with p from 4 to 20, have been calculated by the LCBB method, introduced in Ref. [29]. This approach, in which the electronic states of the superlattice are expanded on the basis of bulk states, calculated by empirical pseudopotentials, is found to be adequate and practical for superlattices with intermediate to large periods; in particular, it is useful for calculating how the band structures and the optical spectra of the bulk materials are modified upon confinement.

In Chapter 2 we have studied the evolution of a bulk state into a superlattice state, gaining a clear insight on the roles played by the confinement, the bulk states-coupling and the reduction of the symmetry, all involved in the formation of a superlattice. The bulk and superlattice band structures are very similar, nevertheless there are some remarkable differences. The superlattice gaps are larger than the bulk gaps: in particular the GaAs/vacuum gaps are larger than the GaAs/AlAs ones, as a result of a stronger confinement; moreover the superlattice band gap widths increase as the superlattice period decreases. The lowering in the crystal symmetry and the mixing of the bulk states are responsible for the overall slight modification of the

energy levels and, especially, for the removal of level degeneracies.

In Chapter 4 we have addressed the optical properties. The quantum-confinement induced shifts of the critical point energies are calculated for both kinds of superlattices and are found to be larger for the GaAs/vacuum systems, where couplings between different GaAs layers are only due to quantum-mechanical tunneling and have a negligible effect. For both GaAs/AlAs and GaAs/vacuum superlattices, the E_1 peak in the absorption spectrum splits into two peaks with increasing blue shifts for decreasing superlattice period. This result agrees with the observations of Ref. [10] on GaAs/AlAs superlattices, and is attributed to a symmetry splitting of the valence bands along the line Γ-L. The E_2 transition is found to be split for large-period GaAs/AlAs superlattices, where the electronic states of the bulk are confined in each layer and the absorption spectrum is the superposition of the two bulk ones. The energy of the E_2 peak depends weakly on the superlattice period. The average (or Penn) gap does not depend on the superlattice period, confirming the expectation that a blue shift at the lower absorption edge is compensated by red shifts in the upper part of the absorption spectrum. The band contribution to linear birefringence of GaAs/AlAs superlattices is calculated and compared with recent experimental results of Ref. [16]. The zero-frequency birefringence is found to be much smaller than the experimental findings: this result hints that the missing contribution to observed static birefringence may be attributed to local-field effects, as already suggested [16]. The frequency-dependent part of the birefringence, arising from band folding and quantum confinement, increases with decreasing superlattice period, as found in the experiment, although the calculated values are smaller.

In Chapter 3 we have presented and applied the DFT-LDA to the calculation of the ground state properties and the band structures of bulk GaAs and AlAs systems and GaAs/AlAs superlattices. We have found an overall agreement with corresponding semi-empirical results, and with experimental and theoretical data available in literature. These findings confirm the analysis developed in Chapter 1 and attest the high quality of the electronic states, both semi-empirical and DFT-LDA, which are the bases of the optical absorption calculations.

In Chapter 5 we have presented two different kinds of results. First, TDDFT calculations of the dielectric tensor components and of the zero-frequency birefringence

of GaAs/AlAs superlattices as a function of the SL period, for p ranging from 1 to 8. We have shown that the use of an effective medium theory is justified in the growth direction for all periods but p=1. In the in-plane direction however, the dielectric constant $\varepsilon_\perp$ increases with increasing period, and the classical effective medium value is reached to 90% for a period as small as $p \simeq 10$. We have pointed out that the behavior of the dielectric tensor is completely determined by the interplay between quantum confinement and local fields effects, and that the birefringence comes from the anisotropy of the local fields. Quantum confinement effects are important to understand the fine structure of the optical spectra, even of relatively weakly confined systems like GaAs/AlAs, but it is completely insufficient to take them into account only via the band structure in an independent-transition picture: local-field effects, which reflect the inhomogeneity of the superlattice, effectively mix the formerly independent transitions and can therefore drastically enhance the anisotropy, up to a factor of 7 even for periods as small as $p = 8$. Including local field effects the experiment [16] can be reproduced even quantitatively. Further exchange-correlation effects seem to cancel to a large extent on the anisotropy results, and can therefore be neglected unless a fine quantitative analysis is required. Then, we have shown that, when working within the TDLDA, the bulk dielectric constants of both constituent materials increase by as much as 7 %. However, those changes cancel out in the birefringence, and both the plateau value as well as the birefringence at intermediate periods remain unchanged. In addition, we have confirmed the results of previous semi-empirical calculations based on the independent-transition scheme, for $6 \leq p \leq 8$, by performing ab initio calculations in the same approximation.

Finally, we have presented a TDDFT calculation for bulk GaAs and AlAs, which includes a static long-range contribution $-\alpha/q^2$ to the exchange-correlation kernel f_{xc}, as suggested by Reining *et al.* in Ref. [30]. We have shown that the real and imaginary parts of the dielectric function, which exhibit strong continuum exciton effects, are considerably improved with respect to calculations where the adiabatic local density approximation is used. These findings allow to state that, for these semiconductor systems, the problem of optical properties up to 10 eV could be solved by just determining the one number α. This approach has the precious advantage to reduce significantly the computation time and memory needed, in comparison

to a many-body Green's function approach. The good results for GaAs and AlAs encourage a future application of the theory to GaAs/AlAs superlattices.

The present work can be extended in several other directions. Within the LCBB scheme, relying on semi-empirical pseudopotentials, a more precise calculation of the optical properties requires the inclusion of spin-orbit interaction and local-field effects. On the other hand, a complete description of the E_1 and E_2 peaks requires, in the semi-empirical framework as well, the inclusion of excitonic effects, which account for half of the oscillator strength of the E_1 transition in the bulk. Concerning the *ab initio* approach, it is now possible to move to the study of other, more complex, superlattice systems of technological interest or even to lower-dimensional structures – quantum wires or quantum dots –, trying to clarify how the local field effects are modified and how they affect the anisotropy of the optical properties and/or investigating the role of excitonic effects, including their effect on the anisotropy of the optical response. This analysis could be applied to GaAs layers alternated with an empty lattice, which are expected to show considerably stronger confinement effects and can, in a first approach, simulate multilayer composites of GaAs and oxidized-AlAs (GaAs/AlOx) [7]. Moreover, ZnSe/GaAs could be chosen as a representative of heterovalent heterojunctions, in view of the good lattice match of the two constituent materials, and in view of its potential technological importance as a blue emitter [153]. Also Si/Ge is a system of technological interest, especially since it has been discovered that short period (i.e. less than 20 interatomic distances) Si/Ge superlattices have a quasidirect band gap due to band folding, and that the optical matrix elements between the top of the valence band and the new band edge states at the center of the Brillouin zone are enhanced by several order of magnitudes with respect to the ones for the lowest indirect transition, remaining however at least one order of magnitude smaller than the optical matrix element in a direct gap semiconductor such as GaAs [154]. Among the one-dimensional systems in which anisotropy and excitonic effects should play an important role, the study of silicon wires and gallium arsenide wires embedded in a matrix of aluminium arsenide is particularly promising. In fact, the first ones are important due to their impact on the understanding of porous silicon [155], the latter ones for their potential enhancement of the photovoltaic efficiency [156]. It would be interesting

to examine the possibility of matching the *ab initio* theory to the semi-empirical method for superlattice periods larger than $p = 8$, to extrapolate *ab initio* results on short/medium periods to qualitative or even semiquantitative predictions for larger periods. Also one and zero-dimensional systems could be studied within this approach, which would be based on the introduction of a strongly reduced basis set, given by the bulk DFT-LDA wavefunctions of the constituent materials, in analogy with the LCBB scheme.

Appendix A

Basic approximations

A solid is a many-body system (typically the number of degrees of freedom is of the order of 10^{23}), whose complete Hamiltonian consists in two terms depending respectively on the space and spin coordinates of the nuclei $\mathbf{R}_\alpha$, i.e. V_{N-N}, and on the electronic space and spin coordinates $\mathbf{r}_i$, i.e. V_{e-e}, and a term of electron-nucleus interaction, i.e. V_{N-e}:

$$H = T_e + T_N + V_{N-N}\left(\{\mathbf{R}_\alpha\}\right) + V_{N-e}\left(\{\mathbf{r}_i, \mathbf{R}_\alpha\}\right) + V_{e-e}\left(\{\mathbf{r}_i\}\right) , \tag{A.1}$$

where T_e and T_N represent the nuclear and electronic kinetic terms. Analytic solutions of the Schrödinger equation are possible for a few extremely simple systems, whereas numerical exact solutions can be calculated for a small number of atoms or molecules. In the remaining cases, we have to introduce some simplifying hypotheses. The development of schemes that provide some useful information on real systems continues nowadays. Among the variety of possible choices, and hence of different methods of calculations, the actual choice is intimately tied to the nature of the problem of interest. The aim is to make the problem feasible, without invalidating the physics of the results. We want to discuss here our specific approximations.

The inertia of a nucleus is much bigger than the inertia of an electron:

$$m_e \ll M_N , \tag{A.2}$$

in fact the mass ratio is equal to 1/2000 even in the most unfavorable case of the hydrogen atom. From a classical point of view, the velocity of a nucleus is negligible if compared to the velocity of an electron: we can state that an electron responds

almost instantly to the motion of the nuclei or, the electrons see the nuclei as if they were still. In the language of the quantum mechanics, this intuition becomes the rigorous Born-Oppenheimer approximation: after rearranging the terms, in order to isolate the electronic and ionic degrees of freedom, we write the wavefunction as a product of an electronic part $\psi(\{\mathbf{r}_i, \mathbf{R}_\alpha\})$ and a nuclear part $\Phi(\mathbf{R}_\alpha)$. If we estimate reasonable to neglect the term of interaction between the electrons and the lattice motions (i.e. the electron-phonon interaction), we obtain a Schrödinger equation where only the nuclear coordinates occur:

$$[H_N + E_e(\{\mathbf{R}_\alpha\})]\,\Phi(\mathbf{R}_\alpha) = E_T(\mathbf{R}_\alpha)\,\Phi(\mathbf{R}_\alpha)\ . \tag{A.3}$$

The presence of the electrons is included in the "adiabatic term" $E_e(\{\mathbf{R}_\alpha\})$, which express the total energy of the electrons, in case the ion cores are "frozen" in the positions $\mathbf{R}_\alpha$:

$$[T_e(\{\mathbf{r}_i\}) + V_{N-e}(\{\mathbf{r}_i, \mathbf{R}_\alpha\}) + V_{e-e}(\{\mathbf{r}_i\})]\,\psi(\{\mathbf{r}_i, \mathbf{R}_\alpha\}) = E_e(\{\mathbf{R}_\alpha\})\,\psi(\{\mathbf{r}_i, \mathbf{R}_\alpha\})\ . \tag{A.4}$$

In short, the problem can be reduced to two independent equations: first, Eq. (A.4) describes the electrons when the ions are kept in a fixed set of positions, successively Eq. (A.3) describes the lattice vibrations, considering that the ion cores feel the electrons around them thanks to the adiabatic term. Concerning the system we are interested in, the nuclei are finally located on the sites of a Bravais lattice. After the separation has been put into effect, we can concentrate on the Eq. (A.4) regarding the electronic degrees of freedom.

We will work within a pseudopotential framework (see Appendix B). When the solid is built up, the electrons which belong to internal shells in the isolated atoms (core electrons) remain strongly localized in the proximity of the nuclei, being almost not affected by the chemical bonding. This is the physical motivation to separate the core electrons from the valence electrons, by freezing them opportunely in the core ions (core electrons + nuclei).

In spite of the previous approximations, the two-body electron-electron interaction is still able to make the task formidable. We do not discuss here the big variety of remedies studied to overcome this problem. In Chapters 2 an 3 we have presented an empirical and a first-principle approach, which allow to reduce Eq. (A.4) to a

simpler effective one-particle band structure equation:

$$H_{1e}\,\phi_{\mathbf{k},n}(\mathbf{r}) = \Big(\frac{p^2}{2m} + V(\mathbf{r})\Big)\,\phi_{\mathbf{k},n}(\mathbf{r}) = E_{\mathbf{k},n}\,\phi_{\mathbf{k},n}(\mathbf{r})\,. \tag{A.5}$$

In case of a periodic crystal, the solutions of Eq. (A.5) are Bloch functions

$$\phi_{\mathbf{k},n}(\mathbf{r}) = e^{i(\mathbf{k}\cdot\mathbf{r})}u_{n,\mathbf{k}}(\mathbf{r})\,, \tag{A.6}$$

where $u_{n,\mathbf{k}}(\mathbf{r})$ has the periodicity of the Bravais lattice. The eigenstates are labelled by the band indices n and the wavevector $\mathbf{k}$, determined by the symmetry of the lattice.

Appendix B

Pseudopotentials

The concept of pseudopotentials was originally proposed in an early work of Fermi, which dates back to 1934 [157]. In regard to solids, it was introduced as a variant of the orthogonalized plane wave (OPW) method [158] and developed later in the form of empirical pseudopotentials [159, 160]. In the 80's the generalization from empirical to *ab initio* norm-conserving pseudopotentials [161, 162, 163, 164] has led to a widespread use of the method in calculations based on Density Functional Theory (DFT), allowing empirical parameter free ground state property and band structure calculations, where the only input data required are the atomic numbers of the constituent atoms.

In this appendix we give an overview of the concept of pseudopotentials, both in the empirical/semi-empirical and *ab initio* norm-conserving forms, and we discuss their construction and their use.

B.1 What a pseudopotential is

When solving the many-body problem of electrons in a condensed aggregate of atoms, a strong simplification consists in focusing on the charge density related to electrons which belong to outermost shells (valence electrons). Many difficulties come, in fact, from what happens in the inner region (core), but, fortunately, core electrons are often not concerned in the bonding together of the atoms and can be "frozen" once and for all in an atomic configuration, in order to restrict the effort to the study of the valence electrons.

The starting point is considering an isolated atom. An electron in the core region feels roughly a Coulomb-like potential, $-Z_{eff}/r$: the effective charge Z_{eff} is given by the positive nuclear charge, screened by the presence of the other electrons. An highly attractive Coulomb term $\hat{V}$ implies, from the virial theorem

$$\hat{T} = -\frac{1}{2}\hat{V}\,, \tag{B.1}$$

also a high positive kinetic energy $\hat{T}$, which reflects a strong spatial variation of the wavefunctions. This is true both for the core and the valence electrons, though the valence electrons are far less likely to reach the neighborhood of the nucleus and thus the amplitude of their oscillations is much smaller. Moreover, the waves have to interlace in order to give wavefunctions which are orthogonal to each other.

Mathematically and numerically, a plane-wave-basis formalism is one of the simplest and most natural formalism to implement in a computational code for crystals. However, it is well known that a non-smooth character of the wavefunctions in the real space correspond to a large number of plane waves to describe their Fourier transforms. When using a plane wave representation for the wavefunctions, this is a tough inconvenience, which results in a very high computational effort. A further problem comes from the fact that the energy of the core states is of the order of keV, while the relevant bonding energies are in the range of some eV: a high relative precision for total energies is needed, even if only differences are of interest. The introduction of pseudopotentials aims at finding a solution to these problems. In fact, in many systems there is a clear separation between valence and core orbitals. The core orbitals have energies far below the valence orbitals and their spatial extent is limited. In this specific case the core does not react to changes in the chemical environment and does not take part in the formation of bondings. But, in order to forget about the core electrons, it is necessary to incorporate the effects due to their presence in an effective potential, namely the *pseudopotential*, acting on the valence electrons. This pseudopotential must be built in such a way to guarantee that the solutions of the new Schrödinger equation have the same energy eigenvalues as the solutions of the all-electron problem. However, unlike the all-electron wavefunctions, the pseudowavefunctions should be smooth and nodeless. This is the essential numerical constraint when building pseudopotentials; other requirements can be added

to give all the different recipes for the different types of pseudopotentials. In fact, this is a problem whose solution is far from unique.

The core orbitals contribute to the Hartree and exchange-correlation potential felt by the valence electrons with a repulsive potential, which comes from the fact that each valence electron state ψ must be orthogonal to all the inner core electron states ψ_c. We can write:

$$\psi = \phi - \sum_c \langle \psi_c | \phi \rangle \, \psi_c \,, \tag{B.2}$$

where we introduce the pseudowavefunction ϕ. Following Phillips and Kleinman [158], substituting the Eq. (B.2) into the the Schrödinger equation for the valence electrons,

$$H \, \psi = E \, \psi \,, \tag{B.3}$$

we obtain

$$(H + V_R) \, \phi = E \phi \,, \tag{B.4}$$

where

$$V_R = \sum_c (E - E_c) \, \langle \psi_c | \phi \rangle \psi_c \tag{B.5}$$

and E_c is the energy of the core state ψ_c:

$$H \, \psi_c = E_c \, \psi_c \,. \tag{B.6}$$

The pseudopotential V^{PP} can now be defined as the sum of the original long-range attractive local potential V_I, due to the Coulomb interaction with the core ions, and the short-range repulsive potential V_R just introduced, which is a memory of the presence of the core states. The Eq. (B.4) is the wave equation for the pseudowavefunction ϕ. The resulting pseudopotential is weak and well-behaved, even inside the core radius r_c; this great simplification is obtained at the expense of introducing an energy-dependent, non-local repulsive potential.

We can exploit the symmetry of the problem to expand the pseudopotential $V^{PP}(\mathbf{r}, \mathbf{r}')$ on a set of spherical harmonic functions: it is the non-locality which leads to different components V_l^{PP} for the different angular momenta l. As all components V_l^{PP} at large r reduce to the ionic Coulomb potential, $-Z_{eff}/r$, getting independent of l, it is intuitive to write the pseudopotential as the sum of a local

potential V^{loc} and a few relevant l-dependent terms which vanish beyond r_c:

$$\langle \mathbf{r}|V^{PP}|\mathbf{r}'\rangle = V^{loc}\delta\left(\mathbf{r}-\mathbf{r}'\right) + \sum_{l=0}^{l_{max}} \sum_{m=-l}^{l} Y_{lm}^{*}\left(\Omega_{\mathbf{r}}\right) \delta V_l^{PP}\left(r\right) \frac{\delta\left(r-r'\right)}{r^2} Y_{lm}\left(\Omega_{\mathbf{r}'}\right) \ , \quad \text{(B.7)}$$

where

$$\delta V_l^{PP} = V_l^{PP} - V^{loc} \quad \text{(B.8)}$$

and Y_{lm} are spherical harmonics. Since the radial component $\delta V_l^{PP}\left(r\right)$ is local, it is more precise to call the whole pseudopotential "semi-local", instead of non-local.

B.2 Empirical pseudopotentials

The pseudopotentials can be translated in suitable fitting functions, whose parameters can be easily determined starting from reflectivity or photoelectronic spectra: this is the empirical pseudopotential method (EPM), which is by construction particularly suited to study optical properties. The pseudopotential has always the periodicity of the Bravais lattice. Assuming cells of volume Ω, which contain N_α atoms of type α, the local pseudopotential expansion as a Fourier series in the reciprocal space has the form [9]:

$$V^{loc}\left(\mathbf{r}\right) = \sum_{\mathbf{G}} v_{\alpha\mathbf{G}} S_{\alpha\mathbf{G}} e^{i\,\mathbf{G}\cdot\mathbf{r}} \ , \quad \text{(B.9)}$$

where the $\mathbf{G}$-vectors are the reciprocal lattice vectors,

$$v_{\alpha\mathbf{G}} = \frac{1}{\Omega}\int_{\Omega} V_{\alpha}^{loc}\left(\mathbf{r}\right) e^{-i\,\mathbf{G}\cdot\mathbf{r}}\, d\mathbf{r} \quad \text{(B.10)}$$

is the pseudopotential form factor for the atom α and

$$S_{\alpha\mathbf{G}} = \frac{1}{N_\alpha}\sum_{j=1}^{N_\alpha} e^{-i\,\mathbf{G}\cdot\mathbf{d}_{\alpha,j}} \quad \text{(B.11)}$$

is the structure factor, depending on the position $\mathbf{d}_{\alpha,j}$ of the j-th atom of type α in the primitive cell. The form factors are the fitting parameters. If we wish to include the effects of non-locality we should write further correction terms in the reciprocal space as a sum of l-dependent components. In the case of GaAs and AlAs bulk crystals, the inclusion of non-local terms is needed to achieve a better description of high-energy states: nevertheless, we have verified that only the lowest conduction bands are responsible for the structures in the optical spectra below

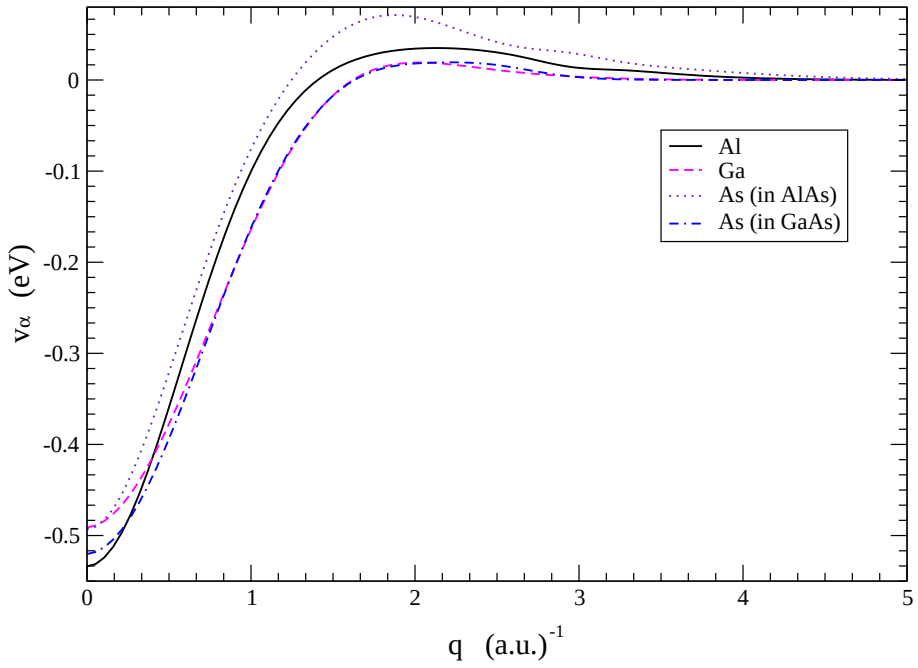

Figure B.1: Continuous atomic local pseudopotentials $v_\alpha(q)$ calculated following Mäder and Zunger [44].

6 eV and therefore non-local terms can be neglected for our purposes. The first atomic pseudopotentials were developed in this way more than 30 years ago. Although extremely easy to use, these pseudopotentials were not always adequate to well reproduce the wavefunctions and their related quantities. Moreover, it did not exist a reliable procedure to assure the transferability to different crystal structures or different coordination numbers. In the last decade the request for more accurate atomic empirical pseudopotentials, to be used in the field of nanostructures calculations, has grown. In particular, it is no more desirable the solution to have different sets of form factors for different supercell dimensions. Let us clarify the statement using as example the superlattices GaAs/AlAs studied in this work: the number of **G**-points of the superlattice reciprocal lattice, lying between two reciprocal lattice points of the bulk crystal, grows linearly with the superlattice period p. As a consequence, to study large systems, we need to know the value of $v^\alpha_{\mathbf{q}}$ at a dense grid

of points $\mathbf{q}$, which define the superlattice reciprocal lattice $\mathbf{G}_{SL}$. To this aim, it is useful to develop a continuous-space empirical pseudopotential $v_\alpha(\mathbf{q})$,

$$v_\alpha(q) = \frac{1}{\Omega} \int_\Omega d\mathbf{r}\, e^{i\mathbf{q}\cdot\mathbf{r}}\, v_\alpha(\mathbf{r})\,, \tag{B.12}$$

to be used for all the possible different structures based on the same constituents, including of course the bulk crystals (see Chapter 2). That is exactly what Zunger *et al.* have done for different semiconductor compounds, starting from 1994 [44, 165, 166, 167, 168].

Concerning GaAs and AlAs crystals, we refer to the semi-empirical pseudopotential functions proposed in Ref. [44]. We define them "semi-empirical" because the fitting takes into account not only experiment, but also *ab initio* calculations. The procedure adopted to evaluate the function (B.12) consists in the following operations:

1. The origin of the zinc-blend primitive cell is fixed in the middle of the line between the anion (As) and the cation (Ga or Al).

2. The bulk form factors $v_\alpha(G)$ are adjusted at a small number of reciprocal lattice vectors $\mathbf{G}$ to reproduce bulk band energies and effective masses. The operation is repeated at different unit cell volumes Ω, to gain informations on the neighborhood of each point $\mathbf{G}$ and dispose of a finer mesh which will make the interpolation less ambiguous. By inspecting the discrete form factors the algebraic form selected for the fitting is a linear combination of Gaussians, multiplied by a smooth function that allows adjustments of the small q components:

$$v_\alpha(q) = \frac{\Omega_\alpha}{\Omega} \sum_{i=1}^{4} a_{i\alpha}\, e^{-c_{i\alpha}(q-b_{i\alpha})^2} \left[1 + f_{0\alpha} e^{-\beta_\alpha q^2}\right]. \tag{B.13}$$

3. At this stage the parameters of Eq. (B.13) are let free to vary independently (the original form factors may change), to fit: (i) the experimental GaAs/AlAs valence band offset (0.5 eV), (ii) LDA calculated level splittings in short-period GaAs/AlAs superlattices of various orientations, (iii) first-principle LDA wavefunctions. In this way, it is possible to explore the region $q < \frac{2\sqrt{3}\pi}{a}$, where a is the lattice constant: small q form factors are so fitted, rather than extrapolated. Moreover, the above mentioned problem of previous empirical calculation which yielded poor wavefunctions is finally solved.

$\Omega\alpha$ $(a.u.)^3$	$a_{i\alpha}$ Ry	$b_{i\alpha}$ $(a.u.)^{-1}$	$c_{i\alpha}$ $(a.u)^2$
Al			
111.3	-1.32712	0	1.59819
	0.158114	1.77453	2.10827
	0.0601648	2.59550	0.527745
	0.0168167	2.93581	11.2708
Ga			
131.4	-1.24498	0	1.52748
	0.0366517	2.09782	0.959082
	0.0464357	2.01935	0.574047
	-0.0133385	2.93581	11.2708
As (in AlAs)			
145.2	-1.10411	0	0.972439
	0.0174946	2.46793	6.53147
	-0.00368081	1.22845	5.50601
	0.0921512	1.35897	1.18638
As (in GaAs)			
145.2	-1.05821	0	0.959327
	-0.00217627	2.46808	6.53145
	-0.0434312	0.851644	2.94679
	0.10569	1.22436	0.820922

Table B.1: Atomic pseudopotential parameters in Rydberg units, and volumes Ω_α in atomic units. [44]. The four rows for each atom correspond to the four Gaussian functions ($i = 1, 2, 3, 4$) in Eq. (B.13). We further need to define: $f_{0Al} = 0.02$, $\beta_{Al} = 10\,(au)^{-1}$, and $f_{0Ga} = f_{0As} = 0$. These pseudopotentials are designed for a kinetic-energy cutoff of 5 Ry.

4. The As potential in GaAs and AlAs are not constrained to be identical, i.e. they are fitted independently, to account for the local-environment dependence of the atomic potential, by considering the local electronic charge. This is equivalent to say that empirical/semi-empirical pseudopotentials are not transferable to different chemical environments. The pseudopotential for As coordinated by n Al atoms and $(4-n)$ Ga atoms is given by the weighted average:

$$v_{As} = \frac{n}{4}\, v_{As}\left(\mathrm{AlAs}\right) + \frac{4-n}{4}\, v_{As}\left(\mathrm{GaAs}\right) . \tag{B.14}$$

   This means that, to preserve a correct description of interfaces in GaAs/AlAs superlattices, an As atom bound to two Al and two Ga atoms is attributed a symmetrized pseudopotential, which is the average of the As pseudopotential functions in GaAs and AlAs environments.

5. The quality of the final pseudopotentials is widely tested, in the contest of plane-wave calculations in Ref. [44], in the contest of LCBB calculations in Ref. [29].

These pseudopotentials are local and, at this stage, do not include spin-orbit terms, even if in the Appendix of Ref. [44] it is suggested how to include them. Bulk and superlattice energy levels are provided in the same absolute energy scale, thus superlattice and bulk eigenvalues can be easily compared and the valence band offset is automatically reproduced. The different $q \longrightarrow 0$ limit values of $v_\alpha(q)$ are the key-points to describe correctly the band alignment. The optimized parameters of Eq. (B.13) are given in Table B.1. The energy cutoff these pseudopotentials are designed for is 5 Ry. At last, we should add that the continuous pseudopotentials presented here are not the only ones in literature. Nevertheless, trusting the comparison table in Ref. [44], these pseudopotentials should be the more efficient, at least for a superlattice constituted by GaAs and AlAs. Our results, both concerning the bulk and superlattice systems, confirm the high quality of these pseudopotentials.

B.3 Ab-initio pseudopotentials

B.3.1 Hamann pseudopotentials

In a full DFT calculation, including explicitly both core and valence electrons, the valence electrons feel potentials due to the nuclei, the core electrons and the other valence electrons. The sum of the first two terms gives the true ionic potential. Within a pseudopotential framework, the true ionic potentials are substituted by the ionic pseudopotentials: the two potentials differ in a spherical region centered on the nuclei. We can already underline a basic difference between this definition of pseudopotentials and the semi-empirical pseudopotentials presented in the last section: the semi-empirical pseudopotentials are screened, i.e. they include also the effects due to the electron-electron interaction between valence electrons. This explains, as we have already remarked, why empirical/semi-empirical pseudopotentials cannot be transferable. In case of ionic pseudopotentials we do not meet this restriction: it is practical to have a pseudopotential, which can be convenient to describe the electronic properties in deeply different chemical environments, like an excited atomic state, a molecule or a solid.

The formulation of modern *ab initio* pseudopotentials goes beyond the Phillips-Kleinman scheme, overcoming some problems arising from the imperfect normalization of the pseudowavefunction. In fact, if the true wavefunction ψ is normalized to one, then from the (B.2):

$$1 = \langle\phi|\phi\rangle - 2\sum_c \langle\psi_c|\phi\rangle\langle\phi|\psi_c\rangle + \sum_c |\langle\psi_c|\phi\rangle\ |^2\ ; \tag{B.15}$$

it follows that the pseudowavefunction ϕ has a norm only approximatively equal to one:

$$\langle\phi|\phi\rangle = 1 + \sum_c |\langle\psi_c|\phi\rangle\ |^2\,. \tag{B.16}$$

This is a consequence of the incorrect distribution of the valence charge between the core and the valence region and would cause serious problems in self-consistent calculations. This inconvenience is eliminated in the formulation of Hamann, Schlüter and Chiang [161], by imposing the conservation of the norm for the pseudowavefunction. In the framework of this formalism, Bachelet, Hamann and Schlüter have built systematically all the atomic norm-conserving pseudopotential from H to Pu

[162]. This is not the only way to solve the problem, another possible way leads to the soft non-norm-conserving pseudopotentials of Vanderbilt [169].

The construction of the Hamann pseudopotentials starts from an All-Electron (AE) calculation, within density functional theory, for the isolated atom. The goal is to build a soft potential without a singularity in the origin, nevertheless the new potential must not change the physical properties of the system. The procedure can be summarized in the following steps:

a) the Kohn-Sham equation for the radial part R_{nl}^{AE} of the atomic wavefunction is solved self-consistently within an all-electron scheme:

$$\left\{-\frac{1}{2}\frac{d^2}{dr^2}+\frac{l\,(l+1)}{2r^2}+V^{AE}\,[n;r]\right\} r\,R_{nl}^{AE}\,(r)=\epsilon_{nl}^{AE} r\,R_{nl}^{AE}\,(r)\;, \tag{B.17}$$

where

$$V^{AE}\,[n;r]=-\frac{Z}{r}+V_H\,[n;r]+V_{xc}^{LDA}\,(n(r))\;, \tag{B.18}$$

Z is the atomic number, $V_H\,[n;r]$ is the Hartree potential and $V_{xc}^{LDA}\,(n(r))$ is the exchange-correlation potential in the local density approximation.

b) The all-electron radial wavefunctions R_{nl}^{AE} is modified, by making it smooth and nodeless in the core region, to obtain the radial pseudowavefunction R_{nl}^{PP}. The pseudowavefunction R_{nl}^{PP} must fulfill the pseudoatom Kohn-Sham equation,

$$\left\{-\frac{1}{2}\frac{d^2}{dr^2}+\frac{l\,(l+1)}{2r^2}+V_l^{PP}\,[n;r]\right\} r\,R_{nl}^{PP}\,(r)=\epsilon_{nl}^{PP} r\,R_{nl}^{PP}\,(r)\;, \tag{B.19}$$

To be more precise, the pseudowavefunctions R_{nl}^{PP} are built, under the constraint to fulfill the following requirements:

(i) For the same atomic configuration, the valence eigenvalues of the all-electron Hamiltonian and the pseudo-Hamiltonian must be equal:

$$\epsilon_{nl}^{AE}=\epsilon_{nl}^{PP}\,. \tag{B.20}$$

(ii) The pseudowavefunction $R_{nl}^{PP}\,(r)$ must coincide with $R_{nl}^{AE}\,(r)$ outside the core region, i.e.

$$R_{nl}^{AE}\,(r)=R_{nl}^{PP}\,(r)\;, \tag{B.21}$$

for r beyond a cutoff distance called core radius r_{cl}, which depends on the angular momentum component l. The core radius r_{cl} must include the more external node of the l-th component of the all-electron wavefunction.

(iii) The integral

$$\int_0^R \left| R_{nl}^{AE,PP}(r) \right|^2 r^2 dr \,, \tag{B.22}$$

with $R > r_c l$, must give the same value for an all-electron wavefunction and a pseudowavefunction: this relation expresses the conservation of the norm. From the Eq. (B.22) it follows, thanks to the Gauss theorem, that the electrostatic potential produced at distances $r > r_c$ by the pseudo-charge distribution is equal to the potential produced by the true charge distribution. The density functional theory is based on the concept of charge density, thus it is fundamental to reproduce correctly the true charge density of the system.

(iv) The logarithmic derivatives of the true wavefunction and the pseudowavefunction and their first derivatives with respect to the energy must converge to the same values for $R > r_c$:

$$\frac{1}{R_{nl}^{PP}(r,\epsilon)} \frac{dR_{nl}^{PP}(r,\epsilon)}{dr} = \frac{1}{R_{nl}^{AE}(r,\epsilon)} \frac{dR_{nl}^{AE}(r,\epsilon)}{dr} \,. \tag{B.23}$$

For a perfect pseudopotential Eq. (B.23) holds for every energy ϵ, not only for the eigenvalues ϵ_{nl}. This equality comes from the theory of scattering and, together with the point (iii), it is essential to guarantee the transferability of the atomic pseudopotential to different chemical environments.

The freedom left within the construction rules still allows to play with the parameters to get a "soft" pseudopotential, i.e. a pseudopotential which leads to a low cutoff energy for the plane-wave basis.

c) Once we have obtained the pseudowavefunction, the pseudopotential is obtained by the inversion of the Eq. (B.19):

$$V_{scr,l}^{PP}(r) = \epsilon_{nl} - \frac{l(l+1)}{2r^2} + \frac{1}{2rR_{nl}^{PP}(r)} \frac{d^2}{dr^2} \left[r R_{nl}^{PP}(r) \right] \,. \tag{B.24}$$

For a nodeless wavefunction the pseudopotential does not have any singularity, except possibly at the origin, where it can be avoided by imposing the wavefunction to be proportional to r^l, when it is approaching the origin.

d) At this stage, the pseudopotential is screened, i.e. it contains the Hartree and exchange-correlation potentials due to valence electrons. In this form, it is not

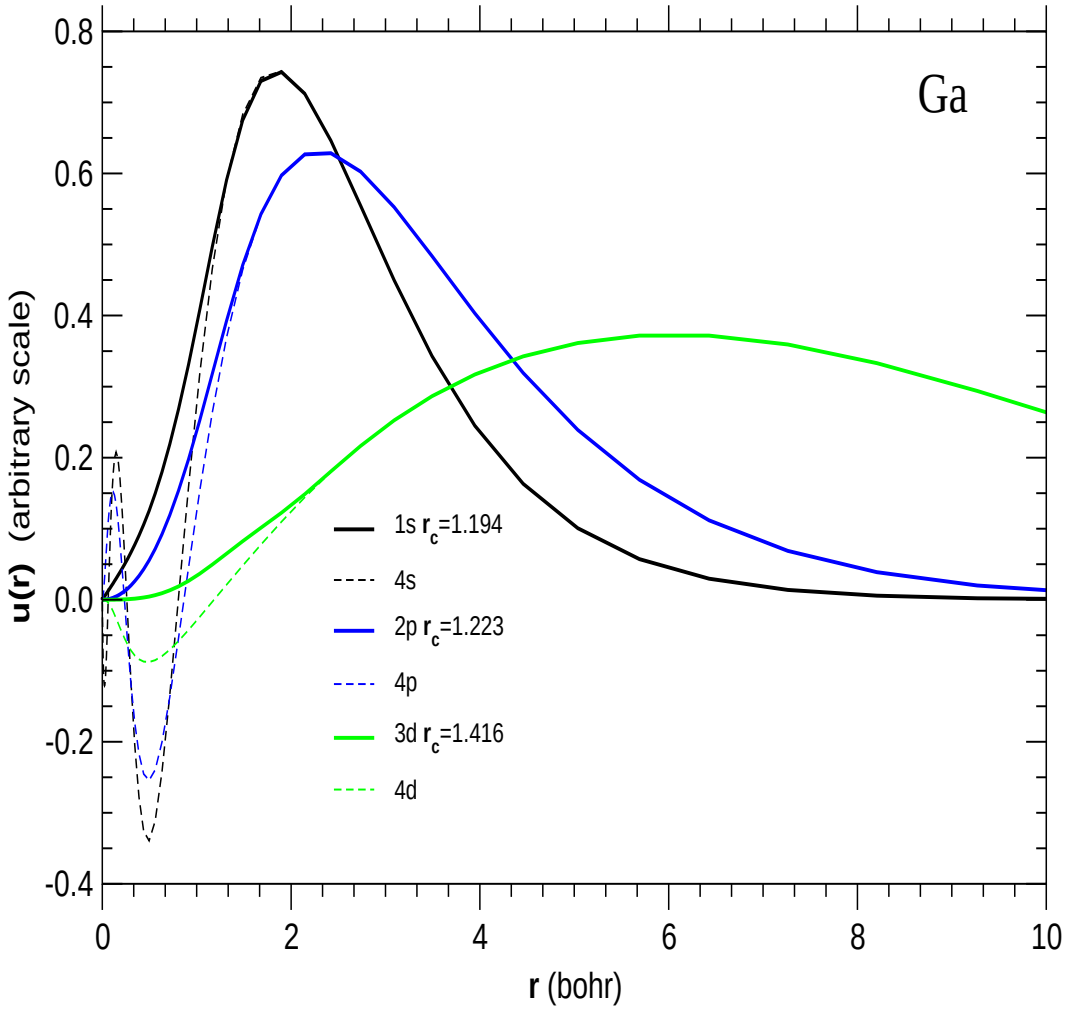

Figure B.2: Example of Ga: the all-electron wavefunctions compared to the pseudowavefunctions for valence states: they differ only inside the core radius.

suitable to be used in a chemical environment which differs from the one in which it has been generated. We need to remove the screening of the valence electrons. Although the exchange-correlation energy is a non-linear functional of the total electron density, in practice the "linearization" of the core-valence contribution is usual and often adequate [170]. An explicit account of the core-valence non-linearity of V_{xc} (non-linear core correction) [171] is sometimes necessary, in particular if the overlap between the core and valence density is remarkable. Anyway, whatever approximation has been chosen, the goal is to subtract from the pseudopotential the contributions to the Hartree potential and the exchange-correlation potential due to the valence electrons:

$$V_{ion,l}^{PP}(r) = V_{scr,l}^{PP}(r) - V_H[n_v; r] - V_{xc}[n_v; r] \ . \tag{B.25}$$

As a consequence of the process of construction of the "bare" pseudopotential, we have a final result which depends explicitly on the components of the angular momentum l :

$$V_{ion}^{PP}(r, r') = \sum_{l=0}^{\infty} \hat{P}_l \delta(r - r') V_{ion,l}^{PP}(r) \ , \tag{B.26}$$

where $\hat{P}_l$ is the projector on the l-th eigenstate of the angular momentum. We underline that the pseudopotential is local in the radial variables, but non-local as far as angular coordinates are concerned: this kind of behavior characterized a semi-local pseudopotential.

e) In the final formulation it is useful to separate a local long-range term from the non-local short-range l-dependent terms:

$$V_{ion}^{PP}(r, r') := V_{loc}^{PP}(r) + \Delta V_l^{PP}(r, r') = V_{loc}^{PP} + \sum_{l=0}^{\inf} |l\rangle \Delta V_l^{PP} \langle l| \, . \tag{B.27}$$

A typical choice is to set V_{loc} equal to one of the non-local components: the local component can, in principle, be arbitrarily chosen, but since the summation in Eq. (B.27) will need to be truncated at some value of l, the local potential should be chosen such that it adequately reproduces the atomic scattering for all the higher angular momentum channels. The maximum angular momentum l_{max} depends both on the atom and on the electronic environment in which it lies. In fact, in the solid the atomic electronic charge is redistributed and may be in an

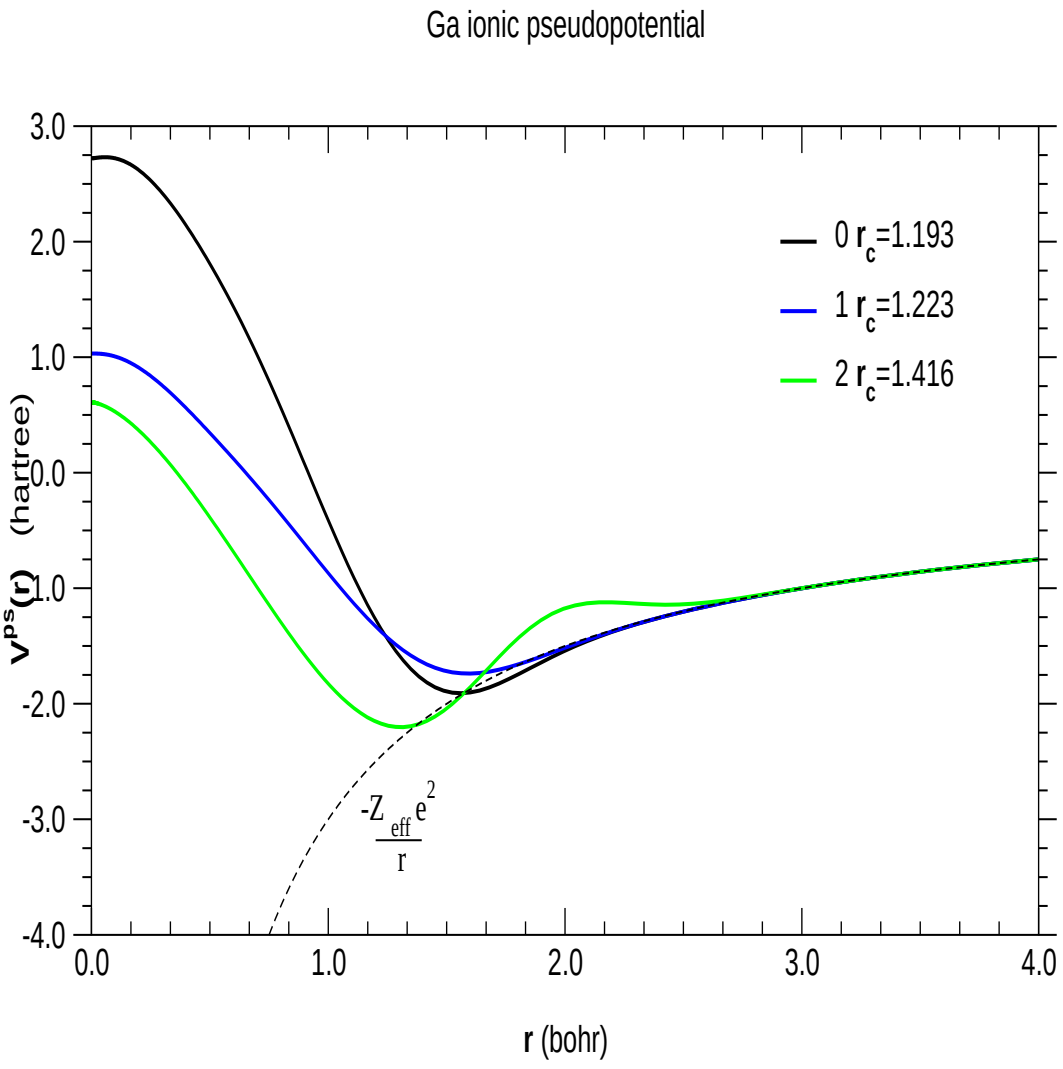

Figure B.3: Example of Ga: the ionic pseudopotential components for angular momenta $l = 0, 1,$ and 2. The dashed line denotes the Coulomb potential for a point-like atomic core.

excited state if compared to the atomic ground state. For the construction of excited angular momentum components it is necessary to rearrange the valence charge into excited orbitals, maybe even in a ionic configuration. In Figs. B.3 and B.2 we show an example of the application of the Hamann scheme: the non-local components of the pseudopotential of Ga are presented in Fig. B.3 on page 148, together with the ionic Coulomb potential. In Fig. B.2 on page 146 we show how the the wiggles in the valence states of Ga are eliminated, moving from the real wavefunction to the pseudowavefunction.

The transferability and the smoothness of the pseudopotential are both strongly affected by the choice of the core radius r_{cl}. A high radius reduces the influence of the oscillating core states and brings to a softer pseudopotential, which leads in its turn to a smaller energy cutoff of the plane-wave basis. On the other hand, the transferability is lowered, due to the loss of physical relevant information in the core region. For each atom the appropriate cutoff radius must be selected as a compromise between fast convergence and good transferability. There are practical limits on how far r_{cl} can be decreased: it must be larger than the outermost node of the all-electron wavefunction; on the other hand it must be small enough to prevent overlaps of neighboring core regions when the molecule or the solid is created. Concerning the energy cutoff of the plane wave basis, certain natural restrictions occur: the atomic size imposes a length scale to the problem, which influences the extent of the Fourier expansion needed to accurately describe the pseudowavefunction. Anyway, a soft pseudopotential prevents from wasting computational effort in unnecessarily large expansions. The transferability depends critically also on the linearization of the core-valence-exchange-correlation and, of course, on the choice of the states to be included in the core. At last, another worsening to the transferability properties can come from the transformation of the pseudopotential from the semi-local into the fully separable form. We will discuss this step in a following section.

The comparison between the logarithmic derivative in an all-electron or pseudopotential calculation, as already mentioned, gives clear hints on the transferability of the generated pseudopotentials. An additional quality requirement

is the check that the all-electron atomic excitation or ionization energies and the eigenvalues are close to the energy values obtained from the pseudopotential calculations and the all-electron frozen core calculations. According to this test, a transferable pseudopotential should lead to the same accuracy as the frozen-core all-electron calculation. Anyway, a final insight on the quality of the pseudopotential can only be given by the results of realistic calculations on different model systems (molecules or solids): the criterion is that a pseudopotential and an all-electron calculation must deliver the same valence electronic structure and the same total energy differences.

B.3.2 Troullier and Martins pseudopotentials

The prescriptions given in the previous section are not sufficient to define uniquely a pseudopotential. It may be remarked that the smoothness of the pseudopotential has never been explicitly required. It has been the objective of much active work trying to determine some practical atomic criteria for a computational efficient pseudopotential, which reproduces the correct all-electron behavior outside the core region. Kerker [172] was the first to propose a pseudopotential construction which focused on the smoothness of the pseudowavefunction. Troullier and Martins [163] generalized and improved Kerker's method, obtaining smooth pseudopotentials with a relatively high cutoff radius, but still able to preserve good logarithmic derivatives. Their recipe has proved to be particularly efficient for systems containing first row elements, transition metals, and rare-earth elements. The first row elements, for example, contain no p core electrons, thus their pseudopotential components with p symmetry are very strong, because there are no inner p states to enforce the orthogonality. Transition metals and rare-earth elements have similar problems with d and f components. Calculations involving atoms of the above type are particularly demanding and these atoms provide an important test for pseudopotential smoothness. The procedure of Troullier and Martins consists in modeling inside the core radius the radial wavefunction in the form:

$$R_{nl}^{PP}(r) = r^{l} e^{p_l\left(r^2\right)}, \tag{B.28}$$

where p_l is a polynomial of order six in r^2. The seven variational coefficients of the polynomial are chosen to fulfill the seven following conditions:

(i) Norm-conservation of charge within the core radius r_{cl}, like in the Hamann recipe.

(ii)-(vi) The continuity of the pseudopotential wavefunction and its first four derivatives at r_{cl}, which imposes in effect the continuity of $V_{scr,l}^{PP}(r)$ and its first two derivatives at r_{cl}.

(vii) The zero curvature of the screened pseudopotential at the origin: $V_{scr,l}^{\prime PP}(0) = 0$.

The last point is the criterion to give smooth pseudopotentials. This condition has been accurately tested in Ref. [163]. Once the pseudowavefunction has been defined, the procedure which leads to the pseudopotential is the standard method described in the previous section. Although there are still no absolute criteria for efficient pseudopotentials, the recipe by Troullier and Martins has been proven to deliver excellent pseudopotentials, offering high transferability in combination with fast convergence.

B.3.3 Kleinman-Bylander formulation

Working on a plane-wave representation entails performing some calculations in the position space and some others in the momentum space, passing from one space to the other thanks to a Fourier transform. In the reciprocal space the semi-local part of the pseudopotential is described by the expression:

$$\sum_{\mathbf{G},\mathbf{G}'} |\mathbf{k}+\mathbf{G}\rangle \Delta V_l^{PP}(\mathbf{k}+\mathbf{G},\mathbf{k}+\mathbf{G}') \langle \mathbf{k}+\mathbf{G}'|\,, \tag{B.29}$$

which is completely non-local.

For an N-dimensional basis $\{\mathbf{G}\}$, the semi-local form requires the evaluation and storage of $(N^2+N)/2$ matrix elements $\langle \mathbf{k}+\mathbf{G}|\Delta V_l^{PP}|\mathbf{k}+\mathbf{G}'\rangle$. Kleinman and Bylander (KB) [173] found out that by complicating the expression of the pseudopotential in real space, it is possible to save time and memory in their manipulation in reciprocal space. With the KB form the matrix elements of the non-local pseudopotential between two states $|\mathbf{k}+\mathbf{G}\rangle$ and $|\mathbf{k}+\mathbf{G}'\rangle$ are expressed as the product of two factors, requiring only a number proportional to N of projections $\langle \Delta V_l^{PP}\phi_{lm}^{PP}|\mathbf{k}+\mathbf{G}\rangle$

and then simple multiplications. In fact, following Kleinman and Bylander, we can rewrite in their separable form the non-local pseudopotential components:

$$\Delta V_l^{KB} = \sum_{l,m} \frac{|\Delta V_l^{PP}\phi_{lm}^{PP}\rangle\langle\Delta V_l^{PP}\phi_{lm}^{PP}|}{\langle\phi_{lm}^{PP}|\Delta V_l^{PP}|\phi_{lm}^{PP}\rangle}\,, \tag{B.30}$$

where ϕ_{lm}^{PP} are the pseudoeigenfunctions of the Hamiltonian, obtained from the semi-local atomic pseudopotential. The Fourier transform of Eq. (B.30) is:

$$\sum_{lm} \frac{\left[\sum_{\mathbf{G}} |\mathbf{k}+\mathbf{G}\rangle\langle\mathbf{k}+\mathbf{G}|\Delta V_l^{PP}\phi_{lm}^{PP}\rangle\right]\left[\sum_{\mathbf{G}'} \langle\Delta V_l^{PP}\phi_{lm}^{PP}|\mathbf{k}+\mathbf{G}'\rangle\langle\mathbf{k}+\mathbf{G}'|\right]}{\langle\phi_{lm}^{PP}|\Delta V_l^{PP}|\phi_{lm}^{PP}\rangle}\,. \tag{B.31}$$

Of course, if we use the non-local part of the pseudopotential, as written in expression (B.30), to solve the electronic problem of the atom, we find the same eigenvalues and eigenvectors we had already found with the pseudopotential expressed in the semi-local form. This occurrence makes the KB pseudopotential in principle as valid as the corresponding semi-local pseudopotential. Nevertheless, this procedure has to be applied cautiously, because it can modify in a non-physical way the chemical properties of the atoms. The problem, as explained in Ref. [174], comes from the fact that the KB Hamiltonian does not respect the Wronskian theorem [175]. According to the theorem, the atomic eigenfunctions are energetically ordered such that, for a given quantum number l, the energies increase with the number of nodes. Since this condition does not hold for the KB Hamiltonian, "ghost" states. i.e. unphysical solutions, can show up in the chemically important energy range around the valence eigenvalues E_l. There are some practical prescriptions to distinguish and eliminate the ghost states : besides applying the criterion of Gonze *et al.* [174], the logarithmic derivatives as a function of the energy must be accurately inspected, comparing calculations using the all-electron Hamiltonian, the semi-local Hamiltonian and the KB Hamiltonian. If a ghost state is detected, occurring for some $\tilde{l}$, it may be eliminated: (i) changing the component l which is set as the local part of the potential, (ii) varying the core cutoff radii r_{cl} of the $\tilde{l}$ component or of the local component. These changes should be done in such a way to preserve as good as possible the transferability.

B.4 The norm-conserving pseudopotentials built to be used in this work

In this section we want to discuss how we have applied the above explained techniques to create norm-conserving pseudopotentials for Ga, As and Al atoms. The tool used to perform the numerical calculation is the fhi98PP package [176] by Fuchs and Scheffler. The code allows to generate norm-conserving pseudopotentials adapted to DFT calculations, for all the interesting elements throughout the periodic table. The procedure of construction is based on a scalar-relativistic all-electron calculation of the free atom. Both the scheme by Hamann [177], described in Section B.3.1, and the scheme by Troullier and Martins [163], described in Section B.3.2, are implemented and can be selected by the user to generate the atomic pseudopotentials. We remark once again that no experimental input is needed. The exchange-correlation potential can be implemented both in different parameterizations of the local density approximation and in the generalized gradient approximation. A partial core density can be included to allow for non-linear core-valence exchange-correlation. The package includes some facilities to test the quality of the pseudopotentials directly on the free atom, in particular their softness and their transferability, examining suitable cutoff energies for plane-wave basis set, scattering properties, excitation energies and chemical hardness properties. Moreover, the presence of unphysical states, in case of Kleinman-Bylander separable pseudopotentials, is detected by inspection of the bound spectrum and by the analysis of Gonze *et al.* . For further details we suggest to see the Ref. [176].

Our *ab initio* pseudopotentials are generated using the method of Hamann *et al.* [161] for Ga and As atoms, while the method of Troullier and Martins is used for Al atoms. We have used the Kleinman-Bylander form for the pseudopotential, after having accurately verified not to have ghost states. We have paid particular attention to the choice of the reference configurations (see Table B.2), to mimic as closely as possible the environment in which the atom is placed: this plays an important role to assure a good description of the solid and, in particular, the lattice mismatch between GaAs and AlAs. We remind that each atomic pseudopotential is far from being unique and there are no fixed recipes to know a priori which

Table B.2: Atomic configurations and core radii used in generating *ab initio* pseudopotentials.

Elements	Atomic configurations	
Ga	$4s^{1.5}4p^{0.5}4d^{0.5}$	
Al	$3s^{2.0}3p^{1.0}3d^{0.0}$	s,p components
	$3s^{0.75}3p^{1.0}3d^{0.25}$	d component
As	$4s^{2.0}4p^{3.0}4d^{0.0}$	
Elements	l	r_l
Ga	0	1.2
	1	1.25
	2	1.45
Al	0	1.93
	1	2.39
	2	2.52
As	0	1.15
	2	1.60

method (Hamann or Troullier-Martins), which parameters (r_{lc}, l_{max}), which atomic configurations, etc. can ensure the better pseudopotentials. Thus, we have tested many different atomic Ga, As and Al pseudopotentials, in order to choose the more suitable. We have also considered the core size effects for all the 3 atoms. Atomic tests have suggested that the introduction of non-linear core corrections improves drastically the excitation properties in Ga and Al atoms, but do not vary significantly the behavior of As energy levels in excited configurations. That is the reason why we have simply applied the linear approximation to build the As pseudopotential. The $3d$ core states in Ga atoms are not completely frozen, this fact leads to errors of around mRy for atomic excitations. Nevertheless, we estimate that the error is still reasonable and it is not worth introducing the d states in the valence, increasing strongly the heaviness of the calculations. A crucial test for the reliability of atomic pseudopotentials is their use to calculate the ground state property of a bulk crystal. That is the reason why we refer to the description of ground state calculation on GaAs and AlAs bulk materials, presented in Section 3.3, as the final validation to the quality of our pseudopotentials.

Bibliography

[1] C. Weisbuch and B. Vinter, *Quantum Semiconductor Structures* (Academic Press, San Diego, 1991).

[2] J. Singh, *Physics of Semiconductors and their Heterostructures* (McGraw-Hill, New York, 1993).

[3] F. Capasso, J. Faist, and C. Sirtori, Physica Scripta **T66**, 57-59 (1996).

[4] Y.Y. Zhu and N.B. Ming, Optical and Quantum Electronics **31**, 1093 (1999).

[5] D.C. Hutchings and B.S. Wherrett, Phys. Rev. B **52**, 8150 (1995).

[6] K.J. Luo, S.W. Teitsworth, H. Kostial, H.T. Grahn, and N. Ohtani, Appl. Phys. Lett. **70**, 2825 (1997).

[7] A. Fiore, V. Berger, E. Rosencher, P. Bravetti, and J. Nagle, Nature **391**, 463 (1998).

[8] M.L. Chelikowsky and J.R. Cohen, *Electronic Structure and Optical Properties of Semiconductors* (Springer, Berlin, Heidelberg, 1989).

[9] P.Y. Yu and M. Cardona, *Fundamentals of Semiconductors* (Springer & Verlag, Berlin, Heidelberg, 1996).

[10] M. Garriga, M. Cardona, N.E. Christensen, P. Lautenschlager, T. Isu, and K. Ploog, Phys. Rev. B **36**, 3254 (1987).

[11] M. Alouani, S. Gopalan, M. Garriga, and N.E. Christensen, Phys. Rev. Lett. **61**, 1643 (1988).

[12] P. Tognini, L.C. Andreani, M. Geddo, and A. Stella, Phys. Rev. B **53**, 6992 (1996).

[13] C.W. Teng, J.F. Muth, R.M. Kolbas, K.M. Hassan, A.K. Sharma, A. Kvit, and J. Narayan, Appl. Phys. Lett. **76**, 43 (2000).

[14] G. Bastard, *Wave Mechanics Applied to Semiconductor Heterostructures* (Les Éditions de Physique, Paris, 1992).

[15] D. Kovalev, G. Polisski, J. Diener, H. Heckler, N. Künzner, V. Yu Timoshenko, and F. Koch, Appl. Phys. Lett. **78**, 916 (2001).

[16] A.A. Sirenko, P. Etchegoin, A. Fainstein, K. Eberl, and M. Cardona, Phys. Rev. B **60**, 8253 (1999).

[17] O. Günther, C. Janowitz, G. Jungk, B. Jenichen, R. Hey, L. Däweritz, and K.P Loog, Phys. Rev. B **52**, 2599 (1995).

[18] U. Schmid, N.E. Christensen, M. Cardona, F. Lukeš, and K. Ploog, Phys. Rev. B **45**, 3546 (1992).

[19] K.B. Kahen and J.P. Leburton, Phys. Rev. B **33**, 5465 (1986).

[20] J.B. Xia, Phys. Rev. B **38**, 8358 (1988).

[21] R.G. Dandrea and A. Zunger, Phys. Rev. B **43**, 8962 (1991).

[22] E. Ghahramani, D.J. Moss, and J.E. Sipe, Phys. Rev. B **43**, 9269 (1991).

[23] Y.E. Kitaev, A.G. Panfilov, P. Tronc, and R.A. Evarestov, J. Phys. Cond. Mat. **9**, 257 (1997).

[24] E. Herbert Li, J. Appl. Phys. **82**, 6251 (1997).

[25] S.S. Li and B.F. Zhu, J. Phys. Cond. Mat. **10**, 6311 (1998).

[26] J.-M. Gérard and B. Gayral, in *Confined Photon Systems*, edited by H. Benisty, J.-M. Gérard, R. Houdré, J. Rarity, and C. Weisbuch (Springer, Berlin, 1999), p. 331; J.-M. Gérard, private communication.

[27] D. Bergman, Physics Report **43**, p. 291 (1978); M.G. Cottam and D.R. Tilley, in *Introduction to surface and superlattice excitations* (Cambridge University Press, Cambridge, 1989), p. 267; E. Jahne, Phys. Stat. Sol. (b) **194**, 279 (1996).

[28] S. Botti and L.C. Andreani, Phys. Rev. B **63** , 235313 (2001).

[29] L.W. Wang, A. Franceschetti, and A. Zunger, Phys. Rev. Lett. **78**, 2819 (1997).

[30] L. Reining, V. Olevano, A. Rubio, and G. Onida, submitted to Phys. Rev. Lett., cond-mat/0109434.

[31] L.W. Wang and A. Zunger, Phys. Rev. B **59**, 15806 (1999).

[32] J.M. Luttinger and W. Kohn, Phys. Rev. **97**, 869 (1955).

[33] E.O. Kane, J. Phys. Chem. Solids **1**, 82-99 (1956); E.O. Kane, J. Phys. Chem. Solids **1**, 249 (1957).

[34] D.M. Wood and A. Zunger, Phys. Rev. B **53**, 7949 (1996).

[35] L.W. Wang and A. Zunger, Phys. Rev. B **54**, 11417 (1996).

[36] C. Pryor, Phys. Rev. B **57**, 7190 (1998).

[37] H. Jiang and J. Singh, Phys. Rev. B **56**, 4696 (1997).

[38] Y.T. Lu and L.J. Sham, Phys. Rev. B **40**, 5567 (1989).

[39] H. Fujimoto, C. Hamaguchi, T. Nakazawa, K. Tauiguchi, K. Imanishi, H. Kato, and Y. Watanabe, Phys. Rev. B **41**, 7593 (1990).

[40] J.B. Xia and Y.C. Chang, Phys. Rev. B **42**, 1781 (1990).

[41] Z.Q. Li and W. Pötz, Phys. Rev. B **46**, 2109 (1992).

[42] M.A. Gell and M. Jaros, Superlatt. Microstruct. **3**, 121 (1987).

[43] L. Pavesi and M. Guzzi, J. Appl. Phys. **75**, 4779 (1994).

[44] K.A. Mäder and A. Zunger, Phys. Rev. B **50**, 17393 (1994).

[45] S. Botti, "Laurea" thesis, Chapter 7, University of Pavia (1998).

[46] For a description of symmetry properties of superlattices see L.J. Sham and Y.-T. Lu, J. Lumin. **44**, 207 (1989).

[47] A. Franceschetti and A. Zunger, Phys. Rev. B **52**, 14664 (1995); H. Fu and A. Zunger, Phys. Rev. Lett. **80**, 5397 (1998).

[48] M. Hosoda, N. Ohtani, K. Tominaga, H. Mimura, and T. Watanabe, Phys. Rev. B **56**, 6432 (1997).

[49] G. Li, D. Jiang, H. Han, Z. Wang, and K. Ploog, Phys. Rev. B **40**, 10430 (1989).

[50] L.H. Thomas, Camb. Philos. Soc. **23**, 542 (1927).

[51] E. Fermi, Z. Phys. **48**, 73 (1928).

[52] P. Hohenberg and W. Kohn, Phys. Rev. **136**, B864 (1964).

[53] R.M. Dreizler and E.K.U. Gross, *Density Functional Theory* (Springer & Verlag, Berlin, 1990).

[54] W. Kohn and L. Sham, Phys. Rev. **140**, A1133 (1965).

[55] H. Englisch and R. Englisch, Phys. Stat. Sol. B **123**, 711 (1984); H. Englisch and R. Englisch, Phys. Stat. Sol. B **124**, 373 (1984).

[56] D.M. Ceperley and B.J. Alder, Phys. Rev. Lett. **45**, 566 (1980).

[57] J.P. Perdew and A. Zunger, Phys. Rev. B **23**, 5084 (1981).

[58] J.P. Perdew, K. Burke, and Y. Wang Phys. Rev. B **54**, 16533 (1996); J.P. Perdew, K.A. Jackson, M.R. Pederson, D.J. Singh, and C. Fiolhais, Phys. Rev. B **46**, 6671 (1992).

[59] R.O. Jones and O. Gunnarsson, Rev. Mod. Phys. **61**, 689 (1989).

[60] J.P. Perdew, Phys. Rev. Lett. **55**, 1665 (1985); A.D. Becke, Phys. Rev. A **38**, 3098 (1988); D.C. Langreth and M.J. Mehl, Phys. Rev. Lett. **47**, 446 (1981); J.P. Perdew, K. Burke, and M. Ernzerhof, Phys. Rev. Lett. **77**, 3865 (1997).

[61] M. Fuchs, M. Bockstedte, E. Pehlke, and M. Scheffler, Phys. Rev. B **57**, 2134 (1998), and references therein.

[62] O. Gunnarson, M. Johnson, and B.I. Lundqvist, Phys. Rev. B **20**, 3136 (1979).

[63] A. Baldereschi, Phys. Rev. B **7**, 5212 (1973).

[64] D.J. Chadi and M.L. Cohen, Phys. Rev. B **8**, 5747 (1973).

[65] H.J. Monkhorst and J.D. Pack, Phys. Rev. B **13**, 5188 (1976).

[66] O. Jepsen and O.K. Andersen, Phys. Rev. B **29**, 5965 (1984).

[67] O. Jepsen and O.K. Andersen, Soldi State Commun. **9**, 1763 (1971).

[68] G. Lehmann and M. Taut, Phys. Status Solidi B **54**, 469 (1972).

[69] S. Baroni, A. Dal Corso, S. De Gironcoli, and P. Giannozzi, http://www.pwscf.org.

[70] E.R. Davidson, Computer Phys. Commun. **53**, 49 (1989).

[71] S.B. Zhang and M.L. Cohen, Phys. Rev. B **35**, 7604 (1987).

[72] S.T. Weir, Y.K. Vohra, C.A. Vanderborgh, and A.L. Ruoff, Phys. Rev. B **39**, 1280 (1989).

[73] N. Chetty, A. Muñoz, and R.M. Martin, Phys. Rev. B **40**, 11934 (1989).

[74] B.K. Agrawal and S. Agrawal, Phys. Rev. B **45**, 8321 (1992).

[75] R.G. Greene, H. Luo, T. Li, and A.L. Ruoff, Phys. Rev. Lett. **72**, 2045 (1994).

[76] G.C. Liu, Z.W. Lu, and B.M. Klein, Phys. Rev. B **51**, 5678 (1995).

[77] A. Mujica, R.J. Needs, and A. Muñoz, Phys. Rev. B **52**, 8881 (1995).

[78] F.D. Murnaghan, Proc. Nat. Acad. Sci. USA **50**, 697 (1944).

[79] F. Birch, J. Geophys. Res. **83**, 1257 (1987).

[80] M. Levy, J.P. Perdew, and V. Sahni, Phys. Rev. A **30**, 2745 (1984).

[81] P. Giannozzi, S. De Gironcoli, P. Pavone, and S. Baroni, Phys. Rev. B **43**, 7232 (1991).

[82] A.L. Fetter and J.D. Walecka, *Quantum Theory of Many-Particle Systems* (Mc Graw-Hill, New York, 1971).

[83] L. Hedin and S. Lundqvist, *Solid State Physics*, edited by F. Seitz, D. Turnbull, and H. Ehrenreich (Academic, New York, 1969), Vol. 23, p.1.

[84] C.-O. Almbkadh and U. Von Bart, Phys. Rev. B **31**, 3231 (1985).

[85] M.S. Hybertsen and S.G. Louie, Phys. Rev. B **34**, 5390 (1986).

[86] R.W. Godby, M. Schlüter, and L.J. Sham, Phys. Rev. B **35**, 4170 (1987).

[87] R.W. Godby, M. Schlüter, and L.J. Sham, Phys. Rev. B **37** 10159 (1988).

[88] M. Hybertsen and S.G. Louie, Phys. Rev. Lett. **55**, 1418 (1985).

[89] M. Hybertsen and S.G. Louie, Phys. Rev. B **32**, 7005 (1985).

[90] R.W. Godby, M. Schlüter, and L.J. Sham, Phys. Rev. Lett. **56**, 2415 (1986).

[91] R.W. Godby, M. Schlüter, and L.J. Sham, Phys. Rev. B **36**, 3497 (1987).

[92] L.J. Sham and M. Schlüter, Phys. Rev. Lett. **51**, 1888 (1983).

[93] J.P. Perdew and M. Levy, Phys. Rev. Lett. **51**, 1884 (1983).

[94] M. Lannoo, M. Schlüter, and L.J. Sham, Phys. Rev. B **32**, 3890 (1985).

[95] L.J. Sham and M. Schlüter, Phys. Rev. B **32**, 3883 (1985).

[96] L. Hedin, Phys. Rev. B **139**, 796 (1965).

[97] G.B. Bachelet and N.E. Christensen, Phys. Rev. B **31**, 879 (1985).

[98] V. Fiorentini, Phys. Rev. B **46**, 2086 (1992).

[99] *Physics of Group IV Elements and III-V Compounds*, edites by O. Madelung, M. Schulz, and H. Weiss, Landolt-Börnstein, Numerical Data and Functional Relationships in Science and Technology, New Series Group III, Vol. 17a (Springer, New York, 1982).

[100] T.C. Chiang, J.A. Knapp, M. Aono, and D.E. Eastman, Phys. Rev. B **21**, 3513 (1980).

[101] D.E. Aspnes, S.M. Kelso, R.A. Logan, and R. Bhatt, J. Appl. Phys. **60**, 754 (1986).

[102] D.J. Wolford and J.A. Bradley, Solid State Commun. **53**, 1069 (1985).

[103] D.E. Aspnes, C.G. Olson, and Q.W. Lynch, Phys. Rev. Lett. **37**, 776 (1976).

[104] A. Onton, in *Proceedings of the 10th International Conference on Physics of Semiconductors, Cambridge, Massachusetts*, 1970 (USAEC, New York, 1970), p. 107.

[105] B. Monemar, Phys. Rev. B **8**, 5711 (1973).

[106] D.M. Bylander and L. Kleinman, Phys. Rev. B **34**, 5280 (1986).

[107] D.M. Wood, S.-H. Wei, and A. Zunger, Phys. Rev. B **37**, 1342 (1988).

[108] B.I. Min, S. Massidda, and A.J. Freeman, Phys. Rev. B **38**, 1970 (1988).

[109] S. Baroni, P. Giannozzi, and E. Molinari, Phys. Rev. B **41**, 3870 (1990).

[110] F. Bassani and G. Pastori Parravicini, *Electronic States and Optical Transitions in Solids* (Pergamon Press, Oxford, 1975).

[111] E.O. Kane, Phys. Rev. **180**, 852 (1969).

[112] S. Antoci and G.F. Nardelli, Phys. Rev. B **6**, 1311 (1972).

[113] V.M. Agranovich and V.E. Kravtsov, Solid State Commun. **55**, 85 (1985).

[114] M. Cardona, in *Semiconductor Superlattices and Interfaces*, Proceedings of the International School of Physics "E. Fermi", Course CXVII, edited by A. Stella and L. Miglio (North-Holland, Amsterdam, 1993), p. 435.

[115] S.L. Adler, Phys. Rev. **126**, 413 (1962).

[116] N. Wiser, Phys. Rev. **129**, 62 (1963).

[117] W. Hanke, Advances in Physics **27**, 287 (1978).

[118] V.U. Nazarov, Phys. Rev. B **49**, 17342 (1994).

[119] G. Grosso and G. Pastori Parravicini, *Solid State Physics* (Academic Press, London, 2000).

[120] P. Lautenschlager, M. Garriga, S. Logothetidis, and M. Cardona, Phys. Rev. B **35**, 9174 (1987).

[121] M. Garriga, M. Kelly, and K. Ploog, Thin Solid Films **233**, 122 (1993).

[122] S. Froyen, Phys. Rev. B **39**, 3168 (1989).

[123] E.E. Mendez, L.L. Chang, G. Landgren, R. Ludeke, L. Esaki, and F.H. Pollak, Phys. Rev. Lett. **46**, 1230 (1981).

[124] See e.g. O. Krebs and P. Voisin, Phys. Rev. Lett. **77**, 1829 (1996); O. Krebs, P. Voisin, D. Rondi, J.L. Gentner, L. Goldstein, and J.C. Harmand, Physica E **2**, 59 (1998).

[125] See e.g. J.D. Joannopoulos, R.D. Meade, and J.N. Winn, *Photonic Crystals: molding the flow of light* (Princeton University Press, 1995).

[126] See e.g.: L.C. Andreani, *Confined Electrons and Photons – new Physics and Devices*, edited by E. Burstein and C. Weisbuch (Plenum, New York, 1995), p. 57.

[127] E. Runge and E.K.U. Gross, Phys. Rev. Lett. **52**, 997 (1984).

[128] E.K.U. Gross, F.J. Dobson, and M. Petersilka, *Density Functional Theory* (Springer, New York, 1996).

[129] G. Onida, L. Reining, R.W. Godby, R. Del Sole, and W. Andreoni, Phys. Rev. Lett. **75**, 818 (1995); S. Albrecht, G. Onida, and L. Reining, Phys. Rev. B **55**, 10278 (1997).

[130] S. Albrecht, L. Reining, R. Del Sole, and G. Onida, Phys. Rev. Lett. **80**, 4510 (1998).

[131] L.X. Benedict, E.L. Shirley, and R.B. Bohn, Phys. Rev. B **57**, R9385 (1998).

[132] M. Rohlfing and S.G. Louie, Phys. Rev. Lett. **81**, 2312 (1998).

[133] E.K.U. Gross and W. Kohn, Phys. Rev. Lett. **55**, 2850 (1985).

[134] E.K.U. Gross and W. Kohn, Phys. Rev. Lett. **57**, 923 (1986).

[135] I.V. Tokatly and O. Pankratov, Phys. Rev. Lett. **86**, 2078 (2001).

[136] see, e.g., M.E. Casida, in *Recent Advances in Density Functional Methods*, Part I, edited by D.P. Chong (World Scientific, Singapore), p. 155.

[137] J. Dobson, G. Vignale, and M.P. Das, *Electronic Density Functional Theory: Recent Progress and New Directions* (Plenum, New York, 1997).

[138] K. Burke, M. Petersilka, and E.K.U. Gross, *Recent Advances in Density Functional Methods*, edited by P. Fantucci and A. Bencini (World Scientific, Singapore, 2001).

[139] G. Onida, L. Reining, and A. Rubio, Rev. Mod. Phys., to be published.

[140] R. Van Leeuwen, Phys. Rev. Lett. **82**, 3863 (1999).

[141] R. Del Sole and R. Girlanda, Phys. Rev. B **48**, 11789 (1993).

[142] M. Cardona, in *Atomic Structure and Properties of solids*, edited by E. Burstein (Academic Press, New york, 1972), P. 514.

[143] P. Etchegoin, A. Fainstein, A. Sirenko, B. Koopmans, B. Richards, P.V. Santos, M. Cardona, K. Totenmeyer, and K. Eberl, Phys. Rev. B **53**, 13662 (1996).

[144] N. Vast, L. Reining, V. Olevano, P. Schattschneider, and B. Jouffrey, submitted to Phys. Rev. Lett. .

[145] We found ε_{GaAs} and ε_{AlAs}, in agreement with previous calculations [81].

[146] M.S. Hybertsen and S.G. Louie, Phys. Rev. B **35**, 5585 (1987).

[147] S. Albrecht, L. Reining, R. Del Sole, and G. Onida, Phys. Rev. Lett. **80**, 4510 (1998).

[148] V.I. Gavrilenko and F. Bechstedt, Phys. Rev. B **55**, 4343 (1997).

[149] S. Botti, V. Olevano, L. Reining, A. Rubio, and N. Vast, to be submitted.

[150] M. Rohlfing and S.G. Louie, Phys. Rev. B **62**, 4927 (2000), and references therein.

[151] B. Arnaud and M. Alouani, Phys. Rev. B **63**, 085208 (2001).

[152] P. Ghosez, X. Gonze, and R.W. Godby, Phys. Rev. B **56**, 12811 (1997).

[153] M.A. Haase *et al.*, Appl. Phys. Lett. **59**, 1272 (1991); H. Leon *et al.*, Appl. Phys. Lett. **59**, 3619 (1991).

[154] C. Tserbak and G. Theodorou, J. Appl. Phys. **76**, 1062 (1994).

[155] see, e.g., L. Dorigoni, O. Bisi, F. Bernardini and S. Ossicini, Phys. Rev. B **53**, 4557 (1996).

[156] A. Franceschetti and A. Zunger, Phys. Rev. B **52**, 14664 (1995); M.H. Szymanska, P.B. Littlewood, and R.J. Needs Phys. Rev. B **63**, 205317 (2001); G. Goldoni, F. Rossi, E. Molinari, and A. Fasolino, Phys. Rev. B **55**, 7110 (1997).

[157] E. Fermi, Il Nuovo Cimento **11**, 157 (1934).

[158] J.C. Phillips and L. Kleinman, Phys. Rev. **116**, 287 (1959).

[159] M.L. Cohen and V. Heine, Solid State Phys. **24**, 37 (1970).

[160] J.R. Chelikowsky and M.L. Cohen, Phys. Rev. B **14**, 556 (1976).

[161] D.R. Hamann, M. Schlüter, and C. Chiang, Phys. Rev. Lett. **43**, 1494 (1979).

[162] G. Bachelet, D.R. Hamann, and M. Schlüter, Phys. Rev. B **26**, 4199 (1982).

[163] N. Troullier and J.L. Martins, Phys. Rev. B **43**, 1993 (1991).

[164] W.E. Pickett, Comments on Solid State Phys. **12**, 57 (1986).

[165] L.W. Wang and A. Zunger, Phys. Rev. B **51**, 17398 (1995).

[166] L. Bellaiche, S.H. Wei, and A. Zunger, Phys. Rev. B **54**, 17568 (1996).

[167] H. Fu and A. Zunger, Phys. Rev. B **55**, 1642 (1996).

[168] A.J. Williamson, J. Kim, L.W. Wang, S.-H. Wei, and A. Zunger cond-mat/9805051.

[169] D. Vanderbilt, Phys. Rev. B **41**, 7892 (1990).

[170] M. Fuchs, M. Bockstedte, E. Pehlke, and M. Scheffler, Phys. Rev. B **57**, 2134 (1998).

[171] S.G. Louie, S. Froyen, M.L. Cohen, Phys. Rev. B **26**, 1738 (1982).

[172] G.P. Kerker, J. Phys. C **13**, L189 (1980).

[173] L. Kleinman and D.M. Bylander, Phys. Rev. Lett. **48**, 1425 (1982).

[174] X. Gonze, R. Käckell, and M. Scheffler, Phys. Rev. B **41**, 12264 (1990); X. Gonze, P. Käckell, and M. Scheffler, Phys. Rev. B **41**, 12264 (1990).

[175] A. Messiah, *Quantum Mechanics* (North-Holland, Amsterdam, 1974), Vol. 1, p. 98.

[176] M. Fuchs and M. Scheffler, Computer Physics Communications.

[177] D.R. Hamann, Phys. Rev. B **40**, 2980 (1989).

Ringraziamenti

È giunto il momento di scrivere di nuovo la parola *fine*. Inevitabilmente, i ringraziamenti diventano l'occasione per tirare le somme di questi anni di dottorato, 3 anni passati tra Pavia e Parigi. Mi sono accorta, prima con disappunto, poi riflettendoci con piacere, che gli amici "pavesi e parigini" sono tanto numerosi da rendere impossibile ringraziarli singolarmente. Questo punto da solo è già sufficiente a rendere il mio personale bilancio molto positivo. Ma c'è di più. Penso che il dottorato non sia stato un "parcheggio", come molti di noi temevano al momento di decidere cosa fare dopo la laurea. È stato un'esperienza formativa che mi ha molto arricchito, indipendentemente da quello che farò a partire da domani. A questo proposito voglio ringraziare *tutte* le persone con cui ho avuto l'opportunità di collaborare. Primi fra tutti, il mio tutore Claudio Andreani a Pavia, insieme a Lucia Reining, Nathalie Vast e Valerio Olevano a Parigi. Grazie ad Angel Rubio per le interessanti discussioni. Lavorare con loro è stato e spero continui a essere un grande privilegio. Grazie ad Alberto per aver curato la preparazione dei miei seminari in francese e per la lettura critica della mia tesi. Grazie a Roberto per essersi occupato delle noiose questioni burocratiche a Pavia e della fase di stampa. Grazie a Francesco e Mario per i frequenti aiuti in campo informatico. La correzione attenta del manoscritto a cui Lucia e Nathalie hanno dedicato il loro già esiguo tempo libero è stata un aiuto insostituibile. Voglio inoltre ringraziare per la sua disponibilità Rodolfo Del Sole, lettore della mia tesi. Dei ringraziamenti particolari vanno a Sergio Ratti, Coordinatore del Dottorato in Fisica a Pavia, e a Guillaume Petite, Direttore del Laboratoire des Solides Irradiés, per l'accoglienza straordinaria che mi ha riservato. Un grazie sentito, inoltre, a tutti i colleghi/amici del Gruppo di Teoria dello Stato Solido e del gruppo NMR a Pavia e del Laboratoire des Solides Irradiés a Palaiseau, per aver reso sempre piacevole il tempo lavorativo e non lavorativo passato insieme. Infine, grazie a *tutti* gli amici, vecchi e nuovi, e alla mia famiglia, con cui ho condiviso quotidianamente questa esperienza. Non prendetevela se non vi nomino a uno a uno, avete tutti un posto speciale.

FINE